2010

Functionalized mesoporous silica nanoparticles (MSNs) for applications in drug delivery and catalysis

Wei Huang
Iowa State University

Functionalized mesoporous silica nanoparticles (MSNs) for applications in drug delivery and catalysis

by

Wei Huang

A dissertation submitted to the graduate faculty

in partial fulfillment of the requirements for the degree of

DOCTOR OF PHILOSOPHY

Major: Chemistry

Program of Study Committee
Brian G. Trewyn, Co-major Professor
Aaron D. Sadow, Co-major Professor
Marek Pruski
Robert S. Houk
Zhiqun Lin

Iowa State University
Ames, Iowa
2010

TABLE OF CONTENT

ACKNOWLEDGEMENTS

First, I would like to thank Dr. Victor S.-Y. Lin, who inspired me with his wisdom and enthusiasm.

I would like to thank my current major professor Dr. Brian Trewyn for his guidance and suggestion on my research projects and my thesis.

I also would like to thank my co-major professor Dr. Aaron Sadow and my past and present POS committee members, Dr. Marek Pruski, Dr. Robert Houk, Dr. Zhiqun Lin, and Dr. Hans Stauffer, in no particular order, for their time and support.

I appreciate the collaboration with Dr. Pruski's research group using their advanced solid-state NMR techniques to help me understand our wonderful mesoporous silica materials better.

Many thanks to all the past and current group members, especially Dr. Yang Cai, Dr. Yulin Huang, Dr. Po-Wen Chung, Mr. Chih-Hsiang Tsai, and Ms. I-Ju Fang for their friendship and company during my Ph.D. study.

Finally, I would like to express my special thanks to Dr. Hung-Ting Chen for standing by my side all the time and for bringing happiness to my life.

ABSTRACT

Well-ordered mesoporous silica nanoparticles (MSNs) feature a great number of important characteristics including large surface area and pore volume, tunable pore diameter, uniform particle size, and good biocompatibility. The feasibility of selective functionalization on the exterior and interior surface of MSNs makes them applicable in areas as diverse as sorption, separation, sensing, drug delivery, and catalysis.

Poly(L-lysine) was immobilized onto the outer surface of amine functionalized MSN via ring-opening polymerization. The poly(L-lysine) coated MSN (PLL-MSN) could be internalized by human cervical cancer (HeLa) cells with extremely high efficiency, which made the delivery of a large amount of drugs into cells possible. The release of the drugs was regulated by the degradation of poly(L-lysine). Trypsin, an enzyme abundant in the intestine where most molecules are absorbed by human body, could digest poly(L-lysine) and open the pore channels of PLL-MSN. On the other hand, pepsin, an enzyme that accumulates in the stomach, had no impact on poly(L-lysine) and therefore the loaded drugs could be kept inside the pore channels and protected from enzymatic hydrolysis. We envision that PLL-MSN has great potential as an oral drug delivery vehicle.

MSNs were also used as catalyst supports in cellulose degradation reactions. We have synthesized a series of platinum nanoparticle immobilized mesoporous silica nanoparticles (Pt NP-MSNs) by using N-(2-aminoethyl)-3-aminopropyl (AAP) and 3-[2-(2-aminoethylamino)ethylamino]propyl (AEP) functionalized MSNs as solid supports. Platinum nanoparticles were anchored on the MSNs by complexation between the Pt precursor and surface amine groups followed by hydrogen reduction. Pt NP-MSNs

successfully catalyzed the conversion of cellulose into valuable polyols: sorbitol and mannitol and could be recycled at least three times under optimized reaction conditions.

In order to expand the applications of MSNs, a series of organofunctionalized large pore mesoporous silica nanoparticles (LPMSNs) were synthesized via the co-condensation method under acidic conditions using a triblock copolymer (P104) as the structure-directing agent. The hydrothermal temperature, the amount of organosilanes, and the sequence of reagent additions were optimized to yield functionalized LPMSN with large pore size and well-controlled particle morphology. The sulfonic acid functionalized silica synthesized under optimum conditions showed better catalytic performance than traditional sulfonic acid functionalized SBA-15 in esterification reactions.

A mesoporous aluminum silicate (Al-MS) material has been synthesized via co-condensation by using $NaAlO_2$ as aluminum source under basic conditions. The aluminum was tetrahedrally coordinated throughout Al-MS and, for the first time, the quantity of the surface aluminum sites was determined by solid-state NMR studies. The silicon to aluminum atomic ratios at the surface and in the bulk were around 100 and 60, respectively; indicating less chemically accessible aluminum sites on the surface. Despite the low surface concentration of aluminum. Al-MS showed excellent catalytic reactivity for the Claisen rearrangement of allyl phenyl ether.

CHAPTER 1. GENERAL INTRODUCTION

Dissertation Organization

The main objective of this dissertation is to present the synthetic strategies of functional mesoporous silica nanoparticles (MSNs) and focus on their applications in controlled delivery and catalysis utilizing their versatile properties. There are totally five chapters plus an appendix in this dissertation. Chapter 1 gives a general introduction on different types of mesoporous silica nanomaterials, the two most commonly used surface modification methods, and the special and unique properties that make them promising candidates as drug delivery vehicles and catalysts. Chapters 2 to 4 contain three major projects that I have accomplished during my graduate study. Specifically, Chapter 2 describes the synthesis of a biodegradable polymer poly(L-lysine) coated mesoporous silica nanoparticle (PLL-MSN) as an oral drug delivery vehicle. The release of the drug is prohibited in the stomach because the polymer remains intact in artificial gastric fluid but it would be triggered in the intestinal environment, where PLL could be degraded readily by trypsin under physiological condition. Chapter 3 highlights the fabrication of platinum nanoparticle immobilized mesoporous silica nanoparticles (Pt NP-MSNs) as effective catalysts for selective degradation of cellulose into value-added chemicals: sorbitol and mannitol. Pt NP-MSNs could be recycled at least three times under our modified and relatively mild reaction conditions. Chapter 4 presents a new co-condensation method to synthesize a series of organofunctionalized large pore mesoporous silica nanoparticles (LPMSNs) with controlled particle size and particle shape. The increased pore diameter, shortened channel length, and the high thermal stability all attribute to the advantages of

utilizing these materials as catalyst supports. Chapter 5 summaries the overall results. Last, the appendix is focused on the synthesis of a mesoporous aluminum silicate (Al-MS) material with single-type active sites confirmed by solid-state NMR studies. Al-MS shows an excellent catalytic activity for the Claisen rearrangement of allyl phenyl ether despite the low surface concentration of Al.

Introduction

Well-ordered mesoporous silica nanomaterials have attracted extensive attention and interest since introducing a new era to overcome the pore size limitation of zeolites (0.6~1.8 nm).[1-3] A major breakthrough was the fabrication of MCM-type mesoporous material reported by scientists in Mobil Research and Development Corporation in 1992.[4] MCM-41, as the most distinguished member in the MCM family, exhibits many attractive and important features, including high surface area (~1000 m^2/g), large pore volume (0.7~1 cm^3/g), tunable pore size (2~10 nm), controlled morphology, facile functionalization, and good biocompatibility. MCM-41 was prepared using a cationic quaternary ammonium surfactants, such as cetyltrimethylammonium bromide (CTAB), as the structure-directing agent through a liquid crystal templating (LCT) mechanism as shown in Figure 1-1. Later in 1998, Stucky and co-workers published the synthesis of SBA-15 using a high molecular weight nonionic Pluronic triblock copolymer, poly(ethyleneoxide)-*block*-poly(propyleneoxide)-*block*-poly(ethyleneoxide) (EO_n-PO_m-EO_n), as a surfactant under acidic condition.[5] Nitrogen sorption analysis[6] and high-resolution transmission electron microscopy (HRTEM) studies[7] proved the presence of 2-D hexagonal mesoporous channels in SBA-15 with interconnected micropores originated from the hydrophilic EO domains of

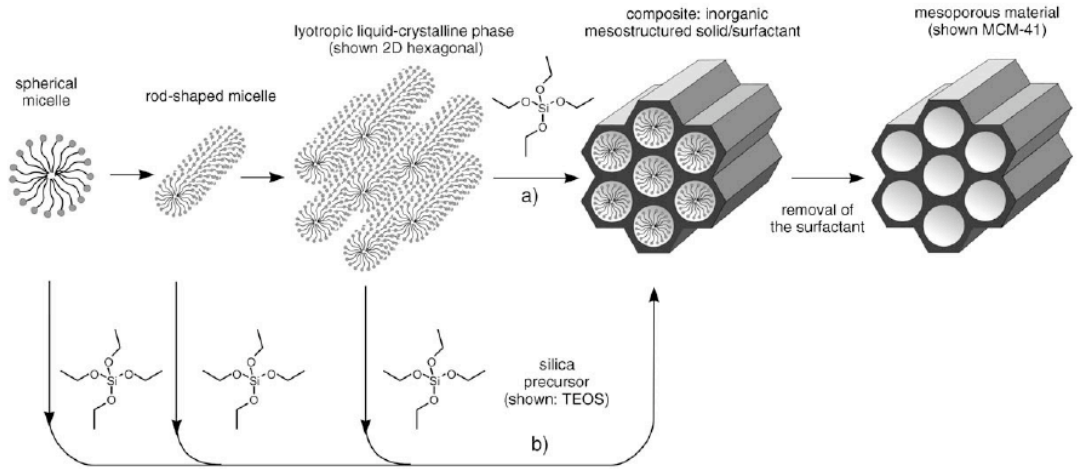

Figure 1-1. Possible mechanistic pathways for the formation of MCM-41: (a) pure liquid crystal template pathway and (b) cooperative liquid crystal template pathway.

the triblock copolymer. The systematical modification of synthetic parameters, such as the aging temperature or incorporation of organic additives, demonstrate that the pore diameter could be expanded up to 30 nm.[5] In addition, the thick silica wall (>3 nm) of SBA-15 resulted in high thermal and hydrothermal stability comparing to the traditional MCM-41 typed material, which is a crucial requirement as a heterogeneous catalytic support. The large pore diameter of SBA-15 materials is important and beneficial for applications in controlled-release delivery, such as accommodation of large molecular weight enzymes and proteins, and catalytic support for bulky homogeneous catalysts, such as versatile transitional metal complexes with a regular diameter of 1 nm. However, the particle morphology of SBA-15 materials is not as well-controlled as MCM-41s. Instead of individual particles, the conventional SBA-15 consists of rod-like domains, coupling and stacking into wheat-like macrostructure with sizes from ten to a few hundred micrometers as reported in the literature.[8-11] It has been reported that the macrostructure of SBA-15 played an important

role in bioimmobilization ability of lysozyme.[12] Zhao and co-workers successfully synthesized well-separated rod-like SBA-15 particles by adding considerable amount of inorganic salt into the original preparation solution mixture. The resultant SBA-15 particles were used as absorbents for immobilization of lysozymes and compared enzyme capacity with conventional aggregated SBA-15 chucks. The uptake experiments indicated that the individual SBA-15 rods not only adsorbed faster but also immobilized larger amount of lysozymes relative to normal SBA-15 aggregate. We envision that the macrostructure of porous materials as a catalyst support will also have significant impact on the catalytic performance. To the best of our knowledge, there is no study on this subject yet, therefore, it is one of my motivations to investigate the synthesis of functionalized large pore mesoporous silica nanoparticles with controlled morphology and compare the catalytic performance with conventional SBA-15 as described in more detail in Chapter Four. Besides MCM- and SBA-typed materials, other mesoporous silica materials, including MCF[13, 14] (mesostructured cellular foam) made by addition of a swelling agent, such as 1,3,5-trimethylbenzene (TMB) to the synthesis of SBA-15, MSU[15, 16] (Michigan State University) material prepared by nonionic polyethylene glycol polymers in neutral environment, and FSM[17] (folded sheet mesoporous material) derived from layered polysilicate kanemite are also discovered in the similar time.

The great potential of mesoporous silica nanomaterials lies in the ease to design and modify the surface with various functionalities toward different goals.[18-20] The well-ordered porous structure renders mesoporous silica nanomaterials with large surface area. The interior surface inside the pore channels is responsible for around 90% of the total surface area and the exterior surface composes the balance as measured from the nitrogen

adsorption/desorption analysis. The two unique surfaces of mesoporous silica nanomaterials give researchers a great opportunity to utilize the materials. There are two well-established methods to selectively functionalize the inner and outer surface with organic groups: co-condensation and post-synthetic grafting methods as illustrated in Figure 1-2. In the co-condensation method, silica sources, such as tetramethyl orthosilicate (TMOS) or tetraethyl

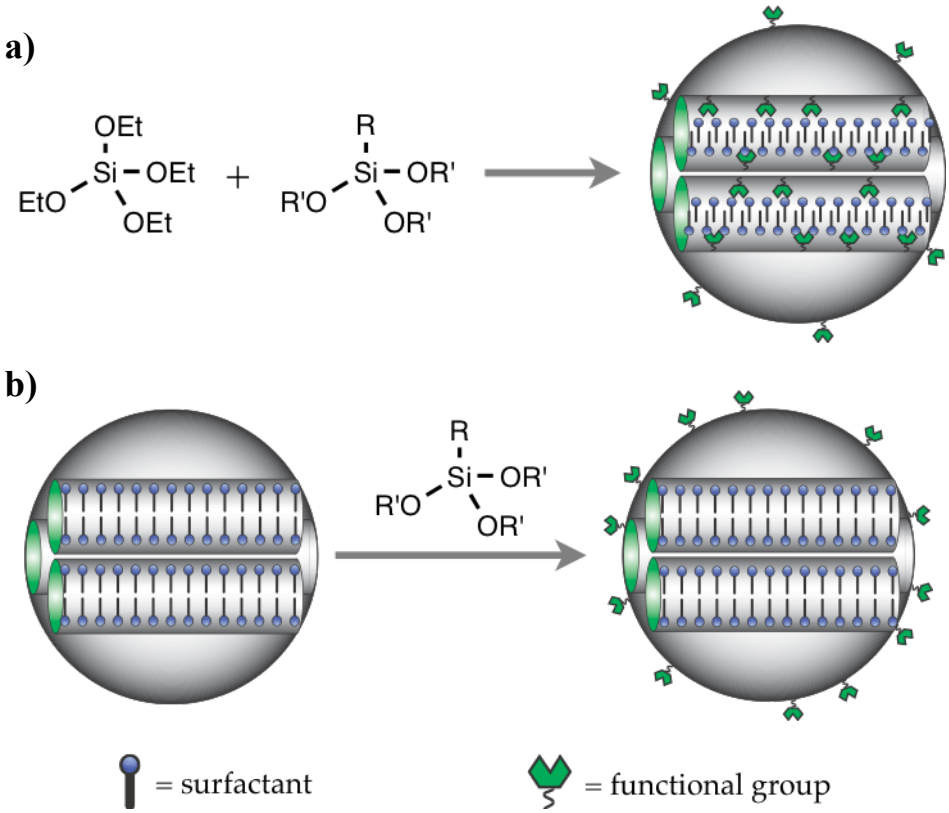

Figure 1-2. Two common material functionalization methods: a) co-condensation; b) post-synthetic graphing.

orthosilicate (TEOS), and organosilanes, such as alkoxysilanes $(R'O)_3SiR$, chlorosilanes $ClSiR_3$, or silazanes $HN(SiR_3)_3$, are added at the same time into the reaction mixture containing the structure-directing agent in either an acidic or basic environments. The organic functional group will incorporate into the silica framework during the synthesis that

resulted in a homogeneous distribution throughout the material, which was proven by Stein and coworkers by determining the two-phase bromination rate of vinyl functionalized MCM-41s prepared from co-condensation.[21] Moreover, pore blocking is not a problem for materials prepared by this route since the organosilanes are direct components of the silica matrix. However, synthesis conditions such as: reaction temperature, chemical nature of the organosilanes, content of organic functionalities, and hydrolysis rate of organosilanes need to be carefully considered and fine-tuned in order to retain the periodic pore arrangement and particle morphology. Acid extraction, not calcination, are suitable in most cases for surfactant removal, since most of the organic groups will decompose at the high calcination temperature (commonly at 550 °C) but can easily retain during the low-temperature extraction process (less than 100 °C). A thorough study on the synthesis of a series of organically functionalized mesoporous silica nanoparticles (MSNs) was published in 2003.[22] Functional groups such as allyl, nitrile, and aldehyde were successfully anchored onto the surface of MSNs via the co-condensation method. All of these functionalized MSN had ordered pore structures and uniform particle sizes. Post-synthetic grafting is another effective way to modify the surface, especially the exterior surface of the mesoporous silica nanomaterials. In this method, well-ordered mesoporous silica nanomaterials are fabricated before they react with organosilanes under dry solvent (commonly anhydrous toluene) conditions at reflux temperature. If the grafting process is performed in the as-made porous materials with surfactants inside the mesopores, the organic functionalities are mainly located on the exterior surface and near the pore openings of the material due to the inaccessibility of interior porous space by protection of surfactants. If the surfactant is removed before the grafting process, theoretically the organic functionalities can be anchored both on the exterior

and interior surfaces of materials. However, the organosilanes react preferentially at the pore openings hindering the diffusion of compounds further into the inner pore channels, leading to the inhomogeneous distribution of organic groups throughout the materials.[23] To the extreme extent, the mesopore channels of the materials could be totally blocked by the immobilized organosilanes. The ordered pore structure and uniform morphology will usually be retained if grafting is not conducted in extremely harsh conditions.

The co-condensation method and post-synthetic grafting process together allow us to selectively modify the exterior and interior surface of mesoporous silica materials with desired functional groups, which is crucial for applications in versatile areas such as catalysis, drug delivery, sorption, separation and sensor. Both of these two modification methods have been properly utilized throughout this dissertation depending on the different goals of the projects.

A rapid growth on interest of utilizing mesoporous silica nanoparticles (MSNs) as a carrier in the controlled release drug delivery system began about a decade ago.[24-29] The good biocompatibility of MSNs was demonstrated by our group and further confirmed by other research groups through countless cellular experiments.[30-32] MSNs do not induce cytotoxicity in a variety of mammalian cell lines such as Chinese hamster ovarian (CHO) cells[33], human cervical cancer (HeLa) cells[34], human liver cells, and human fibroblast cells[35] at concentrations below 100 μg/mL. According to the enhanced permeability and retention (EPR) effect of macromolecules,[36, 37] MSNs within the size domain of 100~130 nm tend to accumulate in tumor tissues much more readily than in normal tissues, resulting in more drugs delivered to tumors compared to normal tissues. In addition, it has been demonstrated that the surface functionality of MSNs can regulate the cellular uptake of materials and also

affect MSNs ability to escape from endosomal entrapment.[30] Taking previous consideration into account, several sophisticated designs of controlled release delivery systems using mesoporous silica nanoparticles with enormous internal surface to encapsulate small drugs by various caps were developed. These caps are linked covalently or non-covalently at the channel opening of MSNs in the manner that the caps can removed and the trapped drugs can be released by external-stimuli including a pH-triggered drug delivery[38] that takes advantage of the lower pH observed in the cancer cells than normal cells, noninvasive photo-responsive drug delivery[35], and enzyme triggered controlled release.[39] Moreover, MSNs as chemical and nucleic acid material carriers was first reported to be able to pass through plant cell walls to deliver both genes and the chemical that induced gene expression simultaneously.[40] Recently, a major development of the MSN-based controlled release delivery is the intravenous injection of these materials and study their biocompatibility and biodistribution in mice.[32] It is found that MSNs can delivery anticancer drugs to tumors by accumulating in tumor xenografts and improve the anticancer drug efficiency. However, intravenous injection has some severe disadvantages, such as risk of infectious diseases. A more popular way of drug uptake is oral drug delivery.[41] The two major difficulties in oral delivery are degradation of drugs by digestive enzymes and short diffusion time of drugs in the small intestine. These two obstacles can be solved by the capped delivery system using MSNs that was developed by our group. As shown in Chapter Two, I designed a potential oral drug delivery vehicle using MSNs as carriers coated with poly(L-lysine) as caps, which is resistant to pepsin in the stomach but efficiently degradable by trypsin in the duodenum. In this way, the mesoporous channels could remain closed while staying in the stomach but reopen as the

polymer caps degraded at the very front part of the small intestine, allowing the drugs to be released and adsorbed by the small intestine.

Mesoporous silica nanomaterials are used frequently as solid supports for advanced heterogeneous catalysts.[42-47] Extensive studies have focused on the immobilization of inorganic or organic active species within the silica framework. The introduced inorganic or organic catalytic sites include incorporation of a trivalent metal like aluminum into the lattice to generate surface-bound Brønsted and Lewis acids and increase the strength of acid sites,[48] encapsulation of metal complexes,[49, 50] and, most commonly used, immobilization of functional organic silanes with catalytic activity such as 4-(dimethylamino)pyridine (DMAP).[51] The catalytically active species are preferably tethered on the surface through covalent bonds linked with single and geminal silanol groups on the silica, which overcomes the leaching problem commonly observed for immobilization of catalytic sites by non-covalent adsorption. The thermal stability and hydrothermal stability of supported porous materials could be enhanced by changing the silica sources and/or reaction conditions to increase the thickness of silica wall and reduce the surface silanol groups.[52-55] For example, MCM-41s synthesized from fumed silica had thicker wall and less silanol groups than that derived from TEOS, and therefore possess higher stability.[56, 57] Extended hydrothermal time also result in the increase of wall thickness and extent of silica condensation within the pore walls, leading to improvement in stability.[58] One important advantage from an environmental point of view of this heterogeneous system is the ease of recovery and recycling of valuable catalytically active species such as chiral metal complex from the reaction mixture.[59-62] The intrinsic properties, plus the flexible and versatile modifications of mesoporous silica nanomaterials make them ideal catalyst supports. A new direction of

utilizing functional MSNs as catalysts is for producing energy or valuable chemicals from sustainable resources such as biomass other than fossil-based energy resources.[63-65] An excellent renewable source is cellulose, which is the most abundant carbon source on earth. In general, cellulose is not edible by human being, i.e. a non-food based resource, therefore, utilization of cellulose to produce valuable chemicals for everyday usage will not increase the food price. However, the challenge of cellulose conversion lies in its robust chemical structure composed of multi-hydrogen bonded polysaccharides through a β-1,4-glucosidic linkage. In Chapter Three, I synthesized a platinum nanoparticle functionalized mesoporous silica nanoparticle (Pt NP-MSN) that could efficiently and selectively convert cellulose to value-added hexitols: sorbitol and mannitol. In addition, the study of reaction mechanism helps understanding of this catalytic system that will lead to better catalyst design and rational control of the products.

References:

1. Seff, K., *Acc. Chem. Res.* **1976,** *9* (4), 121-128.
2. Soler-illia, G. J. D.; Sanchez, C.; Lebeau, B.; Patarin, J., *Chem. Rev.* **2002,** *102* (11), 4093-4138.
3. Zhou, C. F.; Cao, Y.; Zhuang, T. T.; Huang, W.; Zhu, J. H., *J. Phys. Chem. C* **2007,** *111* (11), 4347-4357.
4. Kresge, C. T.; Leonowicz, M. E.; Roth, W. J.; Vartuli, J. C.; Beck, J. S., *Nature* **1992,** *359*, 710-712.

5. Zhao, D.; Feng, J.; Huo, Q.; Melosh, N.; Fredrickson, G. H.; Chmelka, B. F.; Stucky, G. D., *Science* **1998,** *279* (5350), 548-52.

6. Galarneau, A.; Cambon, H.; Di Renzo, F.; Fajula, F., *Langmuir* **2001,** *17* (26), 8328-8335.

7. Liu, J.; Zhang, X.; Han, Y.; Xiao, F. S., *Chem. Mater.* **2002,** *14* (6), 2536-2540.

8. Yu, C. Z.; Fan, J.; Tian, B. Z.; Zhao, D. Y.; Stucky, G. D., *Adv. Mater.* **2002,** *14* (23), 1742-1745.

9. Linton, P.; Wennerstrom, H.; Alfredsson, V., *PCCP* **2010,** *12* (15), 3852-3858.

10. Meynen, V.; Cool, P.; Vansant, E. F., *Microporous Mesoporous Mater.* **2009,** *125* (3), 170-223.

11. Zhao, D. Y.; Sun, J. Y.; Li, Q. Z.; Stucky, G. D., *Chem. Mater.* **2000,** *12* (2), 275-279.

12. Fan, J.; Lei, J.; Wang, L. M.; Yu, C. Z.; Tu, B.; Zhao, D. Y., *Chem. Commun.* **2003,** (17), 2140-2141.

13. Schmidt-Winkel, P.; Lukens, W. W.; Zhao, D. Y.; Yang, P. D.; Chmelka, B. F.; Stucky, G. D., *J. Am. Chem. Soc.* **1999,** *121* (1), 254-255.

14. Lettow, J. S.; Han, Y. J.; Schmidt-Winkel, P.; Yang, P. D.; Zhao, D. Y.; Stucky, G. D.; Ying, J. Y., *Langmuir* **2000,** *16* (22), 8291-8295.

15. Bagshaw, S. A.; Prouzet, E.; Pinnavaia, T. J., *Science* **1995,** *269* (5228), 1242-1244.

16. Prouzet, E.; Cot, F.; Nabias, G.; Larbot, A.; Kooyman, P.; Pinnavaia, T. J., *Chem. Mater.* **1999,** *11* (6), 1498-1503.

17. Inagaki, S.; Fukushima, Y.; Kuroda, K., *J. Chem. Soc. Chem. Commun.* **1993,** (8), 680-682.

18. Stein, A., *Adv. Mater.* **2003,** *15* (10), 763-775.

19. Hoffmann, F.; Cornelius, M.; Morell, J.; Froba, M., *Angew. Chem. Int. Ed.* **2006,** *45* (20), 3216-3251.

20. Trewyn, B. G.; Slowing, I. I.; Giri, S.; Chen, H. T.; Lin, V. S. Y., *Acc. Chem. Res.* **2007,** *40* (9), 846-853.

21. Lim, M. H.; Stein, A., *Chem. Mater.* **1999,** *11* (11), 3285-3295.

22. Huh, S.; Wiench, J. W.; Yoo, J. C.; Pruski, M.; Lin, V. S. Y., *Chem. Mater.* **2003,** *15* (22), 4247-4256.

23. Cheng, K.; Landry, C. C., *J. Am. Chem. Soc.* **2007,** *129* (31), 9674-9685.

24. Lai, C. Y.; Trewyn, B. G.; Jeftinija, D. M.; Jeftinija, K.; Xu, S.; Jeftinija, S.; Lin, V. S. Y., *J. Am. Chem. Soc.* **2003,** *125* (15), 4451-4459.

25. Trewyn, B. G.; Whitman, C. M.; Lin, V. S. Y., *Nano Lett.* **2004,** *4* (11), 2139-2143.

26. Giri, S.; Trewyn, B. G.; Stellmaker, M. P.; Lin, V. S. Y., *Angew. Chem. Int. Ed.* **2005,** *44* (32), 5038-5044.

27. Lu, J.; Choi, E.; Tamanoi, F.; Zink, J. I., *Small* **2008,** *4* (4), 421-426.

28. Zhao, Y.; Trewyn, B. G.; Slowing, I. I.; Lin, V. S. Y., *J. Am. Chem. Soc.* **2009,** *131* (24), 8398-8400.

29. Patil, Y. B.; Swaminathan, S. K.; Sadhukha, T.; Ma, L. A.; Panyam, J., *Biomaterials* **2010,** *31* (2), 358-365.

30. Slowing, I.; Trewyn, B. G.; Lin, V. S. Y., *J. Am. Chem. Soc.* **2006,** *128* (46), 14792-14793.

31. Liu, H. M.; Wu, S. H.; Lu, C. W.; Yao, M.; Hsiao, J. K.; Hung, Y.; Lin, Y. S.; Mou, C. Y.; Yang, C. S.; Huang, D. M.; Chen, Y. C., *Small* **2008,** *4* (5), 619-626.

32. Lu, J.; Liong, M.; Li, Z. X.; Zink, J. I.; Tamanoi, F., *Small* **2010,** *6* (16), 1794-1805.

33. Radu, D. R.; Lai, C. Y.; Jeftinija, K.; Rowe, E. W.; Jeftinija, S.; Lin, V. S. Y., *J. Am. Chem. Soc.* **2004,** *126* (41), 13216-13217.

34. Slowing, I. I.; Trewyn, B. G.; Lin, V. S. Y., *J. Am. Chem. Soc.* **2007,** *129* (28), 8845-8849.

35. Vivero-Escoto, J. L.; Slowing, I. I.; Wu, C. W.; Lin, V. S. Y., *J. Am. Chem. Soc.* **2009,** *131* (10), 3462-3463.

36. Matsumura, Y.; Maeda, H., *Cancer Res* **1986,** *46* (12), 6387-6392.

37. Muggia, F. M., *Clin Cancer Res* **1999,** *5* (1), 7-8.

38. Liu, R.; Zhang, Y.; Zhao, X.; Agarwal, A.; Mueller, L. J.; Feng, P. Y., *J. Am. Chem. Soc.* **2010,** *132* (5), 1500-+1501.

39. Patel, K.; Angelos, S.; Dichtel, W. R.; Coskun, A.; Yang, Y. W.; Zink, J. I.; Stoddart, J. F., *J. Am. Chem. Soc.* **2008,** *130* (8), 2382-2383.

40. Torney, F.; Trewyn, B. G.; Lin, V. S. Y.; Wang, K., *Nat Nanotechnol* **2007,** *2* (5), 295-300.

41. Singh, R.; Singh, S.; Lillard, J. W., *J. Pharm. Sci.* **2008,** *97* (7), 2497-2523.

42. Huh, S.; Chen, H. T.; Wiench, J. W.; Pruski, M.; Lin, V. S. Y., *J. Am. Chem. Soc.* **2004,** *126* (4), 1010-1011.

43. Huh, S.; Chen, H. T.; Wiench, J. W.; Pruski, M.; Lin, V. S. Y., *Angew Chem Int Edit* **2005,** *44* (12), 1826-1830.

44. Nieweg, J. A.; Lemma, K.; Trewyn, B. G.; Lin, V. S. Y.; Bakac, A., *Inorg. Chem.* **2005,** *44* (16), 5641-5648.

45. Mihalcik, D. J.; Lin, W. B., *Angew Chem Int Edit* **2008,** *47* (33), 6229-6232.

46. Demel, J.; Cejka, J.; Stepnicka, P., *J Mol Catal a-Chem* **2010,** *329* (1-2), 13-20.

47. Kamegawa, T.; Yamahana, D.; Yamashita, H., *J. Phys. Chem. C* **2010,** *114* (35), 15049-15053.

48. Cai, Y.; Kumar, R.; Huang, W.; Trewyn, B. G.; Wiench, J. W.; Pruski, M.; Lin, V. S. Y., *J. Phys. Chem. C* **2007,** *111* (3), 1480-1486.

49. Trejda, M.; Wojtaszek, A.; Ziolek, M.; Kujawa, J., *Appl Catal a-Gen* **2009,** *365* (1), 135-140.

50. Shukla, P.; Wang, S.; Sun, H.; Ang, H.-M.; Tade, M., *Chem. Eng. J.* **2010,** *164* (1), 255-260.

51. Chen, H. T.; Huh, S.; Wiench, J. W.; Pruski, M.; Lin, V. S. Y., *J. Am. Chem. Soc.* **2005,** *127* (38), 13305-13311.

52. Fulvio, P. F.; Pikus, S.; Jaroniec, M., *J. Mater. Chem.* **2005,** *15* (47), 5049-5053.

53. Zhang, F. Q.; Yan, Y.; Yang, H. F.; Meng, Y.; Yu, C. Z.; Tu, B.; Zhao, D. Y., *J. Phys. Chem. B* **2005,** *109* (18), 8723-8732.

54. Li, C. L.; Wang, Y. Q.; Guo, Y. L.; Liu, X. H.; Guo, Y.; Zhang, Z. G.; Wang, Y. S.; Lu, G. Z., *Chem. Mater.* **2007,** *19* (2), 173-178.

55. Du, Y. C.; Lan, X. J.; Liu, S.; Ji, Y. Y.; Zhang, Y. L.; Zhang, W. P.; Xiao, F. S., *Microporous Mesoporous Mater.* **2008,** *112* (1-3), 225-234.

56. Cassiers, K.; Linssen, T.; Mathieu, M.; Benjelloun, M.; Schrijnemakers, K.; Van Der Voort, P.; Cool, P.; Vansant, E. F., *Chem. Mater.* **2002,** *14* (5), 2317-2324.

57. Igarashi, N.; Koyano, K. A.; Tanaka, Y.; Nakata, S.; Hashimoto, K.; Tatsumi, T., *Microporous Mesoporous Mater.* **2003,** *59* (1), 43-52.

58. Mokaya, R., *J. Phys. Chem. B* **1999,** *103* (46), 10204-10208.

59. Corma, A., *Chem. Rev.* **1997,** *97* (6), 2373-2419.

60. Karimi, B.; Abedi, S.; Clark, J. H.; Budarin, V., *Angew Chem Int Edit* **2006,** *45* (29), 4776-4779.

61. Jin, Y.; Wang, P. J.; Yin, D. H.; Liu, J. F.; Qiu, H. Y.; Yu, N. Y., *Microporous Mesoporous Mater.* **2008,** *111* (1-3), 569-576.

62. Chen, L. F.; Hu, J. C.; Richards, R., *J. Am. Chem. Soc.* **2009,** *131* (3), 914-915.

63. Ding, J.; Chan, K. Y.; Ren, J. W.; Xiao, F. S., *Electrochim. Acta* **2005,** *50* (15), 3131-3141.

64. Jiao, F.; Frei, H., *Angew Chem Int Edit* **2009,** *48* (10), 1841-1844.

65. Dhepe, P. L.; Fukuoka, A., *Chemsuschem* **2008,** *1* (12), 969-975.

CHAPTER 2. POLY(L-LYSINE) COATED MESOPOROUS SILICA NANOPARTICLE (PLL-MSN): SYNTHESIS, CHARACTERIZATION, AND POTENTIAL APPLICATION AS AN ORAL DRUG DELIVERY VEHICLE

A paper in preparation and to be submitted to *J. Mater. Chem.*

Wei Huang, Hung-Ting Chen, Igor Slowing, Chia-Wen Wu, and Victor S.-Y. Lin

Abstract

Poly(L-lysine) immobilized mesoporous silica nanoparticles (PLL-MSNs) were synthesized via the ring-opening polymerization of N^{ε}-(*tert*-butoxycarbonyl)-L-lysine-*N*-carboxyanhydride that grows on the surface of aminopropyl functionalized MSN. The resulting PLL-MSN is fully characterized by powder X-ray diffraction, N_2 sorption analysis, solid-state NMR, scanning electron microscopy (SEM), transmission electron microscopy (TEM), and ζ-potential analysis. All results indicate that the poly(L-lysine) forms a dense polymer layer chemically bonded on the exterior surface of the MSN. The surface charge of the MSN switches from negative to positive due to the incorporation of the polyamines on the external surface as determined by the ζ-potential study. In addition, PLL-MSN demonstrated to be easily internalized by human cervical cancer (HeLa) cells by various biological studies. The surface tethered poly(L-lysine) is resistant to digestion by pepsin but decomposed by trypsin, which makes this PLL-MSN material a promising oral drug delivery vehicle.

Introduction

Since the first report on the synthesis of MCM-41 material by the researchers in Mobil Research and Development Corporation,[1] ordered mesoporous materials have been vastly used in areas as diverse as sorption,[2-4] sensing,[5-7] catalyst support,[8-10] gene transfection,[11, 12] controlled drug-delivery systems,[13-16] etc. Due to the stable mesoporous structure, well-defined porous structure, and their biocompatibility,[11, 17-19] mesoporous silica nanoparticles (MSNs) are particularly attractive as drug delivery vehicles in the recent years. MSNs have been reported to be drug carriers applied to mice intravenously.[19, 20] However, the oral route is more preferable method of taking medicine than injection mainly due to patient's acceptance, ease of administration, and accurate dosing. One of the challenges for oral delivery is the gastrointestinal (GI) destruction of labile molecules such as enzymatic degradation of peptide or DNA.[21] In this case, the ideal carrier should be able to protect the drugs from various enzymes found in the mouth, pharynx, esophagus, and stomach as it passes through the GI tract. Since the proteolytic activity is the highest in the stomach and drugs will spend the most time in the stomach before entering the small intestine, where most molecules are absorbed into the circulation system,[22] it is critical that the drug is protected from pepsin, an enzyme produced in the stomach. While the molecules enter the small intestine, they need to be uptaken efficiently, which is a another major obstacle of oral delivery due to the low level of macromolecular absorption.[23] Recently, our group reported a controlled-release delivery system consisted of mesoporous silica nanoparticles carrying guest molecules, which are encapsulated inside the mesochannels by nanoparticle caps. These caps can protect payloads from enzymatic attack such as pepsin digestion by blocking the pore entrance to make payloads inaccessible. On the other hand, the caps of the drug

carriers should be able to dissociate quickly, which is incapable for bulky nanoparticle caps, from the encapsulating matrix to allow enough time for drug diffusion and absorption when entering the small intestine. In order to overcome these two problems, we designed the poly(L-lysine) capped mesoporous silica nanoparticles (PLL-MSN) synthesized via ring-opening polymerization initiated by the primary amino groups on the outside surface of MSN (Scheme 2-1). We envision that the poly(L-lysine) coating can resist pepsin digestion due to the slow kinetic of pepsin for unaromatic peptides under pH = 2, which keeps the pores

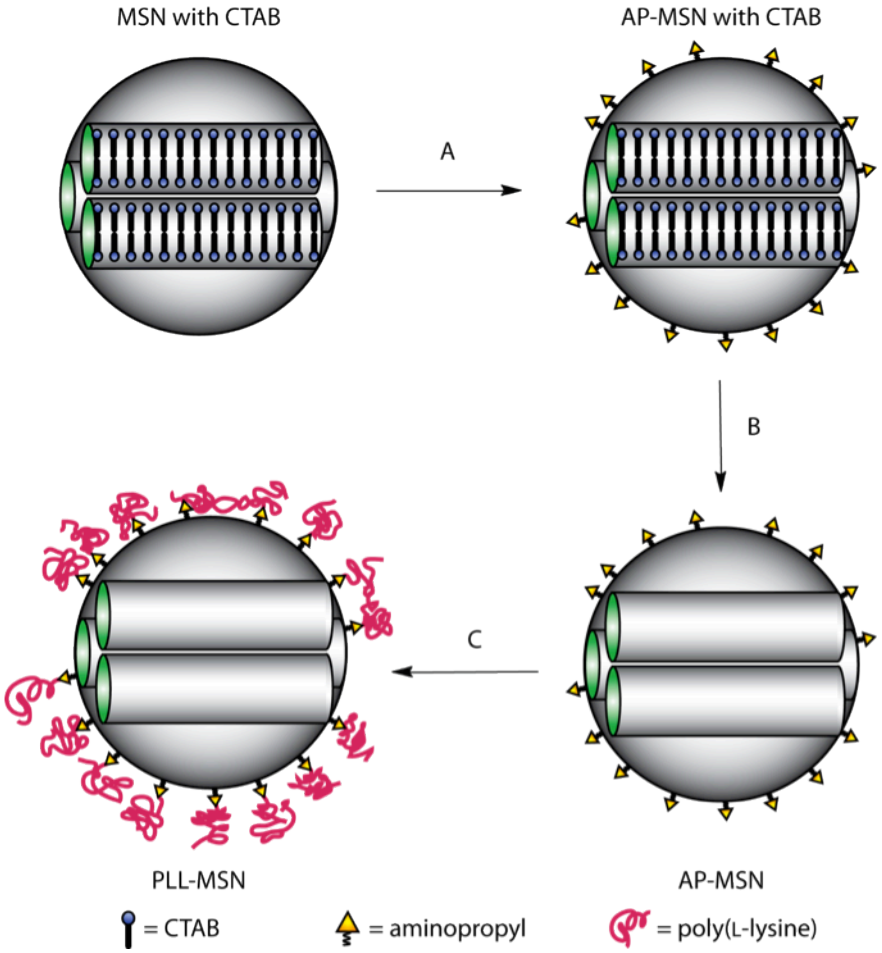

Scheme 2-1. Synthetic procedure of PLL-MSN. A.) Functionalization of MSN (with surfactant inside mesopores) by postsynthetic-grafting of 3-aminopropyltrimethoxysilane in reflux toluene. B.) Surfactant removal in methanol at acidic environment. C.) Ring-opening polymerization of N^{ε}-(*tert*-butoxycarbonyl)-L-lysine-*N*-carboxyanhydride initiated by surface amine groups to form PLL-MSN.

closed and prevents any drugs loaded inside the mesopores from proteolytic digestion. On the other hand, the polymer could be degraded by trypsin,[24] an enzyme efficient for cleavage of lysine and arginine sites and rich in the duodenum (first portion of the small intestine). Therefore, the mesopores were reopened almost completely. We envision that this PLL-MSN material can serve as a smart nano-container in the biological application such as an oral drug delivery vehicle.

Experimental section

Chemicals and reagents

Cetyltrimethylammonium bromide (CTAB), triphosgene, anhydrous *N,N*-dimethylformamide (DMF), anhydrous triethylamine (TEA), trypsin from bovine pancreas, and pepsin from porcine gastric mucosa were purchased from Sigma-Aldrich. Ethyl acetate (EtAc) was obtained from Fisher. Tetraethyl orthosilicate (TEOS) and 3-aminopropyl trimethoxysilane (APTMS) were obtained from Gelest. H-Lys(*t*-Boc)-OH was purchased from Novabiochem. All chemicals and reagents were used as received.

Synthesis of as-synthesized MSN

MSN was synthesized according to the method previously reported by our group[11] with minor modifications in the way that TEOS was added. In a typical reaction, a mixture of CTAB (1 g), 2 M NaOH (3.5 ml), and nanopure water (480 ml) was stirred at 80 °C until the surfactant was dissolved. TEOS (5 ml) was added to this clear solution by a syringe pump at a injection rate of 60 ml/h. The mixture was kept at 80 °C for 2 h. The solid

product was recovered by filtration, washed with water and methanol, and dried under vacuum to yield the as-synthesized MSN.

Synthesis of 3-aminopropyl functionalized MSN (AP-MSN)

APTMS (1mmol) was added to a toluene suspension with as synthesized MSN (1 g). The whole mixture was refluxed for 6 h under argon. The resulting material was filtered, washed with toluene and methanol, and dried under vacuum. In order to remove the CTAB, the amino-functional MSN (1 g) was refluxed in acidic methanolic solution (1ml of *conc.* HCl in 100 ml of MeOH) for 6 h. The AP-MSN was then treated with sodium bicarbonate saturated in methanol solution to deprotonate the primary amines.

Synthesis of N^{ε}-(*tert*-butoxycarbonyl)-L-lysine *N*-carboxyanhydride ((*t*-Boc)-Lys-NCA)

Our synthetic method was a slight modification (solvent) of a literature reported procedure.[25] Briefly, as shown in Scheme 2-2a, H-Lys(t-Boc)-OH (1.97 g) and triphosgene (0.8 g) were suspended in anhydrous THF (40 ml) under argon. Anhydrous TEA (0.36 ml) was added 10 min later and the whole suspension was stirred vigorously at room temperature for 15 h. The reactor mixture was then cooled down to -18 °C for 30 min after the reaction. The white precipitate was removed by filtration, and the crude product was obtained after the solvent was evaporated. The white crude product was dissolved in ice-cold EtAc and washed by ice-cold water and sodium bicarbonate (0.5%) aqueous solution separately. The organic phase was separated and dried over magnesium sulfate. After removing EtAc under the vacuum, the pure product was obtained as white powder (yield = 1.3g, 4.8 mmol, 60%).

Synthesis of poly(L-lysine) coated MSN (PLL-MSN)

As shown in Scheme 2-2b, (t-Boc)-Lys-NCA (0.54 g) was first dissolved in anhydrous DMF before it was added to the suspension of AP-MSN (0.4 g) in DMF. The reaction mixture was stirred under argon at room temperature for 24 h. The material was filtered, washed with DMF and methanol, and dried under vacuum. The *tert*-butoxycarbonyl groups were later removed by in acidic condition to yield PLL-MSN.

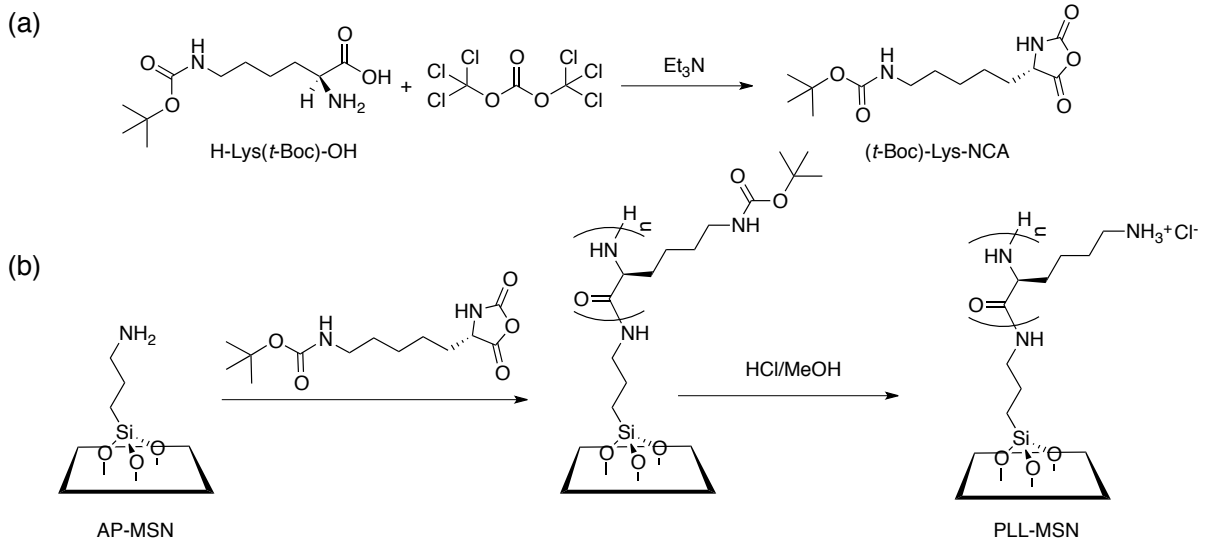

Scheme 2-2. Synthesis of (a) (*t*-Boc)-Lys-NCA by reacting *t*-Boc protected lysine and triphosgene, and (b) PLL-MSN from surface initiated ring-opening polymerization of (*t*-Boc)-Lys-NCA.

Characterization of materials

Powder X-ray diffraction patterns were obtained from a Scintag XDS 2000 X-ray diffractometer with Cu Kα radiation. BET (Brunauer-Emmett-Teller) surface area and BJH (Barrett-Joyner-Halenda) pore size data were measured on a Micromeritics TriStar 3000 analyzer at 77 K. ^{13}C-NMR data were collected from a Bruker AV-600 spectrometer. Zeta potential of the materials was taken on a Malvern Nano HT Zetasizer. Particle morphology was determined by scanning electron microscopy (SEM) using a JEOL 840A scanning

electron microscope. TEM images were collected on FEI Tecnai G^2 F20 STEM working at 200kV.

Enzyme digestion

PLL-MSN (100 mg) was suspended in pepsin aqueous solution (20 ml, 1 μM) at pH = 2 or trypsin aqueous solution (20 ml 1 μM) at pH = 7.4 respectively. The PLL-MSN material was kept at 37 °C for 8 h with pepsin and 2 h with trypsin. The material was filtered, washed with water and methanol, and dried under vacuum. The resulting materials were denoted as pepsin-PLL-MSN or trypsin-PLL-MSN.

Results and discussion

As shown in Scheme 2-1, an unfunctionalized MSN was first synthesized according to a previously published method[11] using CTAB as structure directing agent and TEOS as silica source. With surfactant inside the mesopores of the material, APTMS was grafted onto the as-synthesized MSN in refluxed toluene in inert atmosphere. This method rendered AP-MSN with the amino groups mainly located on the exterior surface and near the pore openings of the material. The surfactant was later removed by acid extraction to expose the pore channels. The powder XRD pattern of the AP-MSN exhibited three distinguished peaks as indexed in Figure 2-1, which indicated that AP-MSN had well-ordered 2D hexagonal pore structure. The SEM image (Figure 2-2) showed that AP-MSN was individual spherical particles with diameter around 150 nm, which was a suitable size for biological applications.[26] The nitrogen adsorption/desorption analysis of AP-MSN exhibited type IV isotherm (Figure 2-3), which was characteristic of mesoporous materials with cylindrical

pores. The BET surface area and pore volume were 913 m^2/g and 0.53 cm^3/g, respectively. The BJH pore size distribution indicated the existence of uniform sized mesopores with an average pore diameter of 2.4 nm. The well-ordered porous structure, controlled particle size, high surface area, large pore volume, and uniform sized mesopores were all important structural parameters for AP-MSN to be a good drug carrier.

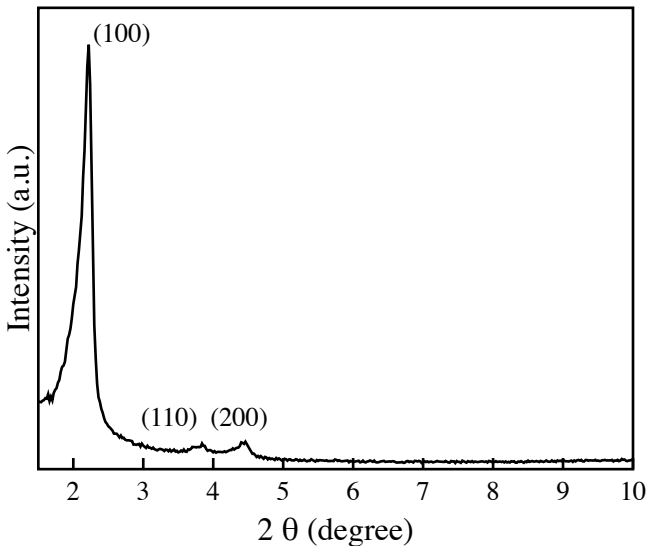

Figure 2-1. Powder XRD pattern of AP-MSN with (100), (110), and (200) indexed peaks.

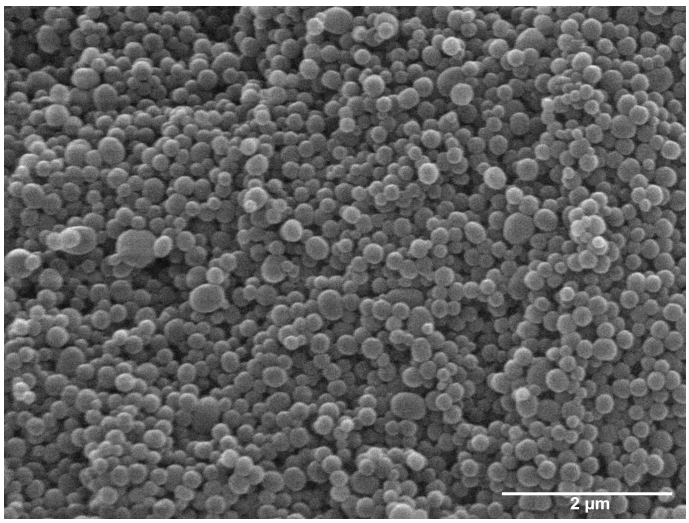

Figure 2-2. SEM micrograph of AP-MSN. Scale bar = 2 µm.

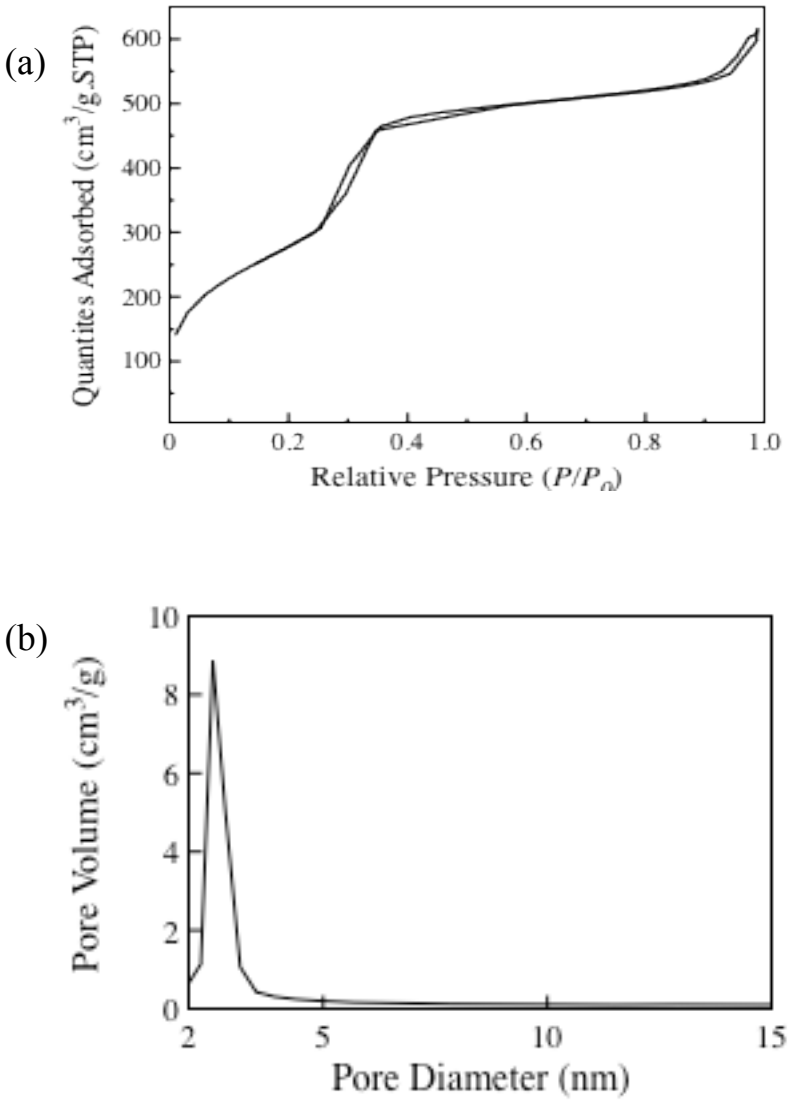

Figure 2-3. BET isotherm (a) and BJH pore size distribution (b) of AP-MSN.

To cap the pore channels of AP-MSN, we coated poly(L-lysine) on the outer surface of AP-MSN. The polymer layer was prepared via ring-opening polymerization of N^{ε}-(*tert*-butoxycarbonyl)-L-lysine-*N*-carboxyanhydride with the primary amine groups on the exterior surface of AP-MSN as the initiator. The *tert*-butoxycarbonyl protecting groups were later removed in acidic conditions to obtain the PLL-MSN.

The successful incorporation of poly(L-lysine) onto the AP-MSN was confirmed by various analyses. Figure 2-4 presented the ^{13}C solid-state NMR spectrum of PLL-MSN. The signal at 53.78 ppm was assigned to Cα carbon on the polymer backbone. The resonance from 26.85 ppm to 39.95 ppm indicated the four carbons on the lysine side chains. The

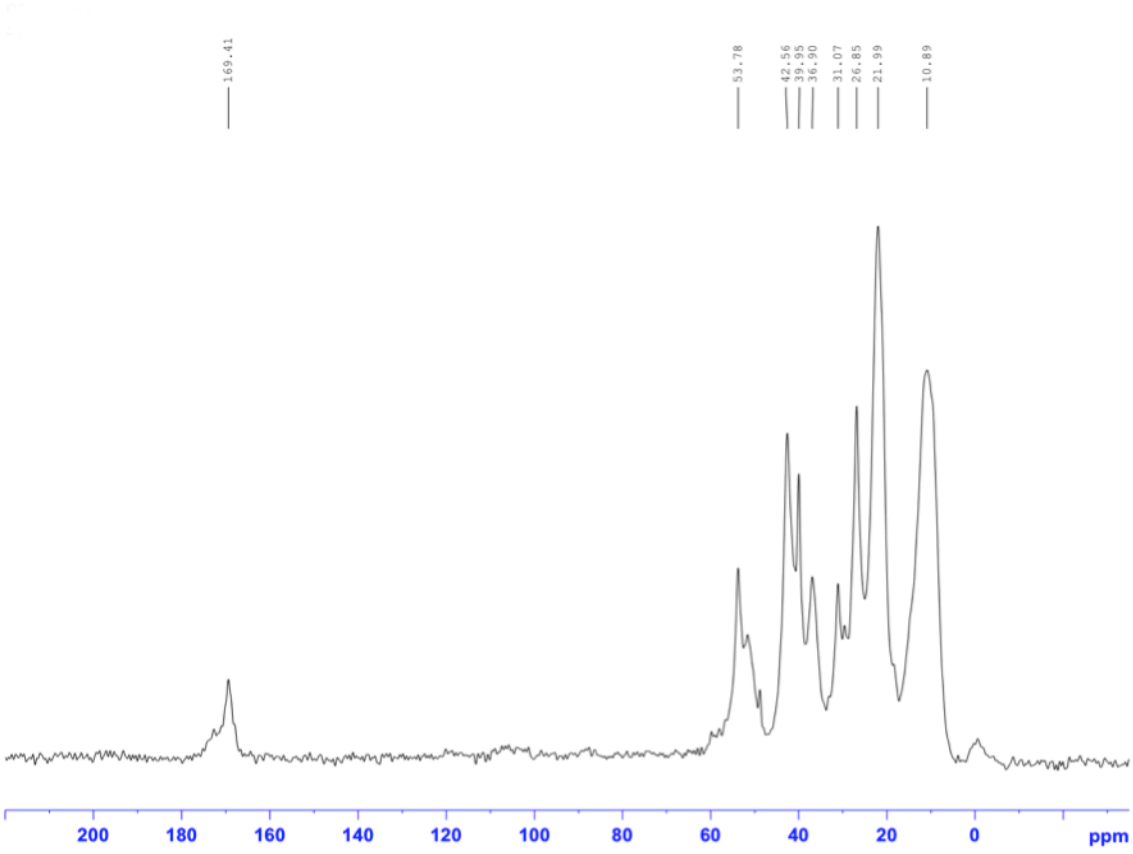

Figure 2-4. 13C solid-state CPMAS NMR spectra of PLL-MSN

broad peak centered at 169.41 ppm indicated the existence of carbonyl groups from the polymer backbone. In addition, there was no signal at 156 ppm, which showed that all *tert*-butoxycarbonyl moieties, the protecting groups of side-chain amines, were completely removed. The ^{13}C-NMR results confirmed the presence of poly(L-lysine) on PLL-MSN and free primary amines on the lysine side chains. The presence of polyamines also revealed by

the measurement of material surface charge by ζ-potential analyzer under physiological conditions. The ζ-potential of PLL-MSN dramatically increased from -20.5 mV (unfunctionalized MSN) to +21.3 mV due to the protonation of primary amines in the lysine side chains at pH = 7.4. The TEM image of PLL-MSN, as shown in Figure 2-5, revealed the pore channels of PLL-MSN represented by the parallel strips in the material and a thick polymer coating on the outside of material. The capping efficiency of the poly(L-lysine) layer was investigated by the nitrogen adsorption/desorption analysis (Figure 2-6). After the polymer was coated on the surface of AP-MSN, the surface area and pore volume dropped dramatically compared to those of AP-MSN. The BET surface area and pore volume of PLL-MSN dropped to 49 m^2/g and 0.12 cm^3/g, respectively. In addition, there was no peak shown on BJH pore size distribution graph for PLL-MSN, which indicated that the mesopores of the materials were completely blocked by the poly(L-lysine) coating. The biocompatibility and endocytosis efficiency of PLL-MSN were also studied using HeLa cells by measuring the LC_{50} (the concentration of the material that will kill 50 % of the cells) and EC_{50} (the concentration of the material needed to be internalized by half of the cells). The LC_{50} of PLL-MSN and unfunctionalized MSN were 90 μg/ml and 100 μg/ml, respectively. These numbers were close enough to say that both of the materials had the same biocompatibility. However, The EC_{50} of PLL MSN (0.25 μg/ml) was much lower than that of unfunctionalized MSN (12 μg/ml), indicating the polymer coverage significantly increased the endocytosis efficiency due to enhancement of cell adhesion by polyamines on the surface.[27]

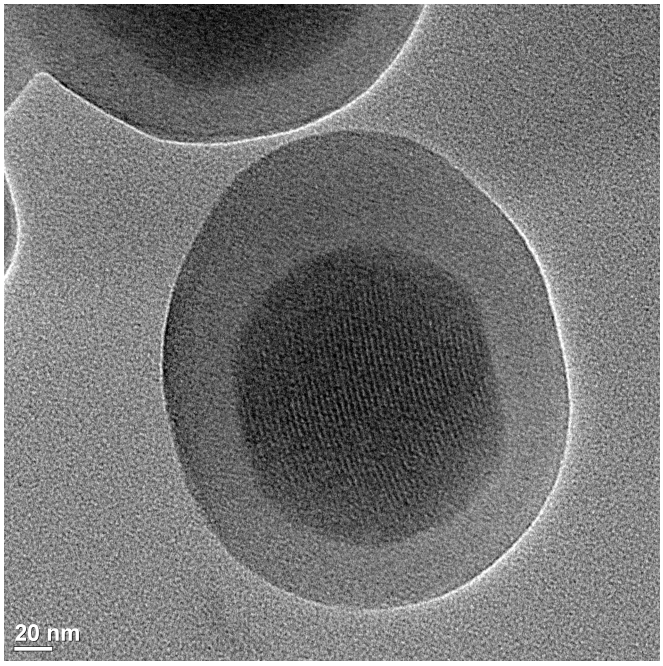

Figure 2-5. TEM micrograph of PLL-MSN. The outer layer on the MSN represents surface coated poly(L-lysine) polymer. Scale bar = 20 nm

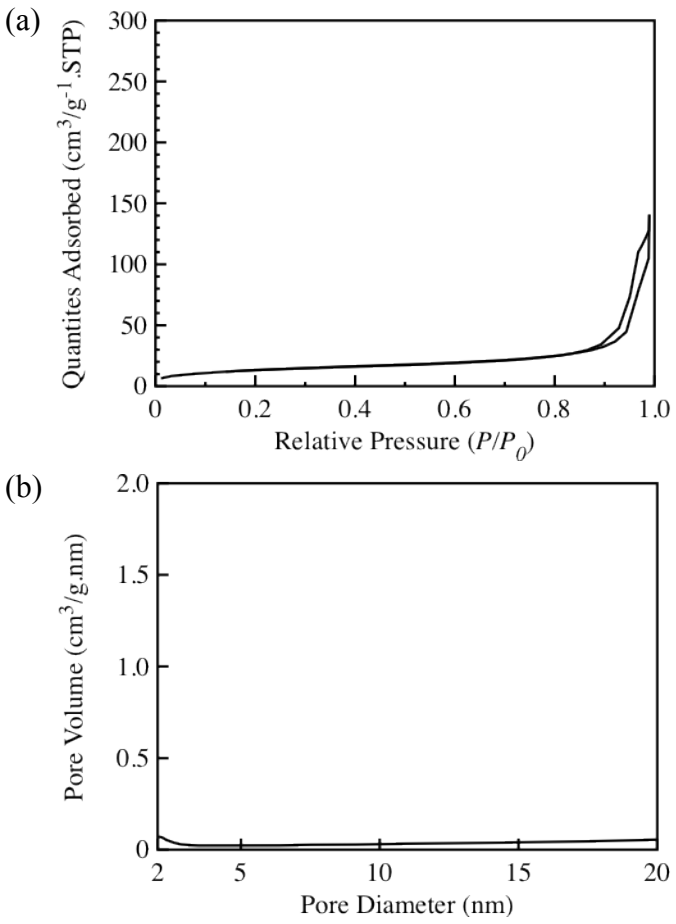

Figure 2-6. BET isotherm (a) and BJH pore size distribution (b) of PLL-MSN.

PLL-MSN was treated with two different enzymes: pepsin and trypsin. Pepsin and trypsin were chosen since they are two important enzymes and have the highest proteolytic activities throughout GI tract. PLL-MSN was stirred with pepsin at pH = 2 for 8 h, which exceeded the average transit time of 4 h to pass through the stomach. The nitrogen sorption analysis indicated pepsin-PLL-MSN had similar BET surface area (47 m^2/g) and pore volume (0.13 cm^3/g) as that of PLL-MSN, and no detectable pore structure was observed in the pepsin-PLL-MSN from the diagram of BJH pore size distribution (Figure 2-7). The results indicated that the polymer layer could not be hydrolyzed by pepsin. Under acidic conditions, pepsin specifically cleaved peptide bonds between hydrophobic amino acids such as tyrosine, tryptophan, and phenylalanine, but it could not hydrolyze highly hydrophilic peptides such as poly(L-lysine). As a result, poly(L-lysine) could remain intact during contact with pepsin. In contrast, trypsin is an enzyme that specifically cleaves the carboxyl end of lysines.[28] PLL-MSN treated with trypsin for 2 h under physiological condition showed a large increase in BET surface area (887 m^2/g) and pore volume (0.48 cm^3/g). 97 % of the surface area and 91 % of the pore volume were recovered after suspended in the trypsin solution. From BJH analysis, trypsin-PLL-MSN had a pore size of 2.0 nm in diameter, indicating that the mesopores of the material were uncapped after the exterior polymer layer was degraded by trypsin. These results demonstrate the potential of PLL-MSN as an oral drug carrier, since the pore channels remain capped at low pH in the presence of pepsin, but reopen through digestion of poly(L-lysin) by trpsin in the intestine, where drugs were released and could be absorbed efficiently into the circulation system.

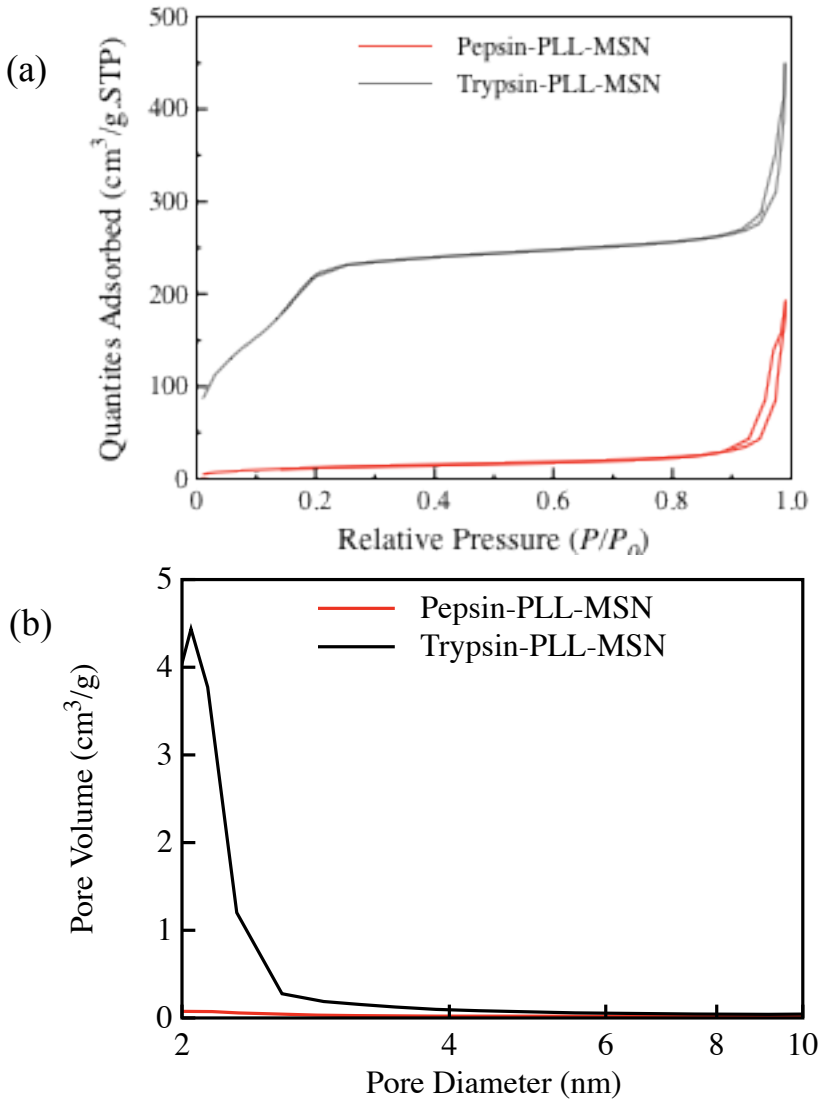

Figure 2-7. BET isotherms (a) and BJH pore size distributions (b) of PLL-MSN treated with pepsin and trypsin, respectively.

Conclusions

Poly(L-lysin) coated mesoporous silica nanoparticles has been successfully synthesized and fully characterized by various analytic techniques. The poly(L-lysine) acted as a smart cap that could only be degraded by trypsin under physiological condition and not by pepsin at acidic environment. We envision PLL-MSN can serve as a potential oral drug delivery vehicle.

References:

1. Kresge, C. T.; Leonowicz, M. E.; Roth, W. J.; Vartuli, J. C.; Beck, J. S., *Nature* **1992,** *359* (6397), 710-712.
2. Feng, X.; Fryxell, G. E.; Wang, L. Q.; Kim, A. Y.; Liu, J.; Kemner, K. M., *Science* **1997,** *276* (5314), 923-926.
3. Dai, S.; Burleigh, M. C.; Shin, Y.; Morrow, C. C.; Barnes, C. E.; Xue, Z. L., *Angew Chem Int Edit* **1999,** *38* (9), 1235-1239.
4. Brown, J.; Mercier, L.; Pinnavaia, T. J., *Chem. Commun.* **1999,** (1), 69-70.
5. Radu, D. R.; Lai, C. Y.; Wiench, J. W.; Pruski, M.; Lin, V. S. Y., *J. Am. Chem. Soc.* **2004,** *126* (6), 1640-1641.
6. Yamada, T.; Zhou, H. S.; Uchida, H.; Tomita, M.; Ueno, Y.; Ichino, T.; Honma, I.; Asai, K.; Katsube, T., *Adv. Mater.* **2002,** *14* (11), 812-815.
7. Stein, A., *Adv. Mater.* **2003,** *15* (10), 763-775.
8. Chen, H. T.; Huh, S.; Wiench, J. W.; Pruski, M.; Lin, V. S. Y., *J. Am. Chem. Soc.* **2005,** *127* (38), 13305-13311.
9. Ying, J. Y.; Mehnert, C. P.; Wong, M. S., *Angew Chem Int Edit* **1999,** *38* (1-2), 56-77.
10. Corma, A., *Chem. Rev.* **1997,** *97* (6), 2373-2419.
11. Radu, D. R.; Lai, C. Y.; Jeftinija, K.; Rowe, E. W.; Jeftinija, S.; Lin, V. S. Y., *J. Am. Chem. Soc.* **2004,** *126* (41), 13216-13217.
12. Trewyn, B. G.; Whitman, C. M.; Lin, V. S. Y., *Nano Lett.* **2004,** *4* (11), 2139-2143.
13. Trewyn, B. G.; Slowing, I. I.; Giri, S.; Chen, H. T.; Lin, V. S. Y., *Acc. Chem. Res.* **2007,** *40* (9), 846-853.

14. Wang, S. B., *Microporous Mesoporous Mater.* **2009,** *117* (1-2), 1-9.

15. Manzano, M.; Vallet-Regi, M., *J. Mater. Chem.* **2010,** *20* (27), 5593-5604.

16. Coti, K. K.; Belowich, M. E.; Liong, M.; Ambrogio, M. W.; Lau, Y. A.; Khatib, H. A.; Zink, J. I.; Khashab, N. M.; Stoddart, J. F., *Nanoscale* **2009,** *1* (1), 16-39.

17. Slowing, I.; Trewyn, B. G.; Lin, V. S. Y., *J. Am. Chem. Soc.* **2006,** *128* (46), 14792-14793.

18. Liu, H. M.; Wu, S. H.; Lu, C. W.; Yao, M.; Hsiao, J. K.; Hung, Y.; Lin, Y. S.; Mou, C. Y.; Yang, C. S.; Huang, D. M.; Chen, Y. C., *Small* **2008,** *4* (5), 619-626.

19. Lu, J.; Liong, M.; Li, Z. X.; Zink, J. I.; Tamanoi, F., *Small* **2010,** *6* (16), 1794-1805.

20. Hudson, S. P.; Padera, R. F.; Langer, R.; Kohane, D. S., *Biomaterials* **2008,** *29* (30), 4045-4055.

21. Morishita, M.; Peppas, N. A., *Drug Discovery Today* **2006,** *11* (19-20), 905-910.

22. Singh, R.; Singh, S.; Lillard, J. W., *J. Pharm. Sci.* **2008,** *97* (7), 2497-2523.

23. Francis, M. F.; Cristea, M.; Winnik, F. M., *Pure Appl. Chem.* **2004,** *76* (7-8), 1321-1335.

24. Miller, W. G., *J. Am. Chem. Soc.* **1964,** *86* (19), 3918-&.

25. Hernandez, J. R.; Klok, H.-A., *Journal of Polymer Science, Part A: Polymer Chemistry* **2003,** *41* (9), 1167-1187.

26. Muggia, F. M., *Clin Cancer Res* **1999,** *5* (1), 7-8.

27. Deng, C.; Chen, X. S.; Yu, H. J.; Sun, J.; Lu, T. C.; Jing, X. B., *Polymer* **2007,** *48* (1), 139-149.

28. Waley, S. G.; Watson, J., *Biochem. J* **1953,** *55* (2), 328-337.

CHAPTER 3. CONVERSION OF CELLULOSE TO POLYOLS BY PLATINUM NANOPARTICLE FUNCTIONALIZED MESOPOROUS SILICA NANOPARTICLES

A paper in preparation and to be submitted to *Green Chemistry*

Wei Huang, Yulin Huang, Hirokazu Kobayashi, Atsushi Fukuoka, Brian G. Trewyn, Hung-Ting Chen, and Victor S.-Y. Lin

Iowa State University and Ames Laboratory

Abstract

A series of platinum nanoparticles immobilized mesoporous silica nanoparticles (Pt NP-MSNs) have been synthesized using N-(2-aminoethyl)-3-aminopropyl (AAP-) and 3-[2-(2-aminoethylamino)ethylamino]propyl (AEP-) functionalized MSNs as solid supports. Platinum nanoparticles were anchored on the MSNs by complexation of a Pt precursor to surface amino-functional groups followed by metal reduction. Pt NP-MSNs have been fully characterized by various material analysis techniques including powder X-ray diffraction, nitrogen sorption, transmission electron microscopy, scanning electron microscopy, and solid state NMR. We have also demonstrated that these Pt NP-MSNs assisted in the degradation of cellulose producing sorbitol and mannitol and discovered that both Pt nanoparticles and the mesoporous silica support affect the reaction yield.

Introduction

The urgent demands to reduce the dependence on petroleum oil and increase the utilization of bio-renewable energy resources for production of valuable chemicals have induced significant research activities in catalysis. Currently, finding a reactive catalyst that can efficiently convert biomass, especially non-food based cellulose, into valuable chemicals used in everyday life is of great interest.[1-8] Cellulose is the main structural component in the primary cell walls of higher order plants. Given that about 33% ~ 40% of plants on earth is made by cellulose, it is by far the most abundant organic compound in nature.[9] Basically, cellulose is a bio-polymer produced by photosynthesis, which consists of *D*-glucose as the repeating unit conjugated by β-(1,4)-glycosidic bonds.[4, 10, 11] This unique β-(1,4)-glycosidic linkage imparts the structural rigidity to a single cellulose chain, which further forms a semi-crystalline fibril through a complicated intra- and inter-molecular multiple hydrogen-bonded network. Because of these intertwined hydrogen bonds, cellulose has low solubility in most common solvents, which significantly reduces its vulnerability to attack by chemical reagents.

Several approaches have been persued in the conversion of cellulose to polyols such as acid-catalyzed hydrolysis,[12-14] supercritical fluid assisted degradation,[15] and fermentation catalyzed by wild type or genetic engineered cellulases.[16] However, most chemical and physical conversion methods suffer from low selectivity of products; whereas enzymatic methods has challenges related to high cost and minimal recyclability due to the instability of enzymes. Recently, Fukuoka and co-workers first reported a novel solid catalyst consisting of platinum metal deposited on aluminum oxide supports, which could simultaneously depolymerize cellulose and further reduce it into hexitols (sorbitol and mannitol) in the

presence of hydrogen as depicted in Scheme 3-1.[17-19] This study opens up a new direction of using metal loaded solid material as heterogeneous catalysts for cellulose conversion to polyols. This Pt/γ-Al_2O_3 catalytic system produced hexitols, sorbitol and mannitol, with the reaction yield of 31%. More recently, Liu and co-workers discovered that ruthenium on active carbon could also catalyze this conversion to polyols with slightly better yield (39.3%) at an elevated hydrogen pressure and reaction temperature.[20] It was first proposed by Liu and now generally accepted that the hydronium ion generated from water *in-situ* at elevated temperature catalyze the hydrolysis of cellulose in this system. Zhang and co-workers unveiled another bimetallic system, active carbon supported nickel and tungsten carbide (Ni-W_2C/AC), which selectively converted cellulose to ethylene glycol with excellent yield (61%).[21-23] In spite of all these efforts devoted to heterogeneous catalysis for cellulose conversion, little attention has been paid to controlling the size of the immobilized metal and the effect of supported materials on the conversion. To address these important reaction conditions, we investigated well-ordered mesoporous silica nanoparticles (MSNs) with large surface area capable for metal deposition and highly accessible porous structure as potentially suitable solid support.

Herein, we report the synthesis of a mesoporous silica nanoparticle catalyst

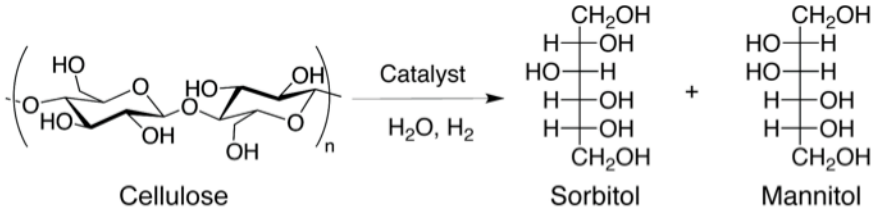

Scheme 3-1. Catalytic conversion of cellulose to hexitols (sorbitol and mannitol).

functionalized with well-distributed platinum nanoparticles for the conversion of cellulose to hexitols in the presence of hydrogen gas. The platinum nanoparticles were generated *in-situ* by chemical fixation of the platinum precursor with the surface amine group, which was pre-functionalized on the MSN surface, followed by sequential oxidation and reduction. The reaction mechanism of cellulose conversion was also investigated and detailed below.

Experimental section

Chemicals and reagents. Cetyltrimethylammonium bromide (CTAB) and cellulose were purchased from Sigma-Aldrich. Chloroplatinic acid hexahydrate was purchased from Strem Chemicals Inc. Ball-milled cellulose was obtained from Hokkaido University. Tetraethyl orthosilicate (TEOS), N-(2-aminoethyl)-3-aminopropyltrimethoxysilane (AAPTMS), and 3-[2-(2-aminoethylamino)ethylamino]propyltrimethoxysilane (AEPTMS) were obtained from Gelest. All chemicals and reagents were used as received.

Synthesis of platinum nanoparticles immobilized MSNs (Pt-AAP-x and Pt-AEP-x). Chloroplatinic acid hexahydrate was used as platinum precursor to form platinum complexes with surfactant-free AAP-MSNs or AEP-MSNs, which were synthesized according to a previous published procedure.[24] The loading of amino functional group was determined to be 0.50 mmol/g for the AAP-MSN and 0.71 mmol/g for the AEP-MSN by 29Si solid-state NMR measurement. The initial introduced molar ratio between platinum and amine groups was 0.3, 0.6, and 1.0. For example, chloroplatinic acid hexahydrate (39 mg, Pt : $-NH_2$ = 0.3 : 1 (mol : mol)) dissolved in MeOH/H_2O (1:1, 10 ml) was added to AAP-MSN (500 mg). The mixture was stirred for 24 h at room temperature. The material was recovered by filtration, washed by H_2O and MeOH, and dried over vacuum. The dry sample

was calcined in O_2 at 400 °C for 2 h and was reduced in H_2 at 400 °C for another 2 h to yield the Pt-AAP-0.3.

Catalyzed cellulose degradation reaction. The ratio of substrate to catalyst (S/C) was kept at 100 (S = mol of $C_6H_{10}O_5$, C = mol of Pt). In a typical reaction, cellulose (80 mg), Pt-AAP-0.3 (31.8 mg), and nanopure water (10 ml) were charged in a stainless steel autoclave pressurized with 700 psi H_2. The reaction was kept at 190 °C for 7 h with constant stirring. At the end of the reaction, the mixture was centrifuged, and the filtered solution was analyzed by HPLC. To determine recyclability, the solid was collected after centrifugation, dried under vacuum, and reused at the same reaction conditions without further treatment. Other reaction conditions (such as reaction time and temperature) were also tested and the results were described in the results and discussion section.

Characterization. Powder X-ray diffraction patterns were obtained from a Scintag XDS 2000 X-ray diffractometer with Cu Kα radiation. Nitrogen sorption analysis was conducted on a Tristar 3000 Sorptometer. The surface area and pore volume/pore size distribution were calculated by the Brunauer-Emmett-Teller (BET) and Barrett-Joyner-Halenda (BJH) methods, respectively. Scanning electron microscopy (SEM) images were taken using a JEOL 840A scanning electron microscope. Transmission electron microscopy (TEM) images were collected on FEI Tecnai G^2 F20 STEM working at 200kV. The amount of Pt was quantified on the Hewlett-Packard 4500 ICP-MS. The degradation products were analyzed by using a Rezex RPM-monosaccharide Pb^{2+} (Phenomonex®) column on a Varian Prostar HPLC equipped with a reflective index detector.

Result and Discussion

We first synthesized two types of amino-functionalized mesoporous silica nanoparticles, N-(2-aminoethyl)-3-aminopropyl (AAP) or 3-[2-(2-aminoethylamino)ethylamino]propyl (AEP) groups according to previously reported co-condensation methods as illustrated in Scheme 3-1. These amino-functional MSN were utilized as solid supports for the immobilization of platinum nanoparticles (Pt NPs). These tethered amino groups were intentionally introduced for complexation with a chloroplatinic acid hexahydrate ($H_2PtCl_6 \cdot 6H_2O$) in various amounts to form a surface immobilized platinum complex localized on the silica surface. The resulting material was later subjected to be oxidized at 400 °C under oxygen atmosphere and then be reduced with a hydrogen flow at the same temperature to yield well-defined platinum nanoparticles - immobilized MSN materials (Pt NP-MSNs). For simplification, the Pt NP-MSNs are denoted as Pt-AAP-x or

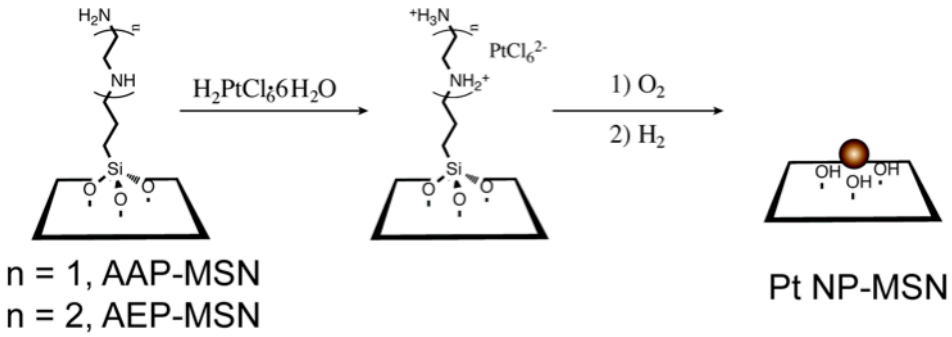

Scheme 3-1. Synthesis of platinum nanoparticle immobilized mesoporous silica nanoparticles (Pt NP-MSNs) using amino-functionalized MSNs reacted with $H_2PtCl_6 \cdot 6H_2O$, followed by sequentially oxidation and reduction.

AEP-x, by which the x (= 0.3, 0.6, or 1.0) represents the introduced molar ratio of $H_2PtCl_6 \cdot 6H_2O$ *versus* surface amine groups, whose loading were estimated by ^{29}Si solid-state

NMR spectra about 0.50 and 0.71 mmol/g for the Pt-AAP and the Pt-AEP materials, respectively.

The electron micrographs of organic functionalized AAP-MSN and AEP-MSN exhibited tubular particles with hexagonally packed mesopores and spherical morphology with worm-like porous structure as reported in the literature, respectively.[24] The Pt NP-MSNs synthesized from AAP-MSNs and AEP-MSNs maintained the same particle morphologies as their parent silicas as shown in SEM images (Figure 3-1a and b). The TEM micrographs (Figure 3-1c and d) of Pt NP-AAP showed a hexagonal mesopore array; whereas the image of Pt NP-AEP expressed worm-hole type porous structure. This result demonstrated that the mesostructure was preserved during multiple chemical treatments and was further confirmed by X-ray diffraction as detailed in Figure 3-S1. The dark dots in Figure 3-1 (c) and (d) represents small Pt NPs distributed among the silica support that was detected by EDX analysis in the region of interest. Clearly, using this surface complexation approach restricts the mobility of platinum species on the silica surface that prevents agglomeration of Pt NPs as evidenced from the individually isolated Pt NPs. We observed that the size of Pt NPs also depends on the mesoporous structure of individual parent materials. The Pt NPs anchored on the AAP-MSNs were much smaller (2 nm) than those on the AEP-MSNs (13 nm). This could be attributed to the different confinement to the immobilized Pt complex provided by dissimilar porous structures.

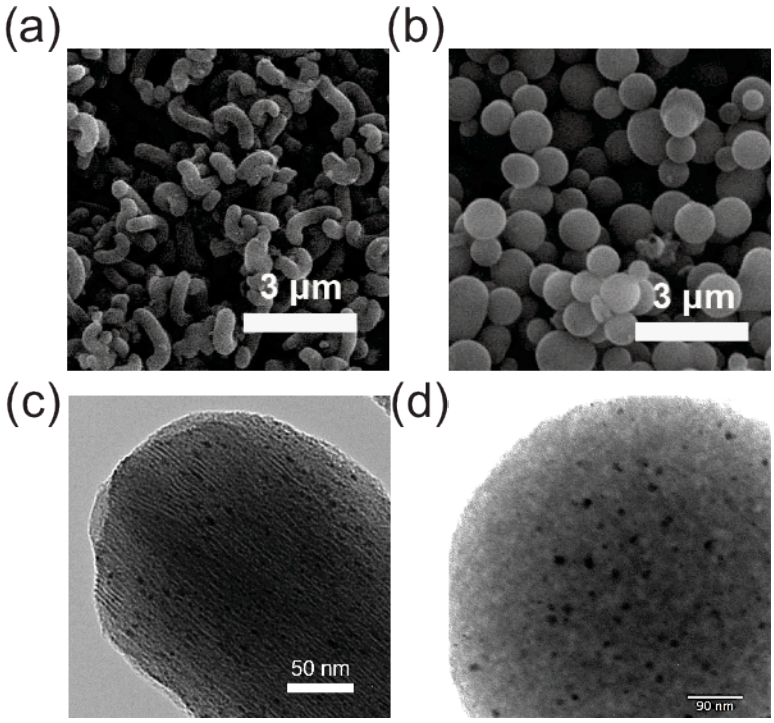

Figure 3-1. SEM micrographs of Pt NP-MSNs synthesized from AAP-MSNs (a) and AEP-MSNs (b), scale bar = 3 µm. The TEM image of Pt NP-MSNs synthesized from AAP-MSNs (c) and AEP-MSNs (d), scale bar = 50 nm and 90 nm, respectively. The dark spots in the materials represent platinum nanoparticles immobilized on the porous silica supports.

The textural properties of Pt NP-MSNs and the amount of loaded Pt NPs in the MSNs were summarized in the Table 3-1. All N_2 sorption analyses of Pt NP-MSNs showed type IV isotherm representing cylindrical mesopores. The Pt NP-MSNs were treated with hydrofluoric acid and hydrochloric acid to completely dissolve the solid for determination of Pt loading on the MSNs by the inductively coupled plasma-mass spectroscopy (ICP-MS). The loading of Pt reached their maximum after the introduction ratio of Pt/Si was larger than 0.6.

Table 3-1. Textural properties of Pt-MSNs and the loading of Pt NPs on MSNs.

Materials	Surface area (m^2/g)	Pore volume (cm^3/g)	Average pore size (nm)	Pt loading (wt%)[a]
Pt-AAP-0.3	770.6	0.5	2.6	2.75 (2.90)
Pt-AAP-0.6	766.2	0.5	2.6	3.27 (5.79)
Pt-AAP-1.0	747.9	0.5	2.6	3.24 (9.66)
Pt-AEP-0.3	680.7	0.62	3.0	3.23 (4.13)
Pt-AEP-0.6	709.1	0.64	3.0	7.08 (8.25)
Pt-AEP-1.0	711.2	0.64	3.0	6.45 (13.76)

[a.] The amount of platinum was calculated from ICP-MS. The number in parenthesis represents the initial introduction amount of platinum.

To investigate what factors influence the reaction yield of hexitols, post-treatment of cellulose, reaction temperature, and reaction time were chosen to optimize reaction condition. As shown in Figure 3-2, the cellulose milled by ZrO_2 balls was converted more efficiently to products comparing with conventional cellulose (Aldrich) using either Pt NP-AAPs or Pt NP-AEPs as catalysts. This result can be related to the dramatic decrease of crystallinity and particle size of cellulose after the ball-milling process that provides more accessible sites on the cellulose surface to be reached by the Pt NP-MSN catalyst as shown in the Supporting Information.

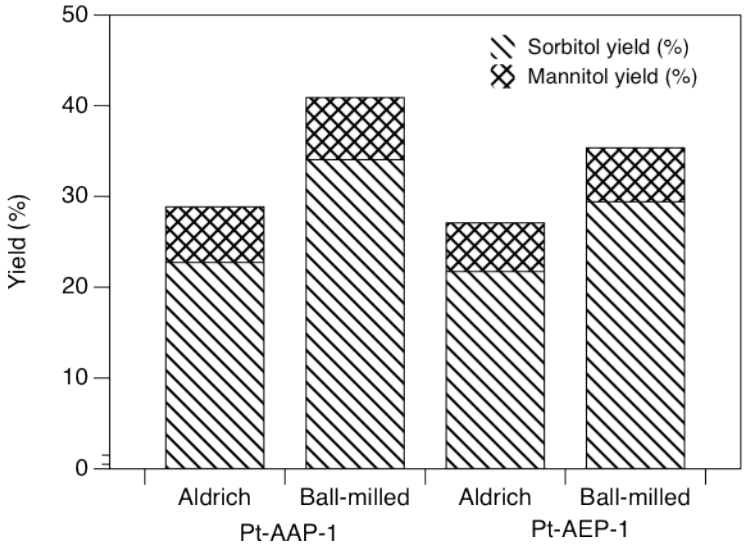

Figure 3-2. Reaction yield of sorbitol and mannitol obtained using different cellulose sources (conventional and ball-milled) catalyzed by the Pt-AAP-1 material (left two bars) and catalyzed by the Pt-AEP-1 material (right two bars).

The Figure 3-3 represented a plot of the hexitol conversion (sorbitol and mannitol) as a function of reaction time and temperature. Less than 10 % reaction yield was observed while the reaction was conducted at 150 °C indicating that Pt NP-MSNs did not efficiently catalyze cellulose degradation at this temperature. Increasing the temperature to 190 °C provided better results where the maximized yield was obtained at 7 h. The reaction performed at longer times gave a lower yield due to the further degradation of the desired products. Given the aforementioned study, the following reaction was conducted using ball-milled cellulose as substrates at 190 °C for 7 h to compare catalytic activity of Pt NP-MSNs.

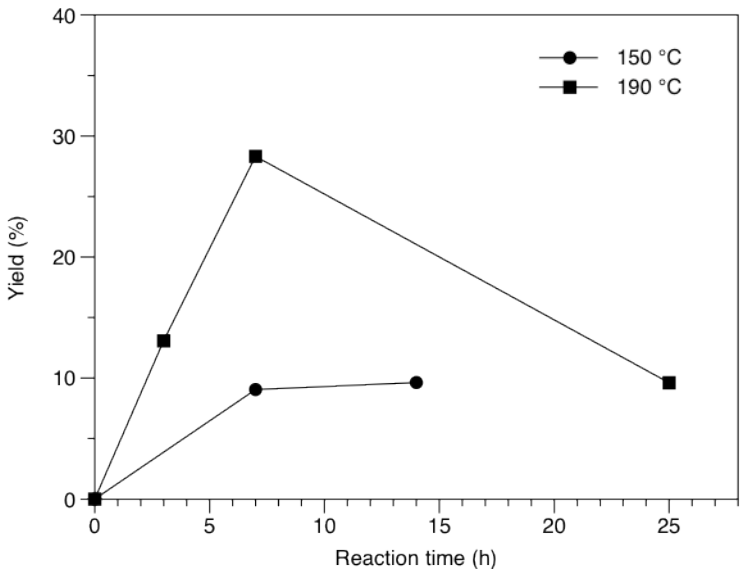

Figure 3-3. Total reaction yield of hexitols conducted at temperature of 150 °C and 190 °C, respectively, at different reaction time using Pt-AAP-0.6 as the catalyst.

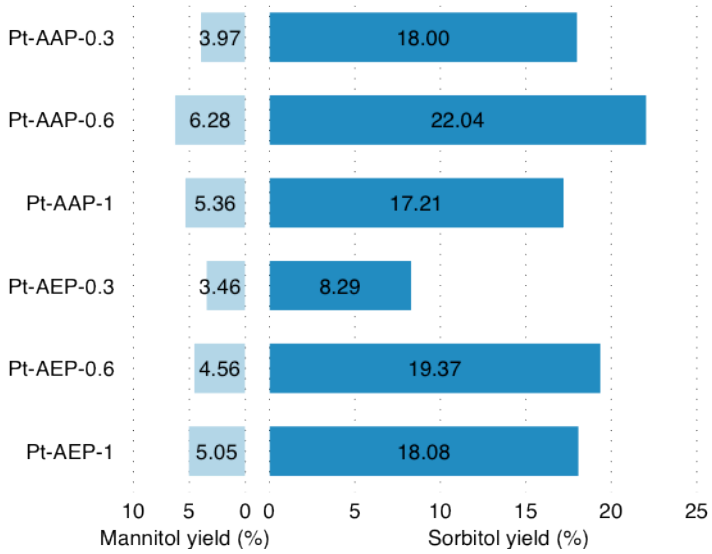

Figure 3-4. The yield of conversion of ball-milled celluloses to sorbitol and mannitol catalyzed by six different Pt NP-MSNs.

The Figure 3-4 shows the results of cellulose conversion catalyzed by 1 mol% Pt NP-MSN catalysts (based on the amount of platinum) reported as the individual yield of sorbitol and mannitol. The sorbitol yield was higher than that of mannitol with ratio of 3.58 ± 0.76.

The Pt-AAP materials catalyzed reactions more efficiently than the corresponding Pt-AEP counterpart. This result could be rationalized by the finer size of Pt NPs in Pt-AAPs than Pt-AEPs as indicated in Figure 3-1 (c) and (d). Pt-AAP-0.6 was found to offer the highest yield of sorbitol (22%) and mannitol (6.3%) among all Pt NP-MSNs of examined.

It was determined that the ball-milling created cellulose networks in the micrometer size range, yet the Pt NP encapsulated inside the MSNs catalyzed the cellulose conversion. To investigate this interesting phenomenon, cellulose was reacted with or without the non-functionalized MSN at the same conditions. Only some hydrolyzed products of cellulose, but no hexitols, were observed in both experiments due to the absence of Pt NPs. As shown in Figure 3-5, the reaction catalyzed by pure mesoporous silica yielded more erythritol and cellotriose (trimer of glucose) compared to the control with no silica. This result indicated that the pure MSN assisted in the hydrolysis of cellulose to oligomers under the reaction conditions. To verify the importance of the mesoporous silica support in the reaction, the same reactions were also performed either using Pt NPs, obtaining after dissolution of Pt-AAP-0.6 by HF, or a physical mixture of Pt NPs and pure MSNs as catalysts. Low yield of products was obtained in both reaction as indicated in Figure 3-6, which demonstrated that the mesoporous silica was essential to physically prevent Pt NPs from agglomeration that resulted in a decrease of yield during the reaction.

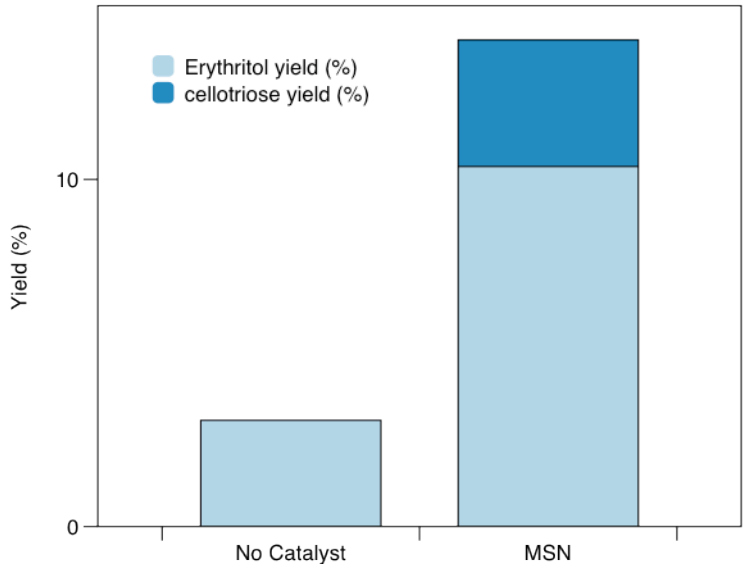

Figure 3-5. The yields of cellulose conversion catalyzed without and with the pure MSN materials. Only erythritol and cellotriose were observed in the product mixture.

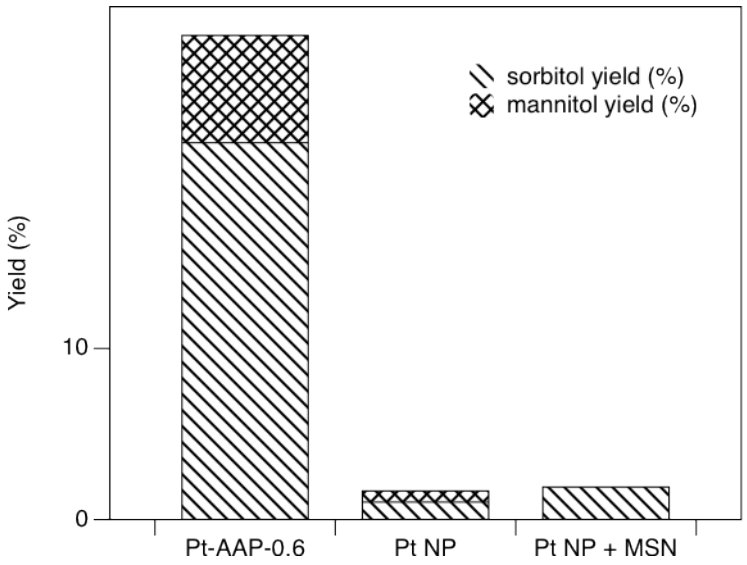

Figure 3-6. The control experiments of cellulose conversion catalyzed by platinum nanoparticles obtained after dissolution of porous silica supports and a physical mixture of the composition of platinum nanoparticles and pure MSNs, respectively.

Combining our aforementioned observations, we propose a mechanism of cellulose depolymerization and conversion to hexitols catalyzed by the Pt NP-MSN. The silica, unlike its usual role as an inert support, and Pt NPs worked synergistically to convert cellulose to

hexitols. The cellulose was first broken down into smaller oligomers with the assistance of silica and then hydrolyzed to form glucose. Finally, the glucose was further catalytically reduced by Pt nanoparticles under hydrogen atmosphere as illustrated in Figure 3-7.

In addition, we investigated the recyclability of these Pt NP-MSN catalysts. As shown in Figure 3-S2, the reaction yields using Pt-AEP-0.6 catalyst considerably dropped in three successive runs in reactions conducted at 190 °C for 24 h. In contrast, the results showed that the Pt-AAP-0.6 catalyst was able to be recycled three times with only a slight decrease in reaction yield when the reaction time was shortened to 7 h.

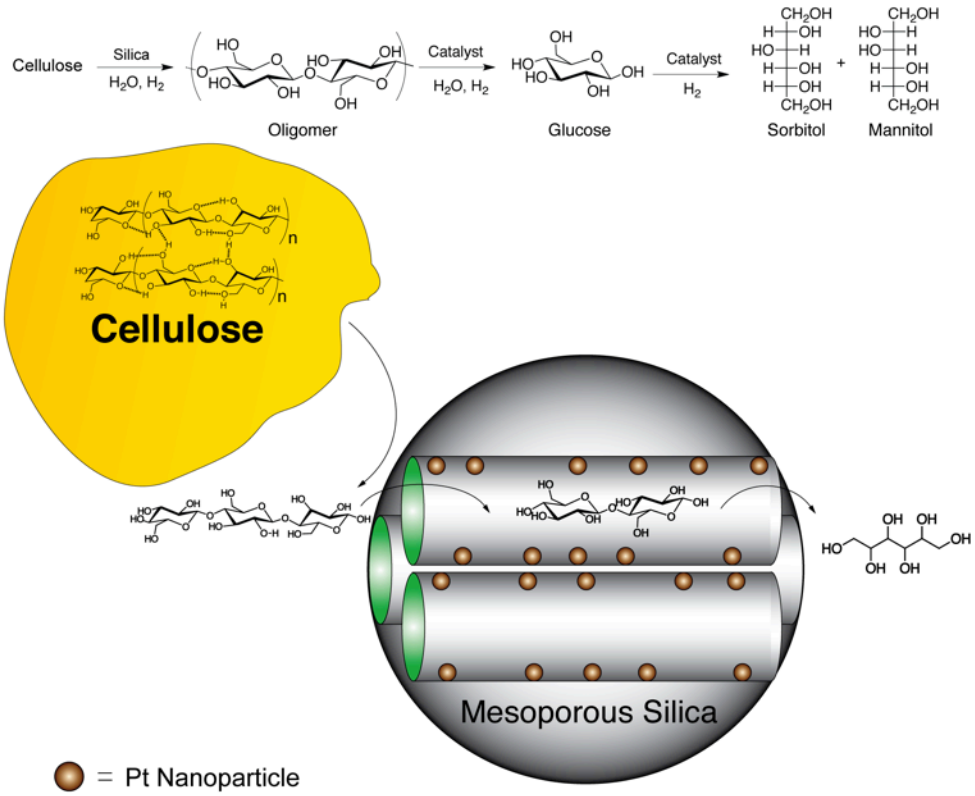

Figure 3-7. The proposed reaction mechanism of cellulose conversion catalyzed by Pt NP-MSNs.

Conclusion

In summary, we have synthesized, characterized, and applied Pt NP-MSNs as catalysts for the cellulose conversion to polyols. We discovered that the silica support promoted the degradation of cellulose to oligomers, followed by the reduction catalyzed by Pt NPs to yield sorbitol and mannitol. In summary, the Pt NP-MSN served as a dual functional catalyst that worked synergistically converting cellulose to high-valued products.

Reference

1. Chheda, J. N.; Huber, G. W.; Dumesic, J. A., *Angew. Chem. Int. Ed.* **2007,** *46*, 7164-83.
2. Stöcker, M., *Angew. Chem. Int. Ed.* **2008**.
3. Huber, G.; Corma, A., *Angew. Chem. Int. Ed.* **2007,** *46*, 7184-7201.
4. Huber, G. W.; Iborra, S.; Corma, A., *Chem. Rev.* **2006,** *106*, 4044-98.
5. Mascal, M.; Nikitin, E. B., *Green Chemistry* **2010,** *12*, 370-373.
6. Ragauskas, A. J.; Williams, C. K.; Davison, B. H.; Britovsek, G.; Cairney, J.; Eckert, C. A.; Frederick, W. J.; Hallett, J. P.; Leak, D. J.; Liotta, C. L.; Mielenz, J. R.; Murphy, R.; Templer, R.; Tschaplinski, T., *Science* **2006,** *311*, 484-9.
7. Rinaldi, R.; Schueth, F., *Energy & Environmental Science* **2009,** *2*, 610-626.
8. Tanksale, A.; Beltramini, J. N.; Lu, G. M., *Renewable & Sustainable Energy Reviews* **2010,** *14*, 166-182.
9. Fan, L. T.; Gharpyray, M. M.; Lee, Y.-H., *Cellulose Hydrolysis*. Springer: Berlin, 1987.
10. Robinson, J. M.; Burgess, C. E.; Bently, M. A.; Brasher, C. D.; Horne, B. O.; Lillard, D. M.; Macias, J. M.; Mandal, H. D.; Mills, S. C.; O'Hara, K. D.; Pon, J. T.; Raigoza, A. F.; Sanchez, E. H.; Villarreal, J. S., *Biomass & Bioenergy* **2004,** *26*, 473-483.
11. Sharkov, V. I., *Angew. Chem. Int. Ed.* **1963,** *2*, 405-409.
12. Mok, W. S. L.; Antal, M. J.; Varhegyi, G., *Ind. Eng. Chem. Res.* **1992,** *31*, 94-100.
13. Suganuma, S.; Nakajima, K.; Kitano, M.; Yamaguchi, D.; Kato, H.; Hayashi, S.; Hara, M., *J. Am. Chem. Soc.* **2008**.

14. Onda, A.; Ochi, T.; Yanagisawa, K., *Green Chemistry* **2008,** *10*, 1033-1037.

15. Sasaki, M.; Adschiri, T.; Arai, K., *AlChE J.* **2004,** *50*, 192-202.

16. Zhang, Y.; Lynd, L., *Biotechnol. Bioeng.* **2004,** *88*, 797-824.

17. Fukuoka, A.; Dhepe, P. L., *Angew Chem Int Ed* **2006,** *45*, 5161-5163.

18. Dhepe, P. L.; Fukuoka, A., *Catal Surv Asia* **2007,** *11*, 186-191.

19. Fukuoka, A.; Dhepe, P. L., *Chem Rec* **2009,** *9*, 224-235.

20. Luo, C.; Wang, S.; Liu, H., *Angew. Chem. Int. Ed.* **2007,** *46*, 7636-7639.

21. Ji, N.; Zhang, T.; Zheng, M.; Wang, A.; Wang, H.; Wang, X.; Chen, J., *Angew. Chem. Int. Ed.* **2008,** *47*, 8510-8513.

22. Ji, N.; Zhang, T.; Zheng, M.; Wang, A.; Wang, H.; Wang, X.; Shu, Y.; Stottlemyer, A. L.; Chen, J. G., *Catal. Today* **2009,** *147*, 77-85.

23. Zheng, M. Y.; Wang, A. Q.; Ji, N.; Pang, J. F.; Wang, X. D.; Zhang, T., *ChemSusChem* **2010,** *3*, 63-6.

24. Huh, S.; Wiench, J. W.; Yoo, J.-C.; Pruski, M.; Lin, V. S. Y., *Chem. Mater.* **2003,** *15*, 4247-4256.

SUPPORTING INFORMATION

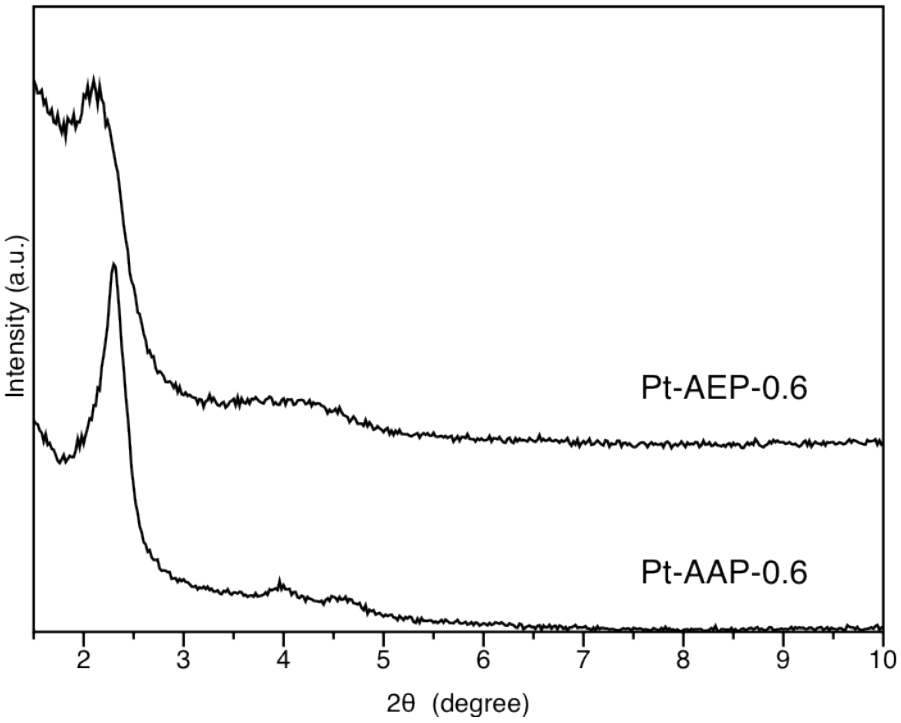

Figure 3-S1. Powder XRD patterns of Pt-AAP-0.6 and Pt-AEP-0.6 materials.

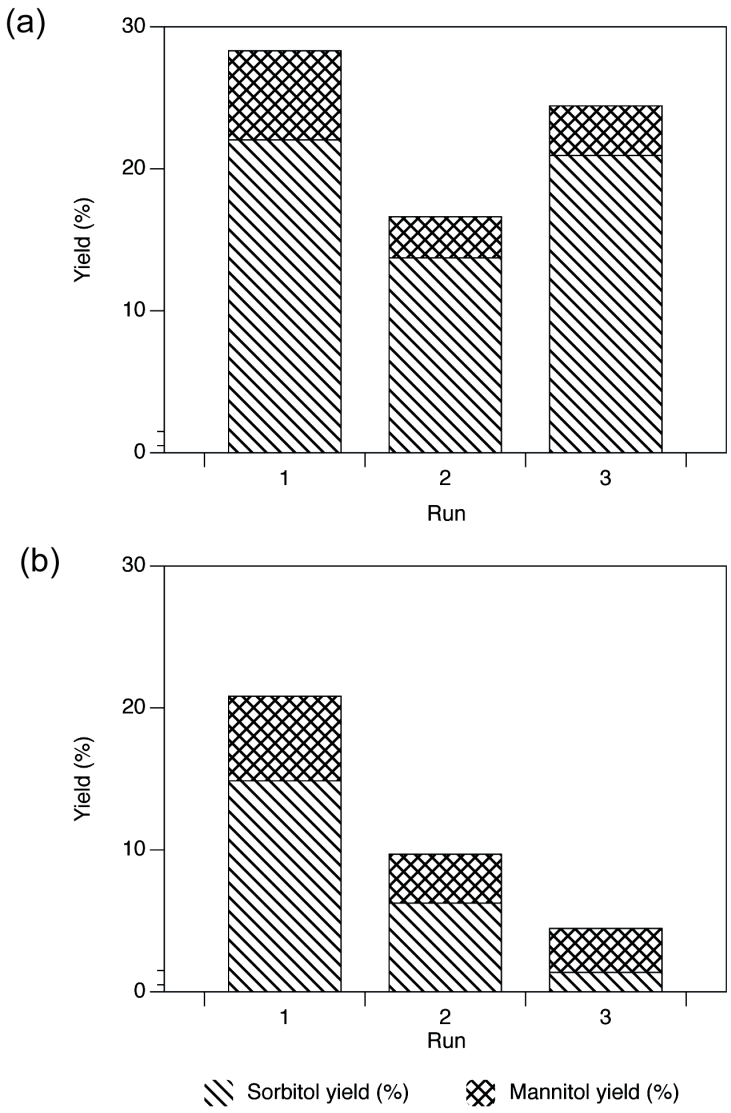

Figure 3-S2. The recyclability test of cellulose conversion catalyzed by Pt-AAP-0.6 material (a) and Pt-AEP-0.6 material (b) in three successive runs.

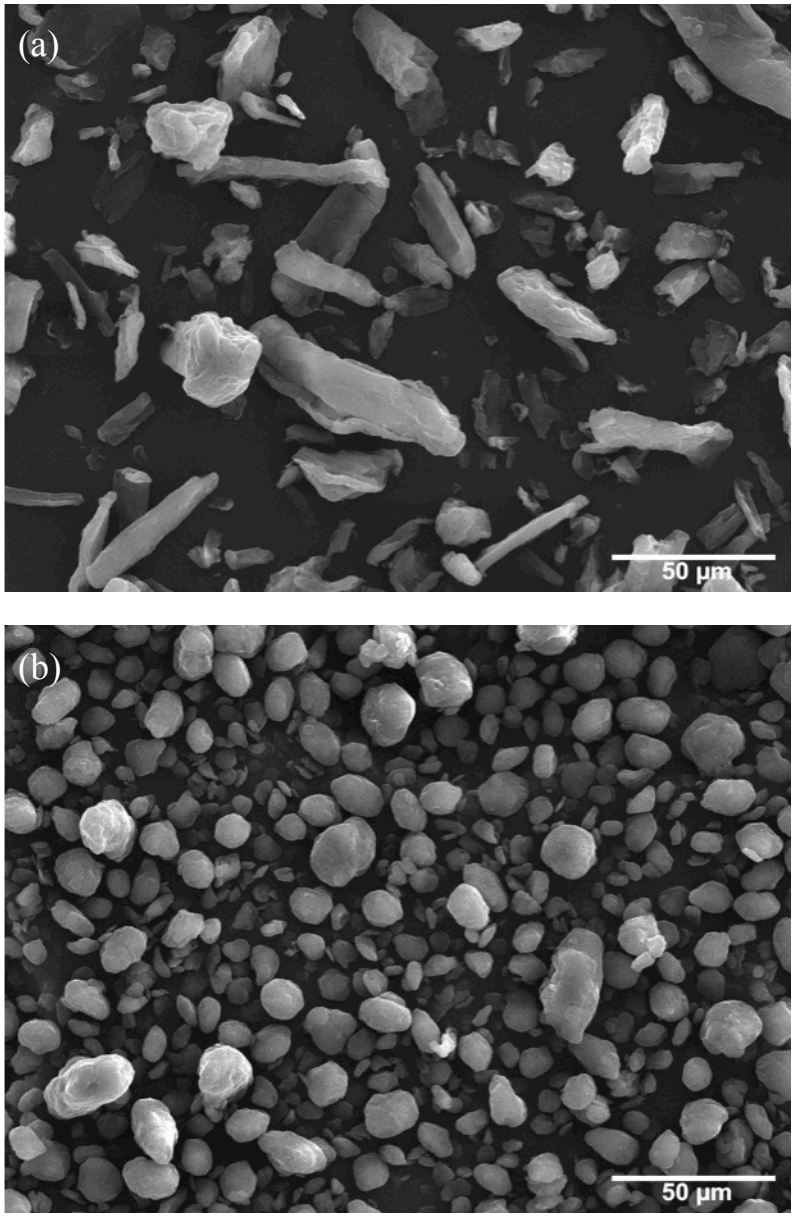

Figure 3-S3. SEM images of cellulose purchased from Aldrich (a) and cellulose ball-milled by ZrO_2 (b). Scale bar = 50 µm.

CHAPTER 4. ORGANIC FUNCTIONALIZED MESOPOROUS SILICA NANOPARTICLES WITH LARGE PORE DIAMETERS AS EFFICIENT HETEROGENEOUS CATALYSTS

A manuscript in preparation and to be submitted to *Chemistry of Materials*

Wei Huang, Chih-Hsiang Tsai, Takeshi Kobayashi, Marek Pruski, Hung-Ting Chen, Brain G. Trewyn, and Victor S.-Y. Lin

Abstract

A series of organic-functionalized large-pore mesoporous silica nanoparticles (LPMSNs) were synthesized *via* the co-condensation method using a Pluronic 104 triblock copolymer as the pore forming surfactant in acidic condition. We systematically investigated synthetic parameters, such as pre-hydrolysis time of tetraethyl orthosilicate and aging temperature, to obtain the rice-shaped individual functionalized LPMSNs with large pore diameters ranging from 5 nm to 10 nm. We discovered that the pre-hydrolysis time was crucial to control particle shape and morphology. Whereas the temperature of hydrothermal process did not influence morphology but affected the chemical accessibility of surface functional groups. The thiol-functionalized LPMSN was oxidized by hydrogen peroxide to convert thiols into sulfonic acids. The catalytic activity of the resulting acid-functionalized LPMSN was examined and it demonstrated higher esterification activity than acid-functionalized SBA-15. This result demonstrated the importance in the size control of mesoporous silica supports in terms of the catalytic reactivity.

Introduction

Since the discovery of M41S family,[1, 2] mesoporous silica materials have attracted extensive interest due to their important structural properties such as large surface area, tunable pore diameter, and feasible surface modification. It was soon after the discovery of mesoporous silicas that the interest in this field has focused on pore expansion and morphology control, which are two extremely important physical parameters for industrial applications.[3-10] Many research groups, including our own, have successfully controlled particle size and morphology of MCM-41 type materials to produce mono-dispersed mesoporous silica nanoparticles (MSNs) with pore diameter in the range of 2 ~3 nm and applied as a carrier in control-release drug delivery[11-16] and as supports in heterogeneous catalysis.[17-21] To further expand the application area, much effort has been devoted to enlarging the pore size of this material.[22-24] The two strategies for pore expansion in MCM-41 that are most commonly utilized are long alkyl chain surfactants or a hydrophobic organic additive swelling agent used in addition surfactant pore formers. However both these strategies also have several disadvantages. For example, the room for pore size enlargement is small when applying long alkyl chain surfactants such as hexadecyltrimethylammonium salts.[1] Also, surfactants with longer carbon chains (> C_{22}) need to be synthesized from expensive precursors. Adding a swelling agent such as 1,3,5-trimethylbenzene (TMB) significantly expands the mesopore diameter up to 10 nm;[1, 25] however, the long-range pore structural ordering is lost with pores larger than 5 nm.[26] In addition, the particle size and shape are not well-controlled as the pore size increases.

SBA-15 as a notable mesoporous silica material with a much large pore diameter, was discovered by Stucky and co-workers, who reported a synthetic procedure using an

amphiphilic triblock copolymer Pluronic 123, poly(ethyleneoxide)$_{20}$-*block*-poly(propyleneoxide)$_{70}$-*block*-poly(ethyleneoxide)$_{20,}$ as the structure-directing agent in acidic condition.[27] The SBA-15 materials exhibited a 2D hexagonal arrangement of highly ordered cylindrical mesopores with tunable pore size varied from 5 nm to 30 nm. Nevertheless, given that the wheat-like macrostructure was observed in the conventional SBA-15, the morphology control of the SBA-15 type materials has been extensively studied. Many synthetic methods, providing individual isolated particles, were reported including adding inorganic salts (such as KCl,[28] NaCl[29]), using co-solvent (like EtOH[30]), and introducing co-surfactant (for example cationic surfactant together with nonionic surfactant[31]) in the reaction mixture. Despite some success that has been made in the synthesis of diverse shaped SBA-15 material,[32-36] control of SBA-15 particle size with channel length of sub-micrometer is still a challenge. Moreover, most morphology studies were focused on pure silica materials; little attention was paid on functionalized ones. Although one can argued that surface functionalization of these materials could be achieved through a post-grafting technique, loading of surface functional groups obtained by this approach was restricted to the number of available silanols, which were especially limited for calcined samples. Thus, it is of great interest to develop a new method to fabricate mesoporous silica nanoparticles with regular particle size, large pore diameter, and also containing highly loaded surface organic functionality.

Herein, we report a simple synthetic procedure combining a co-condensation method with small particle preparation to provide organic functionalized large-pore mesoporous silica nanoparticles (LPMSNs). These LPMSNs are well-isolated particles of regular, uniform sizes (500~800 nm) by systematically refining two synthetic steps: hydrothermal

temperature and the sequence of reagent addition. Five organic silanes, including 3-mercaptopropyl trimethoxysilane (MPTMS), 3-cyanopropyl trimethoxysilane (CPTMS), 3-aminopropyl trimethoxysilane (APTMS), triethoxysilylbutyraldehyde (ADTES), and 3-cyclopentadienylpropyltriethoxysilane (CPDTES), were specifically used in this study because of their potential as linkers for further conjugation with reactive homogeneous catalysts or biological macromolecules for immobilization.

Experimental Section

Chemicals. All chemicals were used as received without further purification. Tetramethyl orthosilicate (TMOS) and palmitic acid were purchased from Sigma-Aldrich. All organic silanes, including 3-mercaptopropyltrimethoxysilane (MPTMS), 3-aminopropyltrimethoxysiliane (APTMS), 3-cyanopropyltrimethoxysilane (CPTMS), triethoxysilylbutyraldehyde (ADTES), and 3-cyclopentadienylpropyltriethoxysilane (CPDTES), were purchased from Gelest. The Pluronic 104 triblock copolymer, $PEO_{27}PPO_{61}PEO_{27}$, was obtained from BASF.

Synthesis of thiol functionalized large-pore mesoporous silica nanoparticle material with different MPTMS addition procedure: A P104 triblock copolymer (7.0 g) was dissolved in 1.6 M HCl(*aq*) solution (273.4 g) and stirred vigorously at 56 °C for 30 min. To the clear solution, TMOS (10.6 g, 69.9 mmol) was added quickly and pre-hydrolyzed for *x* min, where *x* = 0, 15 or 30, followed by a quick injection of MPTMS (1.6 g, 8.4 mmol, 12 mol% of total TMOS). The reaction mixture was kept at 56 °C for 24 h and transferred to a Teflon-lined high-pressure autoclave for aging hydrothermally at 100 °C. The as-synthesized material was isolated by filtration, washed with copious water and

methanol, and dried under vacuum.

Synthesis of thiol functionalized large-pore mesoporous silica nanoparticle material with varying aging temperatures: The synthetic procedure was similar to the aforementioned method, except that MPTMS was added 15 min after injection of TMOS, and the sample was hydrothermally treated at either 100 or 150 °C.

General synthetic procedure of preparing organic functionalized large-pore mesoporous silica materials: The functionalized mesoporous silica material was synthesized in the optimized procedure as described before by pre-hydrolyzed TMOS for 30 min, followed by the addition of organic silane, and the material was aged at 100 °C for 24 h. The introduced amount of organic silane kept at 12 mol% with respect to the TMOS, for all silanes, except for APTMS, which was used at 5 mol%.

General extraction procedure for surfactant removal: The aforementioned material (1.0 g) was refluxed in ethanol (250 ml) for 24 h for removal of the P104 surfactant. The material was filtered, washed with ethanol, and dried under vacuum to yield surfactant-extracted mesoporous silica sample.

Material Characterization: Powder X-ray diffraction (PXRD) was performed on a 2-Theta type X-ray diffractometer by Rigaku Corporation using Cu-Kα radiation. The nitrogen gas sorption analysis was measured on a Micromeritics ASAP 2020 analyzer. A thermogravimetric analyzer 2950 manufactured by TA Instruments was used for thermogravimetric analysis (TGA) measurement of silica samples. The samples were heated from room temperature to 800 °C at ramping rate of 2 °C/min in air. Scanning electron microscopy (SEM) images were taken on a Quanta 250 FEG Scanning Electron Microscope made by the FEI Company. Transmission electron microscopy (TEM) micrographs were

carried out on a FEI Tecnai G^2 F20 STEM working at 200kV. A acid-base titration was applied to determine the quantity of sulfonic acid groups in the mesoporous silica material according to the reported method.[37] Solid-state ^{13}C-NMR spectra were taken under the following conditions: 14.1 T Varian NMR system with a 3.2 mm probe operated at 599.6 MHz for ^{1}H and 150.8 MHz for ^{13}C, respectively. MAS rate n_R = 20 kHz, n_{RF}^{H} = 80 kHz during short pulse, CP (tangent) and SPINAL64 ^{1}H decoupling, n_{RF}^{C} = 60 KHz, τ_{CP} = 1.5 ms, τ_{RD} = 1.5 s and NS = 20000. The spectra are normalized for constant height for visual clarity. ^{29}Si DPMAS spectra were obtained under the following conditions: 9.4 T Chemagnetics CMX Infinity system with a 5 mm probe operated at 400.0 MHz for ^{1}H and 79.5 MHz for ^{29}Si, respectively. MAS rate n_R = 10 kHz, n_{RF}^{Si} = 50 KHz, n_{RF}^{H} = 40 KHz during short pulse and TPPM decoupling, N_{CPMG} = 10, τ_{CPMG} = 10 ms, τ_{RD} = 300 s and NS = 296. The spectra are normalized for constant height for visual clarity.

Synthesis of sulfonic acid-functionalized large-pore mesoporous silica nanoparticles by oxidation: Mercaptopropyl-functionalized material (300.0 mg) was treated with 30 % H_2O_2(*aq*) solution for 24 h for oxidation under Ar. The material was filtered, washed with water and ethanol, and re-suspended in 30 ml of 1 M H_2SO_4(*aq*) for protonation to yield an acid functionalized silica material.

Kinetic study of esterification reaction catalyzed by sulfonic acid-functionalized mesoporous silica material: A mixture of palmitic acid (245.5 mg), methanol (120 μl), and catalyst (1 mol% of sulfonic acid group with respect to palmitic acid) in 5 ml of heptanes was stirred continuously at 60 °C. A small portion of reaction mixture was withdrawn at desired times, and the conversion of palmitic acid to methyl palmitate was determined by ^{1}H-NMR using the integrated area of methyl protons (s, δ = 3.66) and α-methylene protons (t, δ = 2.28-

2.37).

Results and Discussion

Several studies, include our own, reported that introduction of organic silanes in materials influence not only the structure ordering but also the morphology of the final mesoporous silica materials. To avoid the perturbation of final particle morphology, we have systematically investigated synthetic parameters to find a way that to incorporate organic functionality and also maintain individually isolated particles. The MPTMS was used as the model silane for optimization of functionalized LPMSN synthesis due to its potential precursor as an acid catalyst.

Prehydrolysis of TMOS

First, we studied the influence of TMOS prehydrolysis time in terms of final particle morphology. The TMOS was introduced to a surfactant solution and allowed to pre-hydrolyze for *x* min before injection of the functional silane, MPTMS, where $x = 0$, 15, and 30, respectively. The resulting MP-LPMSN was denoted as MP-LPMSN-*x* for simplification. The SEM micrographs of MP-LPMSNs showed that the resulting material had very different morphology depend on the addition time of MPTMS as depicted in Figure 4-1. As shown in Figure 4-1(a), the unfunctionalized LPMSN synthesized based on the literature procedure exhibited mono-dispersed individual hexagonal-shaped particles. However, introducing TMOS and MPTMS simultaneously to the system altered these individual hexagonal particles to aggregations of irregular elongated curved tubes. If the

TMOS was allowed to be prehydrolyzed for 15 min before addition of MPTMS, the aggregation of primary MP-LPMSN particles diminished, which resulted in poorly separated oval-shaped particle as shown in SEM image of MP-LPMSN-15. Further extention of the addition time of MPTMS to 30 min prevented the fusion of particles. The SEM images of MP-LPMSN-30 in Figure 4-1(d) exhibited individual hexagonal particles similar to unfunctionalized LPMSN. In addition, the prehydrolysis of TMOS for longer time also increased the surface area and narrowed pore size distribution as shown in Table 4-S1. The

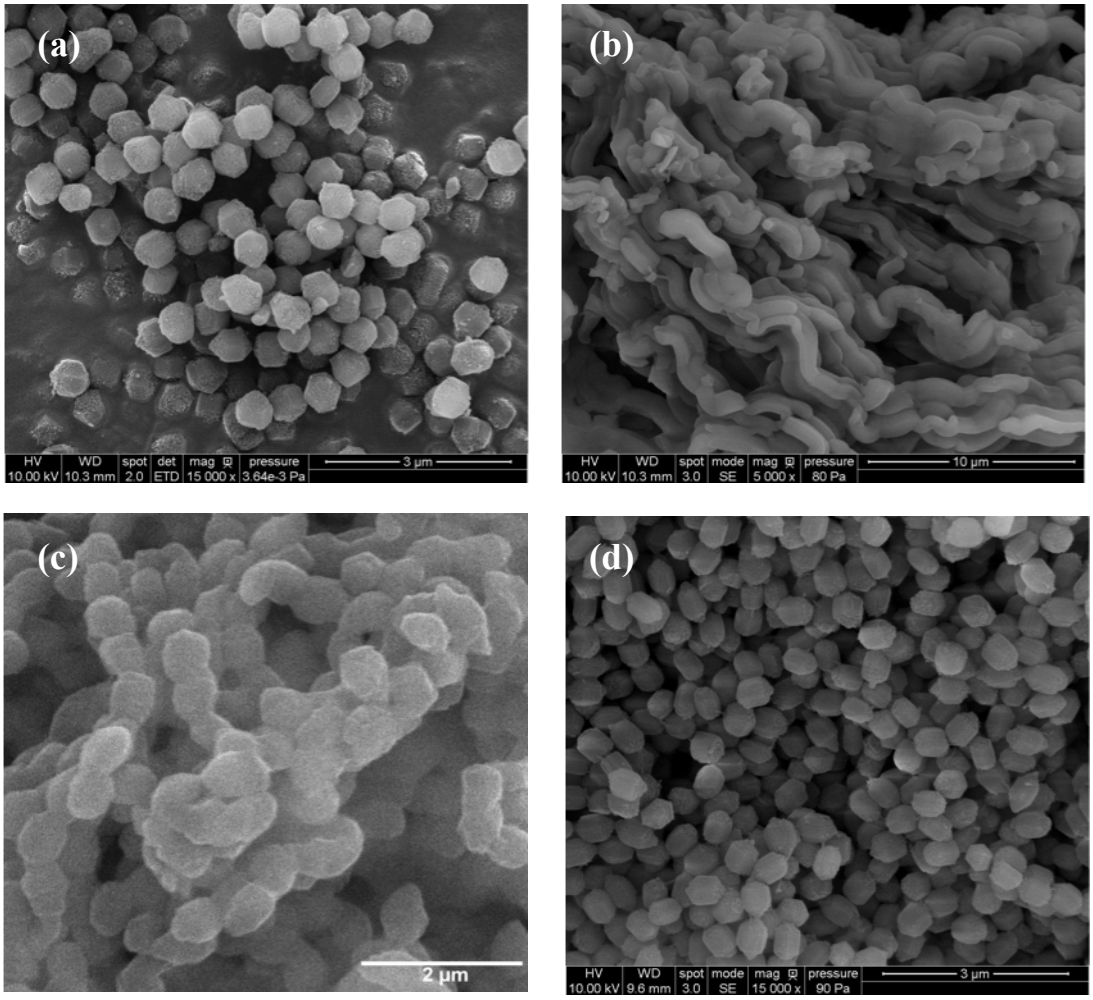

Figure 4-1. SEM images of (a) unfunctionalized LPMSN (scale bar = 3 µm), (b) MP-LPMSN-0 (scale bar = 10 µm), (c) MP-LPMSN-15 (scale bar = 2 µm), and (d) MP-LPMSN-30 (scale bar = 3 µm).

result indicated that that the pre-hydrolysis of TMOS was critical to control particle morphology of the functionalized LPMSN materials. By adding MPTMS at 30 min after injection of TMOS, the uniform well-isolated MP-LPMSNs could be obtained under the reaction conditions.

Aging temperature

To investigate how the aging temperature affected the resulting MP-LPMSN material, the MP-LPMSNs were synthesized based on an aforementioned procedure and hydrothermally aged for 24 h at two different temperatures: 100 and 150 °C. The resulting materials were labeled MP-LPMSN-*y*, where *y* = 100 °C or 150 °C depending on the aging temperature. The textural properties of the two MP-LPMSNs measured by nitrogen sorption analysis were summarized in Table 4-S2. The mean pore diameter of MP-LPMSN-150C exhibited a larger pore diameter of 6.1 nm, calculated by BJH method, than MP-LPMSN-100C with a pore diameter of 4.6 nm. The specific surface area of MP-LPMSN-150C (576 m^2/g), measured by the BET method, was less than that of MP-LPMSN-100C (875 m^2/g). This means that increasing aging temperature enlarged the pore diameter but decreased the surface area of the resulting materials. The ^{29}Si solid-state NMR studies were used as tools to investigate the nature of the incorporation of organic thiol functionality quantitatively and qualitatively in the mesoporous silica framework. As shown in the Figure 4-2, the existence of T sites in the ^{29}Si solid-state DPMAS spectra of MP-LPMSNs demonstrated that the mercaptopropyl group was covalently bonded on the silica surface *via* co-condensation. The amount of surface mercaptopropyl group was estimated by ^{29}Si DPMAS to be 1.2 mmol/g and 1.1 mmol/g for MP-LPMSN-100C and MP-LPMSN-150C, respectively. This result

implies that the hydrothermal aging temperature had no effect on the quantity of incorporated organic functional group. The TGA analyses were also used to further confirm the inclusion of organic thiol group in the MP-LPMSN materials as depicted in Figure 4-3. The weight loss of MP-LPMSNs before 150 °C was assigned to the adsorbed solvent on the silica surface as shown in Figure 4-3 (a) and (b). A weight loss at around 300 °C indicated that the decomposition of mercaptopropyl groups in the two materials, which was close to the temperature found in the mercaptopropyl functionalized SBA-15.

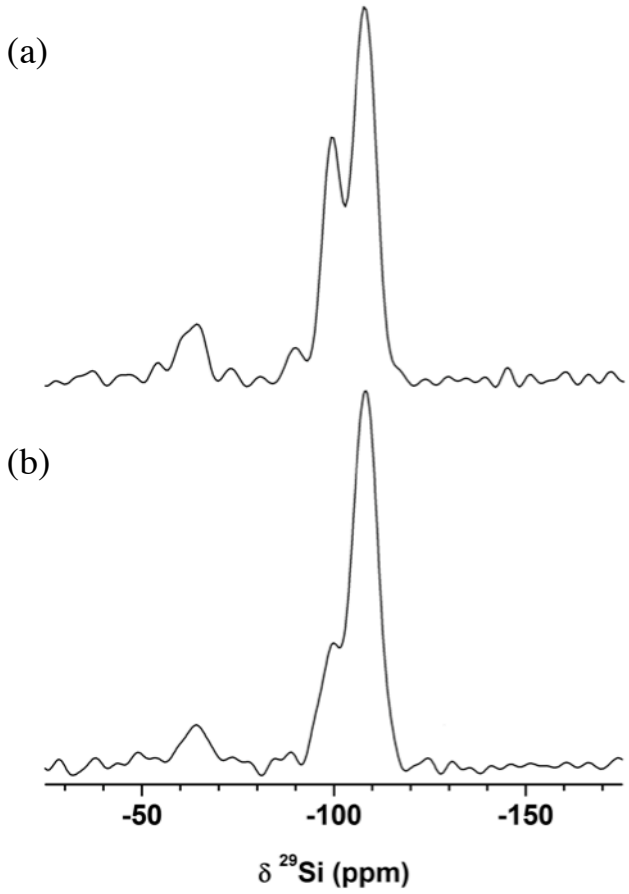

Figure 4-2. ^{29}Si DPMAS spectra of MP-LPMSN-100C (a) and MP-LPMSN-150C (b).

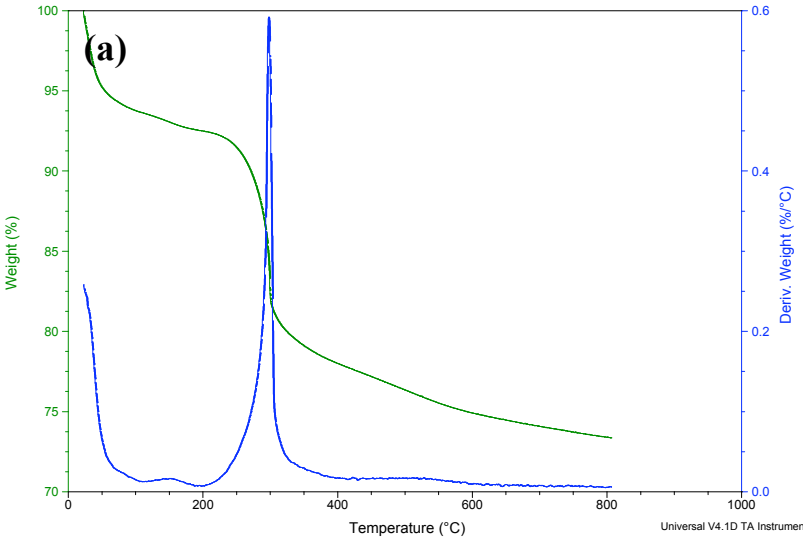

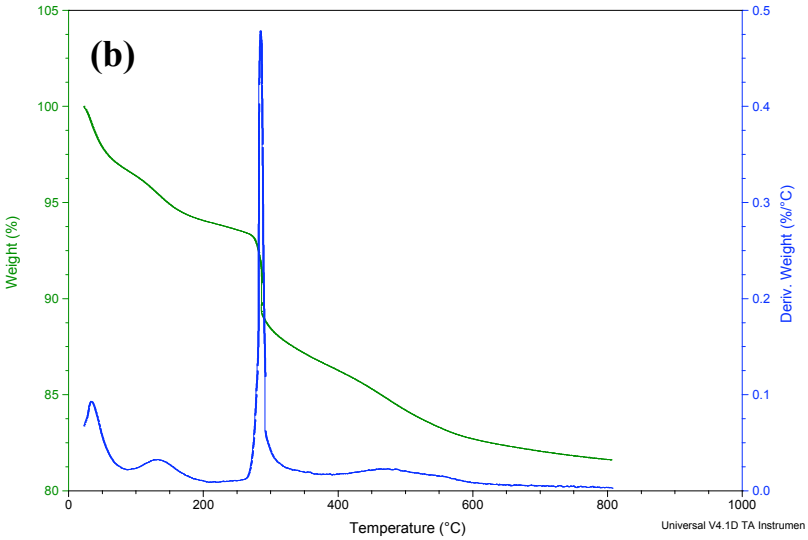

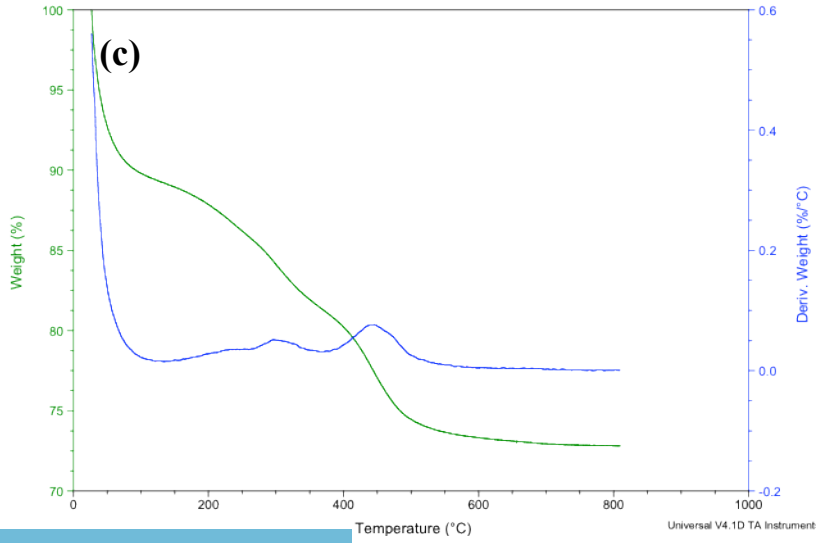

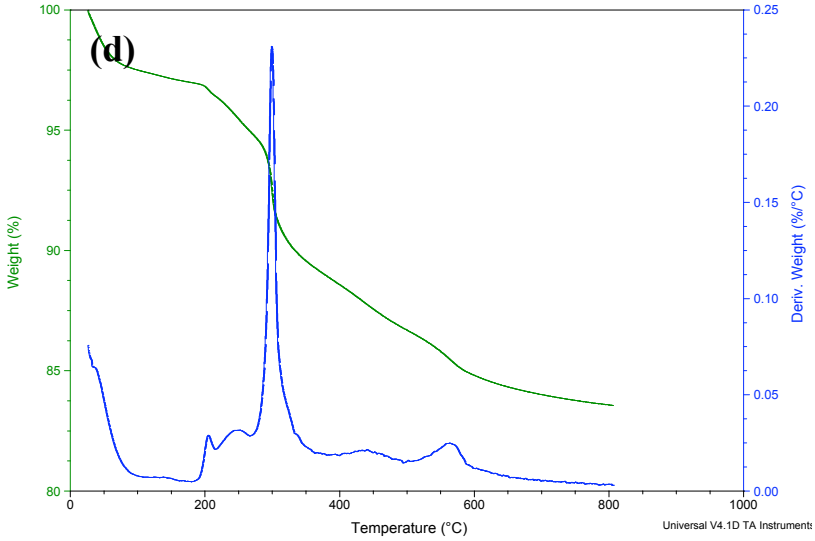

Figure 4-3. TGA analyses of (a) MP-LPMSN-100C, (b) MP-LPMSN-150C, (c) SA-LPMSN-100C, and (d) SA-LPMSN-150C. The mass changes of MP-LPMSN samples were monitored from room temperature to 800 °C at a ramping rate of 2 °C/min in air.

To further study the chemical accessibility of surface functional groups, the MP-LPMSN-100C and MP-LPMSN-150C were subjected to post-synthesis oxidation in 30 *wt*% $H_2O_2(aq)$ solution for 24 h to convert thiols into sulfonic acids, where the resulting materials were labeled as SA-LPMSN-100C and SA-LPMSN-150C, respectively. TGA measurement was performed on the sulfonic acid functionalized LPMSNs to qualitatively examine the conversion of sulfonic acid through oxidation as shown in Figure 4-3 (c) and (d). For SA-LPMSN-100C, a weight loss related to the decomposition of the thiol group was considerably decreased, but a dramatic weight change occurred when the temperature reached around 450 °C indicating the presence of sulfonic acid groups resulted from the oxidation of thiol functionalities. However, there was no observation of weight loss at 450 °C, but at 300 °C, in the SA-LPMSN-150C that suggested that surface thiol groups remained intact after oxidation. The amount of sulfonic acid groups in both SA-LPMSNS were determined by acid-base titration based on a known procedure.[37] Typically, the acid sample

is treated with excess amount of sodium salt, where the chemically accessible acidic protons in the material could be ion-exchanged by sodium cations. The solid material is filtered and the filtrate is titrated with 0.01 M NaOH(*aq*). Surprisingly, the sulfonic acid amount of SA-LPMSN-100C (475 μmol/g), calculated from this method, was found to be five times greater than that of SA-LPMSN-150C (91 μmol/g) as depicted in Table 4-S2. In other words, 41% of the thiol groups on MP-LPMSN-100C, but only 8% on MP-LPMSN-150C, were accessible to the hydrogen peroxide and successfully oxidized. This result could be attributed to the reorganization of silica framework during process of hydrothermal treatment. At higher aging temperature the mesoporous silica structure rearranged in a way that most of the thiol groups were embedded deeply inside the matrix, which became inaccessible and remained intact even in high concentration of the H_2O_2 solution. Aging functionalized LPMSNs at high temperature resulted in a significant reduction in the accessible surface functional groups although it offered larger pore size and similar surface concentration of organic groups.

Synthesis of organic functionalized large-pore mesoporous silica nanoparticles:

A series of organic functionalized LPMSNs were prepared from the reaction mixture containing organosilane/TMOS with molar ratio of 12%, except for APTMS (5%), by using a TMOS prehydrolysis step of 30 min and aging at 100 °C for 24 h. During this investigation, we discovered that the basic APTMS could influence the pH value of the reaction mixture dramatically changing the porous structure of the final LPMSNs. Therefore, the initial amount of APTMS added was reduced from 12 mol% to 5 mol% with respect to TMOS. The as-made sample was extracted in refluxed ethanol to remove surfactant rather than

calcination to preserve the organic functionality at low temperature. The SEM micrographs of all organic functionalized LPMSNs are displayed in Figure 4-4. All of LPMSN materials prepared under optimized synthetic conditions exhibited the well-separated rice-shaped particles with particle size of about 700 × 380 nm. The small-angle XRD patterns of CP-, AP-, and AD-LPMSNs showed three intense diffraction peaks indexed as (100) (110) (200). These are associated with 2-D hexagonal symmetry as depicted in Figure 4-5. The MP- and CPD-MSN display only one (100) peak, indicative of less ordered structure when 3-mercaptopropyl and 3-cyclopentadienylpropyl groups were incorporated into the silica framework.

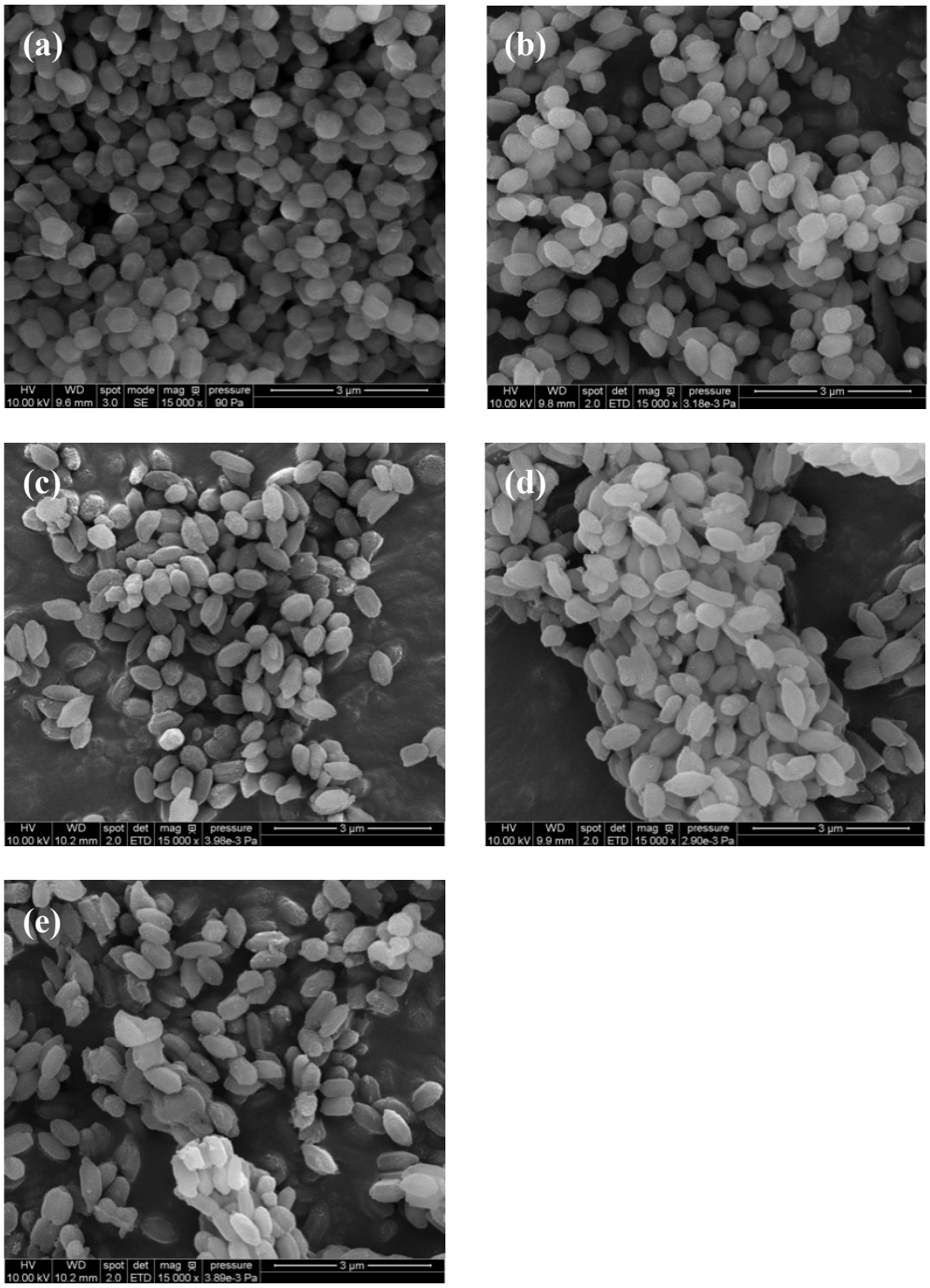

Figure 4-4. SEM images of MP-LPMSN (a), CP-LPMSN (b), AP-LPMSN (c), AD-LPMSN (d), and CPD-LPMSN (e). All scale bar = 3.0 μm.

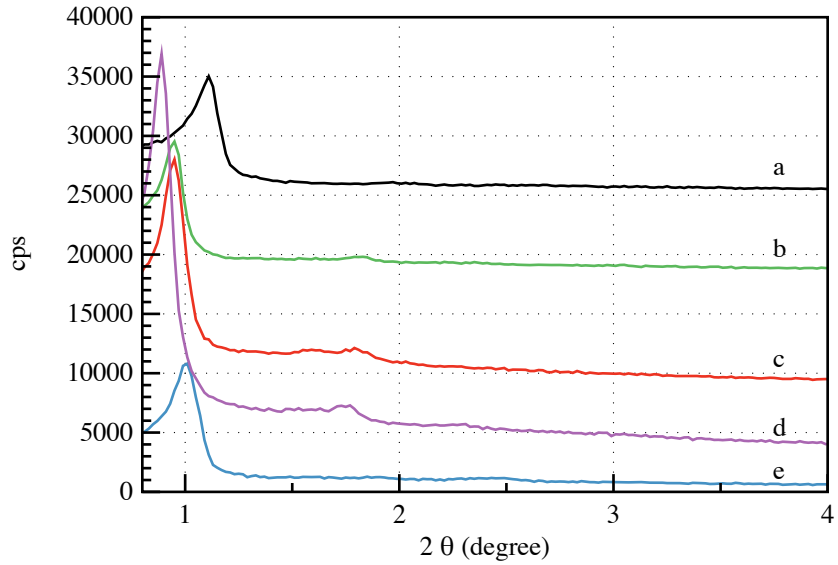

Figure 4-5. Power XRD patterns of MP-LPMSN (a), CP-LPMSN (b), AP-LPMSN (c), AD-LPMSN (d), and CPD-LPMSN (e).

The nitrogen isotherms and pore size distribution of organic functionalized LPMSNs obtained by nitrogen sorption analysis were presented in Figure 4-S1. The type IV isotherms with H_1-type hysteresis were observed in all functionalized LPMSN materials, indicative of hexagonally ordered, cylindrical-channeled mesoporous material. That was confirmed by powder XRD patterns mentioned in Figure 4-5. The LPMSNs showed a very sharp pore size distribution with pore diameters ranging from 5.3 nm to 7.4 nm depending on the types of organic functionality.

Carbon-13 solid-state CP-MAS NMR was employed to demonstrate the presence of organic functionalities in the mesopores and confirm the integrity of the structures as depicted in Figure 4-6. Each resonance peak was assigned based on the observed chemical shifts. The additional peak observed at around 60 ppm most likely represents ethanol adsorbed on the surface during the extraction. The peaks associated with surfactant P104, shown at 18, 70, and 76 ppm, were also detected in the ^{13}C CPMAS NMR spectra of all functionalized LPMSNs, indicating some surfactant remained in the mesopores after ethanol

extraction. As the case of SBA-15, it was reported that ethanol extraction did not completely remove surfactant, leaving about 6 wt% of total sample inside the mesopores.[38] The functional LPMSN materials washed with additional hydrochloric acid in the ethanol or the extended time did not improve the extraction efficiency. Even so, the remained surfactant in the mesopores had little influence on the catalytic activity described here. The amount of organic functionality in the pororus materials was estimated by ^{29}Si solid-state DPMAS spectra, giving similar loadings on the silica surface (1.0 ~1.3 mmol/g) except for the AP group (0.7 mmol/g). Elemental analysis was also performed on MP-, CP-, and AP-LPMSN samples to confirm the loading of functional groups. The CPD- and AD-LPMSNs did not take into account since these two samples contain only C, H, and O atoms, which gave unreliable data due to adsorbed solvents or remained surfactants. The quantities of functional groups in the MP-, CP-, and AP-LPMSNs determined by elemental analysis agreed very well with number obtained by solid-state NMR studies as shown in Table 4-3.

Table 4-3. Structural properties of organic functionalized LPMSNs.

Material	d_{100} (nm)[a]	S_{BET} (m^2/g)[b]	V_p (cm^3/g)[b]	W_{BJH} (nm)[b]	Amount of organic groups (mmol/g)[c]
MP-LPMSN	8.0	782	0.69	5.3	1.2 (1.4)
CP-LPMSN	9.3	855	0.90	6.5	1.3 (1.1)
AP-LPMSN	9.3	654	0.86	7.4	0.7 (0.6)
AD-LPMSN	9.9	864	0.93	6.8	1.0 (-)
CPD-LPMSN	8.7	898	0.74	5.3	1.0 (-)

[a.] The d_{100} number represented d-spacing calculated from the PXRD (100) peak. [b.] Specific surface area (S_{BET}), pore volume (V_p), and mean pore diameter (W_{BJH}) were obtained from nitrogen sorption analysis. The specific surface area was measured by BET method. The mean pore diameter was

masured by BJH method using adsorption data branch. [c.] The organic loading was estimated from ^{29}Si solid-state NMR spectra. The number in the parenthesis was calculated from the elemental analysis.

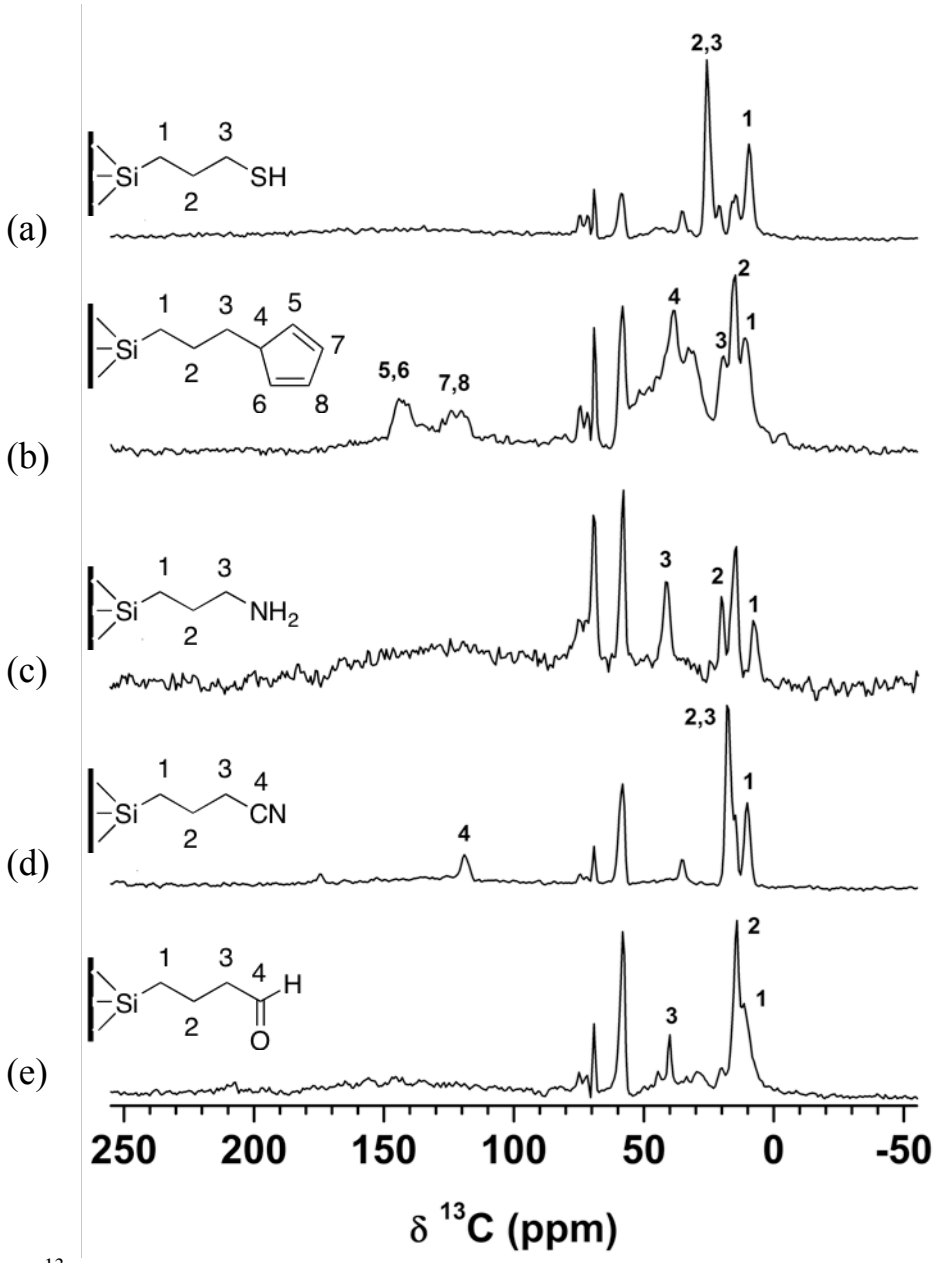

Figure 4-6. ^{13}C solid-state CPMAS NMR spectra of MP-LPMSN (a), CPD-LPMSN (b), AP-LPMSN (c), CP-LPMSN (d), and AD-LPMSN (e).

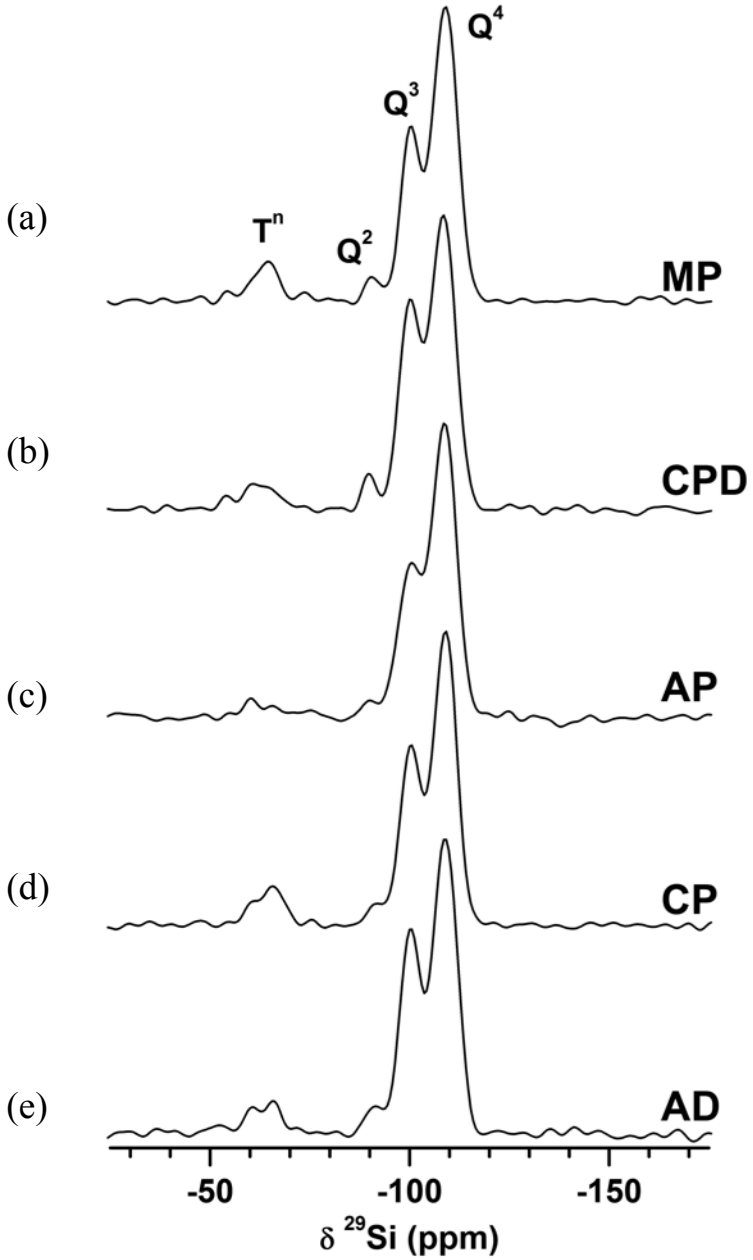

Figure 4-7. ^{29}Si DPMAS spectra of MP-LPMSN (a), CPD-LPMSN (b), AP-LPMSN (c), CP-LPSMN (d), and AD-LPMSN (e).

Kinetics study of esterification catalyzed by sulfonic acid functionalized mesoporous silica.

To evaluate how the particle size of mesoporous silica supports affect the catalytic activity, the esterification of palmitic acid and methanol was conducted using the aforementioned SA-LPMSN-100C as the catalyst and compared the reaction result with one catalyzed by sulfonic acid functionalized SBA-15 (SA-SBA15).[38] The SA-SBA-15 material, synthesized according to literature procedures, was composed of a similar mesoporous structure, i.e. 2-D hexagonal channels, and slightly larger pore diameter of 5.6; however, it was determined that these two materials had very different particle sizes and morphology. The SEM image of SA-LPMSN-100C displayed individual hexagonal-shaped particles with a particle size similar as its precursor, MP-LPMSN, which was around 600 nm × 400 nm as shown in Figure 4-8. On the other hand, SA-SBA15 exhibited elongated tubular aggregates from primary particles. The length of the mesopores in SA-SBA15 was longer than 1 μm with some U-shaped channels. TEM images of two acid functionalized mesoporous silicas unveiled the fine structure of channels with an average depth of 600 nm for the SA-LPMSN-100C and several micrometers long for the SA-SBA15. The difference in length in the mesopore channels will impact on the mass transport of substrates in and out of channels resulting in dissimilar reaction kinetics. In other words, the reactants, palmitic acid and methanol, have to travel longer distances before reaching the catalytic sites located inside the channels, and the product would also need more time to diffuse from the pores when SA-SBA15 was used as catalyst rather than SA-LPMSN-100C. Indeed, as shown in Figure 4-9, the kinetic study showed that the esterification reaction of palmitic acid and methanol catalyzed by SA-LPMSN-100C was much faster (97% conversion in 20 h) than SA-SBA15.

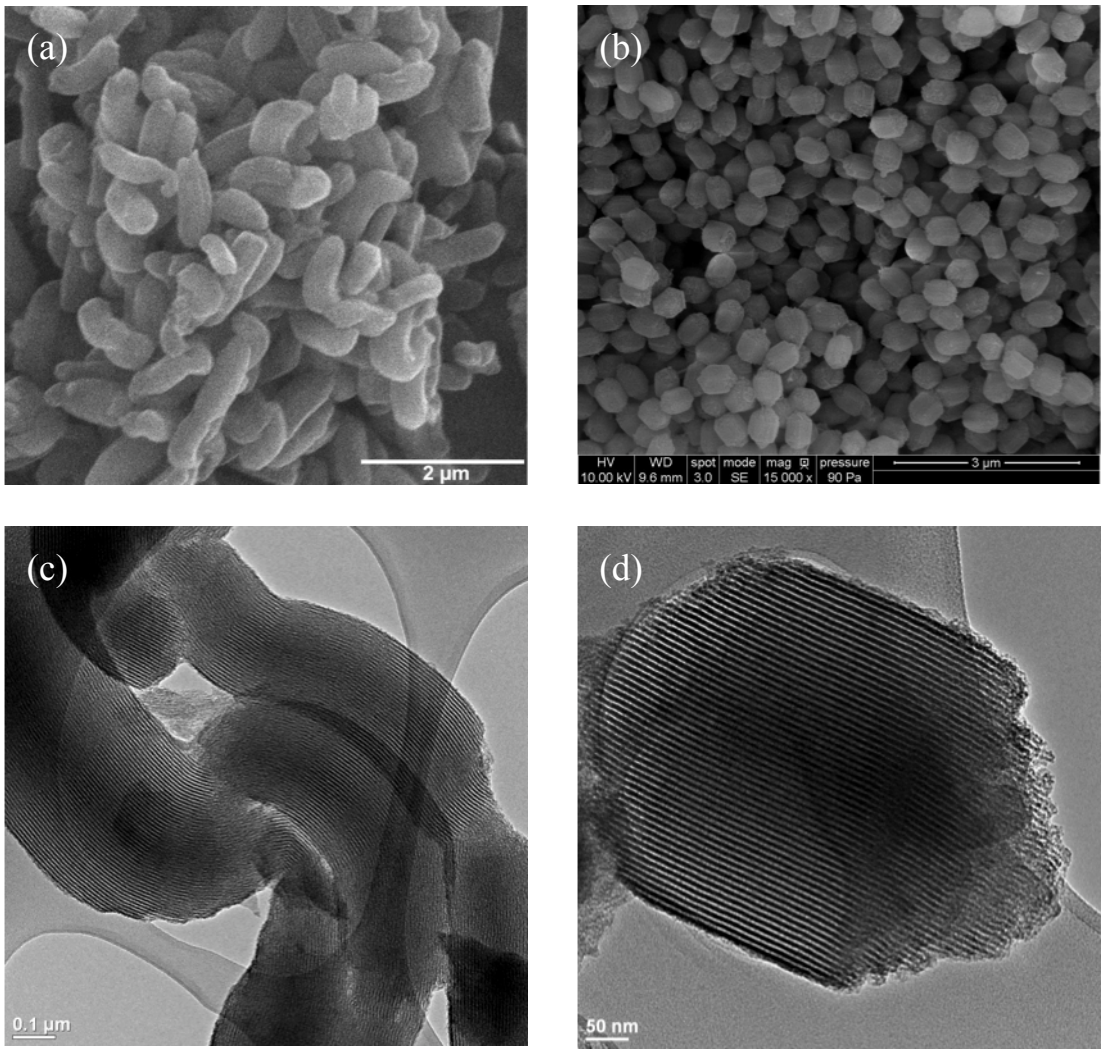

Figure 4-8. SEM images of SA-SBA-15 (a) and SA-LPMSN-100C (b). Scale bar = 2 µm and 3 µm, respectively. TEM images of SA-SBA15 (c) and SA-LPMSN-100C (d). Scale bar = 100 nm and 50 nm, respectively.

While SA-SBA15 was used as a catalyst, the reaction expressed slow kinetics, which only 89% of palmitic acid was converted to methyl palmitate at 30 h, even when the reaction was extended to 2 days, the conversion only increased by 0.5%. Such a difference in reaction rate could be attributed to different depths and curvatures of the mesochannels. The short path of pore channels as in the SA-LPMSN-100C offered less diffusion barriers, which results in faster kinetics of reaction and higher reactivity. This kinetic study demonstrated the merits of using these isolated LPMSNs as catalytic supports.

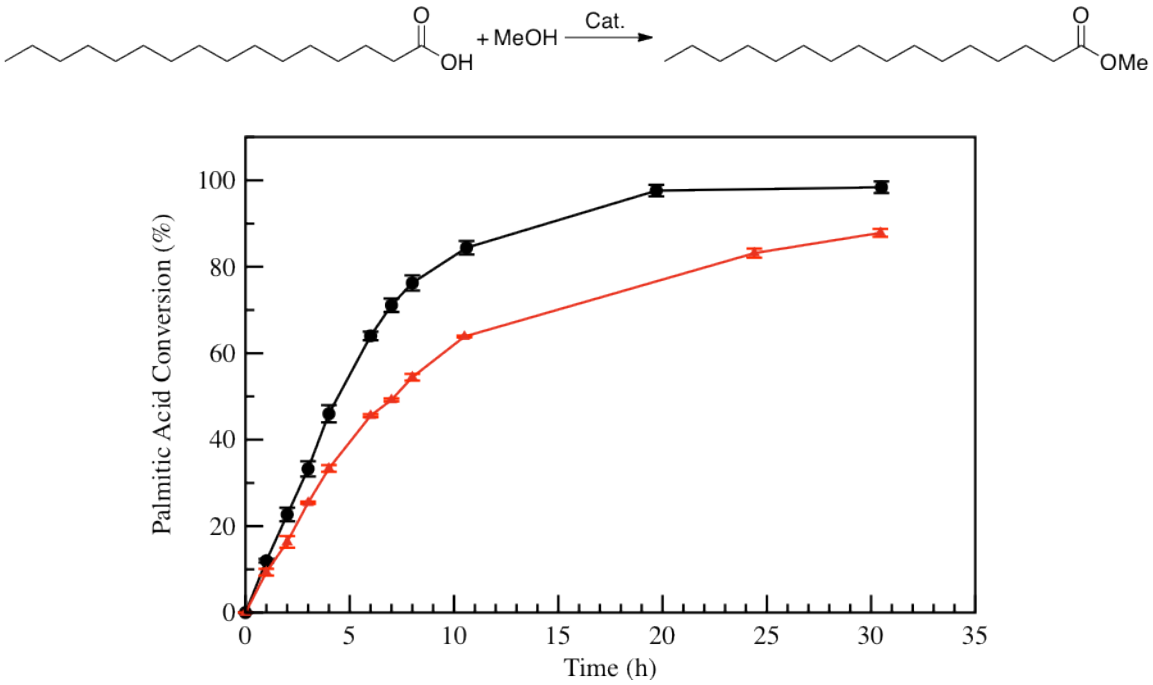

Figure 4-9. Kinetic studies of the esterification reaction catalyzed by SA-LPMSN-100C (black) and SA-SBA15 (red).

Conclusions

In summary, a synthetic procedure, integrating the synthesis of large-pore mesoporous silica with a co-condensation method, was developed to yield a series of organic functionalized LPMSNs with mono-dispersed particle size, large pore diameter, and chemically accessible surface functional groups. The control of particle size in mesoporous supports has also been demonstrated to be beneficial to catalytic reactivity. We envision that these regular sized well-separated organic functionalized LPMSNs could serve by its own as a heterogeneous single-site organic catalyst or a superior material support for immobilization of bulky reactive organometallic catalysts.

References:

1. Kresge, C. T.; Leonowicz, M. E.; Roth, W. J.; Vartuli, J. C.; Beck, J. S., *Nature* **1992,** *359* (6397), 710-712.
2. Beck, J. S.; Vartuli, J. C.; Roth, W. J.; Leonowicz, M. E.; Kresge, C. T.; Schmitt, K. D.; Chu, C. T. W.; Olson, D. H.; Sheppard, E. W.; Mccullen, S. B.; Higgins, J. B.; Schlenker, J. L., *J. Am. Chem. Soc.* **1992,** *114* (27), 10834-10843.
3. Schacht, S.; Huo, Q.; VoigtMartin, I. G.; Stucky, G. D.; Schuth, F., *Science* **1996,** *273* (5276), 768-771.
4. Huo, Q. S.; Zhao, D. Y.; Feng, J. L.; Weston, K.; Buratto, S. K.; Stucky, G. D.; Schacht, S.; Schuth, F., *Adv. Mater.* **1997,** *9* (12), 974-978.
5. Shio, S.; Kimura, A.; Yamaguchi, M.; Yoshida, K.; Kuroda, K., *Chem. Commun.* **1998,** (22), 2461-2462.
6. Tanev, P. T.; Liang, Y.; Pinnavaia, T. J., *J. Am. Chem. Soc.* **1997,** *119* (37), 8616-8624.
7. Bruinsma, P. J.; Kim, A. Y.; Liu, J.; Baskaran, S., *Chem. Mater.* **1997,** *9* (11), 2507-2512.
8. Yang, S. M.; Yang, H.; Coombs, N.; Sokolov, I.; Kresge, C. T.; Ozin, G. A., *Adv. Mater.* **1999,** *11* (1), 52-55.
9. Trewyn, B. G.; Whitman, C. M.; Lin, V. S. Y., *Nano Lett.* **2004,** *4* (11), 2139-2143.
10. Radu, D. R.; Lai, C. Y.; Wiench, J. W.; Pruski, M.; Lin, V. S. Y., *J. Am. Chem. Soc.* **2004,** *126* (6), 1640-1641.
11. Lai, C. Y.; Trewyn, B. G.; Jeftinija, D. M.; Jeftinija, K.; Xu, S.; Jeftinija, S.; Lin, V. S. Y., *J. Am. Chem. Soc.* **2003,** *125* (15), 4451-4459.
12. Lu, J.; Choi, E.; Tamanoi, F.; Zink, J. I., *Small* **2008,** *4* (4), 421-426.

13. Zhao, Y.; Trewyn, B. G.; Slowing, I. I.; Lin, V. S. Y., *J. Am. Chem. Soc.* **2009,** *131* (24), 8398-8400.

14. Patel, K.; Angelos, S.; Dichtel, W. R.; Coskun, A.; Yang, Y. W.; Zink, J. I.; Stoddart, J. F., *J. Am. Chem. Soc.* **2008,** *130* (8), 2382-2383.

15. Liu, R.; Zhang, Y.; Zhao, X.; Agarwal, A.; Mueller, L. J.; Feng, P. Y., *J. Am. Chem. Soc.* **2010,** *132* (5), 1500-+1501.

16. Patil, Y. B.; Swaminathan, S. K.; Sadhukha, T.; Ma, L. A.; Panyam, J., *Biomaterials* **2010,** *31* (2), 358-365.

17. Chen, H. T.; Huh, S.; Wiench, J. W.; Pruski, M.; Lin, V. S. Y., *J. Am. Chem. Soc.* **2005,** *127* (38), 13305-13311.

18. Huh, S.; Chen, H. T.; Wiench, J. W.; Pruski, M.; Lin, V. S. Y., *Angew Chem Int Edit* **2005,** *44* (12), 1826-1830.

19. Mihalcik, D. J.; Lin, W. B., *Angew Chem Int Edit* **2008,** *47* (33), 6229-6232.

20. Demel, J.; Cejka, J.; Stepnicka, P., *J Mol Catal a-Chem* **2010,** *329* (1-2), 13-20.

21. Melero, J. A.; van Grieken, R.; Morales, G., *Chem. Rev.* **2006,** *106* (9), 3790-3812.

22. Corma, A.; Kan, Q. B.; Navarro, M. T.; PerezPariente, J.; Rey, F., *Chem. Mater.* **1997,** *9* (10), 2123-2126.

23. Sayari, A.; Liu, P.; Kruk, M.; Jaroniec, M., *Chem. Mater.* **1997,** *9* (11), 2499-2506.

24. Slowing, I. I.; Trewyn, B. G.; Lin, V. S. Y., *J. Am. Chem. Soc.* **2007,** *129* (28), 8845-8849.

25. Blin, J. L.; Su, B. L., *Langmuir* **2002,** *18* (13), 5303-5308.

26. Huo, Q. S.; Margolese, D. I.; Stucky, G. D., *Chem. Mater.* **1996,** *8* (5), 1147-1160.

27. Zhao, D.; Feng, J.; Huo, Q.; Melosh, N.; Fredrickson, G. H.; Chmelka, B. F.; Stucky, G. D., *Science* **1998,** *279* (5350), 548-52.

28. Yu, C. Z.; Fan, J.; Tian, B. Z.; Zhao, D. Y.; Stucky, G. D., *Adv. Mater.* **2002,** *14* (23), 1742-1745.

29. Linton, P.; Wennerstrom, H.; Alfredsson, V., *PCCP* **2010,** *12* (15), 3852-3858.

30. Cauda, V.; Onida, B.; Platschek, B.; Muhlstein, L.; Bein, T., *J. Mater. Chem.* **2008,** *18* (48), 5888-5899.

31. Zhao, D. Y.; Sun, J. Y.; Li, Q. Z.; Stucky, G. D., *Chem. Mater.* **2000,** *12* (2), 275-279.

32. Liu, Y. M.; Cao, Y.; Yi, N.; Feng, W. L.; Dai, W. L.; Yan, S. R.; He, H. Y.; Fan, K. N., *J. Catal.* **2004,** *224* (2), 417-428.

33. Sayari, A.; Yang, Y., *Chem. Mater.* **2005,** *17* (24), 6108-6113.

34. De Witte, K.; Meynen, V.; Mertens, M.; Lebedev, O. I.; Van Tendeloo, G.; Sepulveda-Escribano, A.; Rodriguez-Reinoso, F.; Vansant, E. F.; Cool, P., *Appl Catal B-Environ* **2008,** *84* (1-2), 125-132.

35. Meynen, V.; Cool, P.; Vansant, E. F., *Microporous Mesoporous Mater.* **2009,** *125* (3), 170-223.

36. Basaldella, E. I.; Legnoverde, M. S., *J. Sol-Gel Sci. Technol.* **2010,** *56* (2), 191-196.

37. Badley, R. D.; Ford, W. T., *J. Org. Chem.* **1989,** *54* (23), 5437-5443.

38. Margolese, D.; Melero, J. A.; Christiansen, S. C.; Chmelka, B. F.; Stucky, G. D., *Chem. Mater.* **2000,** *12* (8), 2448-2459.

SUPPORTING INFORMATION

Table 4-S1. Tetural properties of MP-LPMSNs prepared in different prehydrolysis time.

Material[a]	d_{100} (nm)	Surface area (m^2/g)[b]	Pore volume (cm^3/g)	Mean pore diameter (nm)[c]
MP-LPMSN-0	7.8	694	0.55	2~5.2
MP-LPMSN-15	8.2	857	0.79	4.6
Mp-LPMSN-30	8.0	782	0.69	5.3

[a.] The *x* in the notation of MP-LPMSN-*x* indicated the prehydrosis time in min of TMOS before addition of MPTMS. [b.] Specific surface area was calculated from BET method. [c.] Mean pore diameter was calculated based on BJH method.

Table 4-S2. Physical and chemical properties of MP-LPMSN prepared at different aging temperature.

Material[a]	Surface area (m^2/g)[b]	Mean Pore diameter (nm)[c]	-SH loading (mmol/g)[d]	H+ amount (mmol/g)[e]
MP-LPMSN-100C	875	4.6	1.2	0.475
MP-LPMSN-150C	576	6.1	1.1	0.091

[a.] The *y* in the notation of MP-LPMSN-*y* indicated the temperature of hydrothermal treatment. [b.] Specific surface area was calculated from BET method. [c.] Mean pore diameter was calculated based on BJH method. [d.] Loading of surface thiol group in the MP-LPSMN was estimated from ^{29}Si solid-state NMR spectra. [e.] The acid amount in the sulfonic acid-functionalized LPMSN obtained through oxidation of corresponded MP-LPMSN was measured by acid-base titration using reported method.

Table 4-S3. Structural and chemical properties of SA-LPMSN-100C and SA-SBA15.

Material	Surface area (m^2/g)[a]	Mean Pore diameter (nm)[b]	Pore channel length (μm)	Loading of sulfonic acid (μmol/g)[c]
SA-LPMSN-100C	838	4.8	~0.6	375
SA-SBA15	669	5.6	> 1	733

[a.] Specific surface area was calculated from BET method. [b.] Mean pore diameter was calculated based on BJH method. [c.] The acid amount in the sulfonic acid-functionalized LPMSN obtained through oxidation of corresponded MP-LPMSN was measured by acid-base titration using reported method.

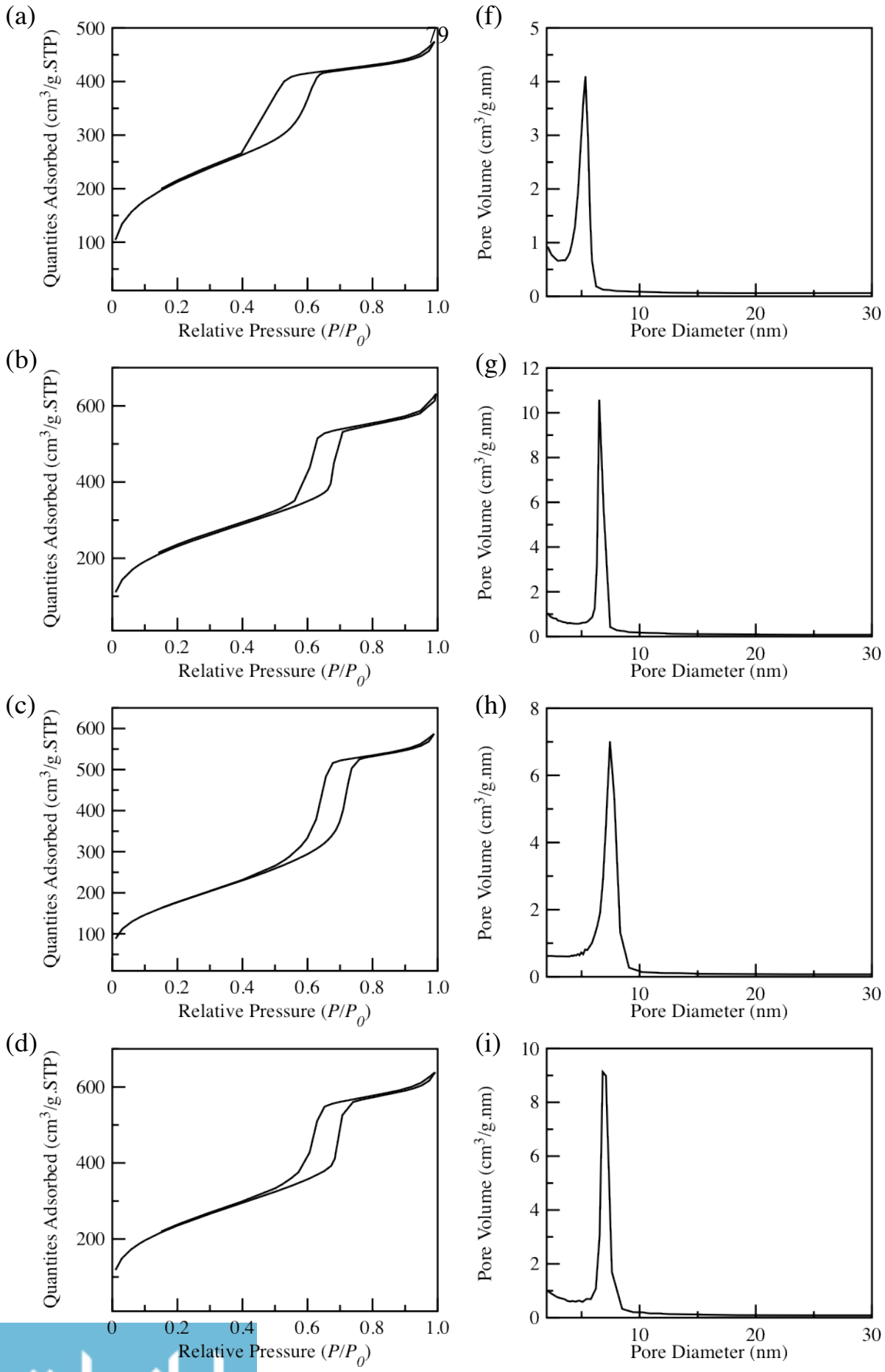

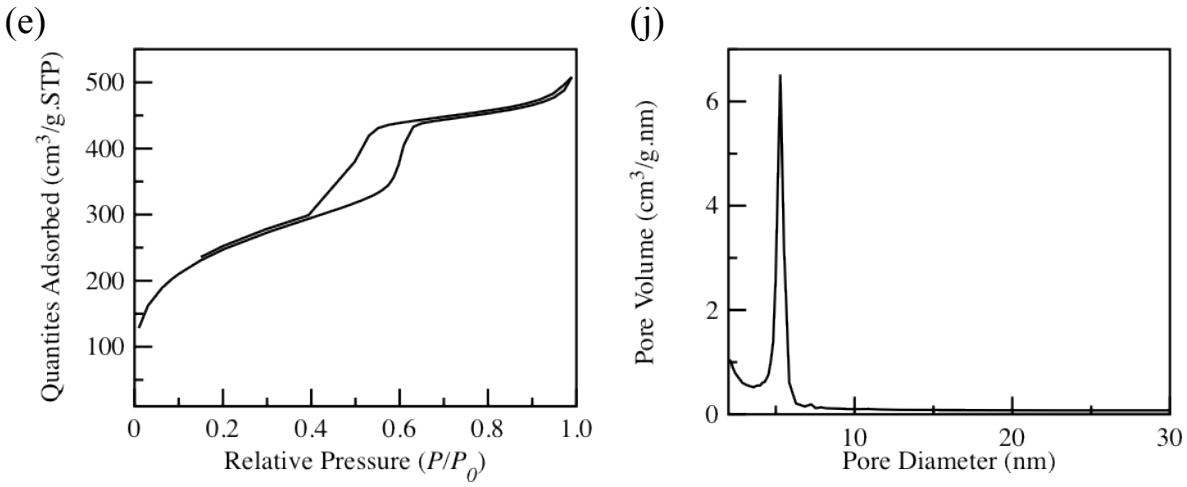

Figure 4-S1. Nitrogen sorption isotherms of MP-LPMSN (a), CP-LPMSN (b), AP-LPMSN (c), AD-LPMSN (d), and CPD-LPMSN (e). BJH pore size distribution of MP-LPMSN (f), CP-LPMSN (g), AP-LPMSN (h), AD-LPMSN(i), and CPD-LPMSN (j).

CHAPTER 5. CONCLUTION

In this dissertation, I have presented my Ph.D. studies regard to syntheses of functionalized mesoporous silica nanoparticles (MSNs) and their versatile applications in the controlled-release drug delivery and catalysis. I also developed a synthetic method to prepare new-typed mesoporous materials from original small-pore MSNs to functionalized large-pore MSNs with well-controlled particle size and morphology. My research accomplishment was detail list below:

1. I have synthesized a hybrid organic/inorganic composite material composed of poly(L-lysine) immobilized mesoporous silica nanoparticles (PLL-MSN). Poly(L-lysine) was coated on the outer surface of amine functionalized MSN via the graft-on approach using the ring-opening polymerization. The thick polymer layer acted as a biodegradable cap, which regulated the release of drugs pre-encapsulated inside the mesochannels during surface polymerization. The poly(L-lysine) cap resisted pepsin digestion in acidic environment similar in the stomach, but degraded readily by trypsin under physiological condition. This unique property of PLL-MSN made this material a potential oral drug delivery vehicle.
2. I also synthesized a series of platinum nanoparticle-immobilized MSNs (Pt NP-MSNs) as heterogeneous catalysts for cellulose degradation. The Pt NP was tethered on the MSN through a physical adsorption with surface amine groups, confined inside the mesopores, followed by reduction to produce Pt-NPs with regular size well-distributed in the entire materials. The Pt NP-MSNs successfully catalyzed the

conversion of cellulose into value-added chemicals, sorbitol and mannitol, and were able to recycle at least three times under optimized reaction conditions.

3. To expand the applications of MSNs, I developed a new method combining the merits of co-condensation method and small particle synthesis to prepare a series of mono-dispersed organofunctionalized MSNs with large pore diameter (LPMSNs). The synthetic conditions were systematically studied and optimized. The resulting materials have larger pore size (5.3 ~ 7.4 nm) than regular MSNs (2 ~ 3 nm) and have well-controlled particle morphology. I also demonstrated that by controlling the particle size these functional LPMSN materials are better catalyst supports than conventional SBA-15s due to the efficient mass transfer in the shorter pore channels.
4. By applying alumina source ($NaAlO_2$) in the co-condensation, I have synthesized a mesoporous aluminum silicate (Al-MS) material under basic conditions. The aluminum was found incorporated in the silica framework with only tetrahedral coordination, evidenced from comprehensive solid-state NMR studies, which increased the thermal stability and acidity of the resulting Al-MS. In addition, the Al-MS showed excellent catalytic reactivity for the Claisen rearrangement of allyl phenyl ether despite the low surface concentration of aluminum.

APPENDIX. MESOPOROUS ALUMINUM SILICATE CATALYST WITH SINGLE-TYPE ACTIVE SITES: CHARACTERIZATION BY SOLID-STATE NMR AND STUDIES OF REACTIVITY FOR CLAISEN REARRANGEMENT REACTIONS

A paper published in *J. Phys. Chem. C* 2007, 111, 1480-1486.

Yang Cai, Rajeev Kumar, Wei Huang, Brian G. Trewyn, Jerzy W. Wiench, Marek Pruski, and Victor S.-Y. Lin

Department of Chemistry and U.S. Department Of Energy Ames Laboratory, Iowa State University, Ames, Iowa

Abstract

A mesoporous aluminum silicate (Al-MS) material has been successfully synthesized via a base-catalyzed co-condensation reaction. Solid-state NMR studies showed that the aluminum atoms are tetrahedrally coordinated and are stable up to at least 400 °C. The double resonance ^{27}Al-^{29}Si NMR experiment provided first direct evidence that all Al atoms are surrounded by Si atoms forming Al-O-Si bonds in the framework. The silicon to aluminum atomic ratio at the surface $(Si/Al)_s$ is estimated at around 100, which exceeds the overall Si/Al ratio of 60. Reactivity study of the mesoporous aluminosilicate shows an excellent catalytic reactivity for the Claisen rearrangement of allyl phenyl ether despite the low surface concentration of Al.

Introduction

Recent advancements in the surface functionalization of MCM-type mesoporous silica materials with high surface area (>600 m^2/g) and uniform pore morphology have started a global pursuit in developing new generations of mesoporous catalysts for various industrially important reactions.[1-5] Much effort has been directed toward the isomorphous substitution of silicon atoms with other catalytically active elements, such as Al,[6-10] Mn,[11,12] Ga,[13] B,[14,15] Ti,[16,17] and V.[18-20] In particular, recent reports on the synthesis of aluminum-containing MCM-41 silicas[6,7,21-30] have successfully demonstrated that the incorporation of aluminum atoms into the mesoporous silica framework could increase the acidity of the mixed oxide materials.[3,8,23,31,32] Numerous organic reactions are catalyzed by highly acidic mesoporous materials, such as the Claisen rearrangement. However, the acidity of these mesoporous aluminosilicates varies significantly between materials prepared by different synthesis methods. Many have attributed such variation to the presence of aluminum sites with different coordination environments resulted from the different conditions of synthesis.[6,7,23,25,26,33,34] Furthermore, the ^{27}Al NMR spectra of many Al-MCM-41 materials prepared by hydrothermal and postsynthesis methods exhibit two aluminum peaks, which are assigned to tetrahedrally and octahedrally coordinated Al atoms.[6,7,25,26,29,30,32,35]

Among the current state-of-the-art methods for preparing mesoporousaluminosilicates, the direct co-condensationmethod[27,28] offers the advantages of shorter synthesis time, lower concentrations of surfactant, homogeneous coordination environment, and well-ordered mesoporous structures. However, this method yields Al sites in the bulk silica matrix as well as on the surface of mesopores. Because only the chemically accessible Al sites can be catalytically active, it is important to get information about the

spatial distribution of aluminum to determine the ratio between the bulk and surface Al atoms so that the location and chemical reactivity of these materials can be correlated. To the best of our knowledge, the determination of the spatial distribution of Al atoms in these materials has not been reported in the literature.

To gain understanding of how the spatial distribution of aluminum atoms affects the structure and chemical reactivity of the mesoporous aluminosilicate materials, we synthesized an Al-MS material via a base-catalyzed co-condensation method. The mesoporous structure of this material was thoroughly characterized by powder X-ray diffraction (XRD), N_2 sorption analysis, and transmission electron microscopy (TEM). The solid-state NMR analysis showed that our material has the overall silicon to aluminum atomic ratio of about 60 and is thermally stable even at 400 °C. In the dried state, only the tetrahedrally coordinated Al sites were observed. By using a sensitivity-enhanced ^{27}Al-^{29}Si cross polarization magic angle spinning (CPMAS) NMR technique, we obtained direct evidence of aluminum incorporation into the silica network. Furthermore, we were able to determine that the silicon to aluminum atomic ratio at the surface $(Si/Al)_s$ is around 100 (i.e., that the distribution of aluminum atoms is not homogeneous). These results indicate that there are less chemically accessible Al sites on the surface of this material than is suggested by a bulk measurement of the Si/Al ratio on the whole sample. We believe this is the first report on the quantitative determination of the chemically accessible (i.e., surface) Al sites in the mesoporous aluminosilicate materials. Furthermore, we demonstrated that this Al-MS material is an excellent catalyst for Claisen rearrangement despite the low surface Al loading.

Experimental section

Materials. Tetraethylorthosilicate (TEOS) was purchased from Gelest and used as received. Sodium aluminates ($NaAlO_2$) and *n*-cetyltrimethylammonium bromide (CTAB) were acquired from Strem and Aldrich, respectively. Other reagents were used as received from Fisher Scientific without further purification. Nanopure water prepared from a Barnstead E-pure water purification system was employed throughout. Toluene was dried prior to use by passage through an alumina/copper column under nitrogen.

Synthesis of Al-MS Material. A mixture of CTAB (1.0 g, 2.74×10^{-3} mol), 2 M of NaOH (aq) (3.5 mL, 7.0×10^{-3} mol), nanopure water (480 g, 26.67 mol), and $NaAlO_2$ (0.0577 g, 0.70×10^{-3} mol) was heated at 84 °C for 2 h 20 min. TEOS (22.4×10^{-3} mol, 5 mL) was added dropwise to this clear solution by a syringe pump with a rate of 60 mL/h. The mixture was stirred for 2.5 h at 84 °C. The solid product was isolated via a filtration, was washed with a copious amount of distilled water and methanol, and was dried under vacuum to yield the "as synthesized" Al-MS material. To remove the surfactant CTAB, the as synthesized Al-MS material was refluxed for 24 h in a methanol solution with 0.1 M HCl. The resulting surfactant-removed solid product was filtered, washed with distilled water and methanol, and then was dried under vacuum. The above synthesis was repeated several times and the purified products were thoroughly characterized as described below. Because these products were essentially indistinguishable, the results are reported for a single material denoted as Al-MS.

General Characterization. Powder XRD data were collected on a Scintag XRD 2000 X-ray diffractometer with Cu Kα radiation (λ = 0.154 nm). Low angle diffraction with

a 2θ range of 1.5 to 10° was used to investigate the long-range order of the mesoporous Al-MS material. Nitrogen adsorption-desorption measurement was conducted on a Tristar 3000 Sorptometer at 77 K. The sample was degassed at 120 °C for 6 h before measurements. The surface area and pore volume/pore size distribution were calculated using the Brunauer-Emmett-Teller (BET) and Barrett-Joyner-Halenda (BJH) method, respectively. TEM measurement was performed on a Philips CM-30 microscope operated at 300 kV.

Solid-State NMR. The solid-state NMR experiments were performed on a Varian NMR System 600 spectrometer, equipped with a triple tuned 3.2 mm MAS probe operated at a rate ν_R = 10 kHz. The samples were packed in MAS rotors after exposure to ambient conditions (55% relative humidity) or after heating up to 400 °C for 3 h under a pressure of 10^{-5} Torr and tightly capping in a glove bag under dry nitrogen. The NMR methods used are explained below. The specific experimental parameters are given in the figure captions in which ν_{RF}^{X} denotes the magnitude of radiofrequency field applied to X nuclei, τ_{CP} is the cross polarization time, τ_{RAPT} is total length of the rotor assisted population transfer (RAPT) sequence,[36] τ_{CPMG} is the time interval between π pulses in the Carr-Purcell-Meiboom-Gill (CPMG) sequence, n_{CPMG} is the number of acquired echoes, and *NS* is the total number of scans.

^{27}Al MAS and multiple-quantum (MQ) MAS NMR spectra were acquired using direct polarization (DP). To accurately determine the Al content in Al-MS, we compared the DPMAS spectra of several samples with that of a reference (a rotor filled with 5 wt % of γ-Al_2O_3 diluted in sulfur, which had similar geometry, line width, and intensity) measured under identical conditions. Several studies have shown that some of the aluminum sites in

mesoporous aluminosilicates may become invisible due to considerable quadrupolar broadening.[7,9,29,35] To minimize the number of sites with low symmetry, we performed the experiments on the sample that was hydrated through exposure to ambient humidity. Full hydration using D_2O also was tried. However, it had no further effect on the spectra. The measurements used 4,000 scans, two ν_{RF}^{Al} values (25 and 83 kHz), and a small flip angle $\pi/[4(I + 1/2)] = 15°$.[37] The recycle delay was 50 ms, which exceeded the ^{27}Al longitudinal relaxation time T_1 by a factor of more than 5.

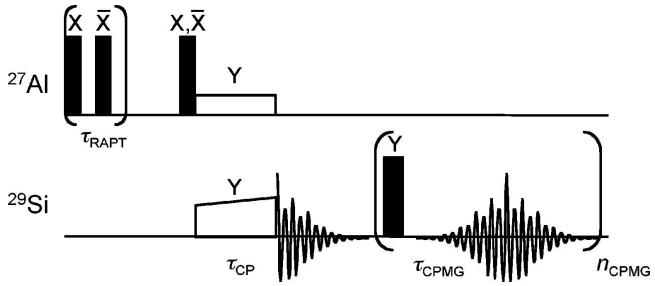

Figure 5-1. Pulse sequence used in RAPT-CPMAS-CPMG experiment.

One-dimensional (1D) ^1H-^{29}Si CPMAS, ^{29}Si DPMAS, and ^{27}Al-^{29}Si CPMAS NMR experiments were performed. All three experiments used a CPMG train of rotor-synchronized π-pulses[38,39] during the detection of silicon magnetization. The CPMG sequence, which refocuses the inhomogeneous line broadening and reduces the homonuclear dipolar broadening in solids, can be used to boost sensitivity in samples with favorable T_2/T_2^* ratio. T_2 denotes here the spin-spin relaxation time due to time-dependent interactions that are nonrefocusable by the π-pulses, and T_2^* corresponds to signal decay following a single-pulse excitation. The CPMG scheme has recently assisted us in acquiring the ^1H-^{29}Si heteronuclear correlation (HETCOR) spectra of MCM-41 silica functionalized with allyl

groups, where a sensitivity gain approaching 1 order of magnitude has been achieved.[40] The ^{27}Al-^{29}Si CPMAS experiment was carried out using the pulse sequence shown in Figure 5-1, which combines cross polarization with RAPT and CPMG detection. In this case, the CPMG train was limited to only 6 echoes because the recycle delay was controlled by fast relaxing ^{27}Al nuclei (T_1 < 10 ms). Still, the implementation of RAPT and CPMG increased the overall sensitivity by a factor of approximately 5. The resulting RAPT-CP-CPMG pulse sequence yielded spectra, which would have been undetectable in our samples under the standard ^{27}Al-^{29}Si CPMAS conditions.

It was equally important to verify that the aluminum sites associated with silicon represent most of the observed ^{27}Al intensity. Therefore, we compared that intensity with the ^{27}Al^{29}Si RAPT-CP MAS spectrum of a known reference, which had similar ^{27}Al and ^{29}Si environments (zeolite 13X with a Si/Al ratio of 2.6). Because of well-known quantitative uncertainties associated with the complex dynamics of spin-locking and CP transfer in the case of quadrupolar nuclei,[41,42] this approach yielded only a rough estimate of the real intensities.

The ^{27}Al and ^{29}Si shifts were referenced to solution $Al(NO_3)_3$ and $SiMe_4$, respectively, at 0 ppm.

Catalytic Test. The catalytic activity of the synthesized material was evaluated by the allyl phenyl ether rearrangement reaction. The reaction was carried out under nitrogen, using 0.978 g of allyl phenyl ether in 9 mL of refluxing toluene with 0.1 g of catalyst. The reaction mixture was sampled with a syringe at different time intervals. The aliquots were analyzed by gas chromatography (HP 5890, FID detector). The reaction intermediates and

products were identified by gas chromatography-mass spectroscopy (GC-MS) and by comparison with the retention times of standards under the same analytical conditions.

Results and discussion

XRD and TEM Results. As shown in Figure 5-2, the XRD pattern of the Al-MS exhibited the characteristic and intense low angle peak at d = 41.3 Å, which can be indexed as the d100 reflection on a hexagonal unit cell. The pattern also displayed a broad secondary feature at about 4.0° (2θ) derived from the combination of d_{110} and d_{200} diffractions. The absence of resolved high-order peaks indicated that any structural order of the material did not extend over a long range, which is probably due to the incorporation of Al into mesoporous framework. TEM image of Al-MS reveals a wormhole-like pore arrangement, which is in agreement with the XRD result as depicted in Figure 5-3.

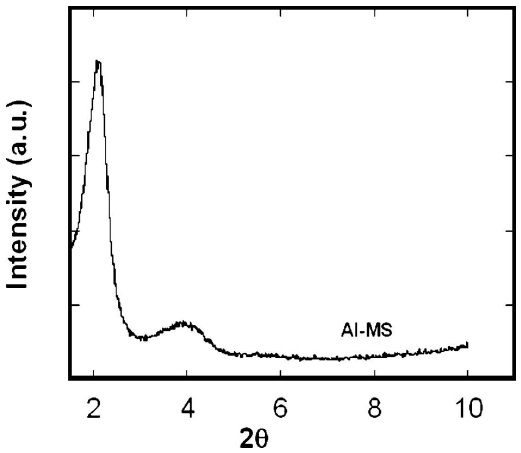

Figure 5-2. Powder XRD pattern of Al-MS.

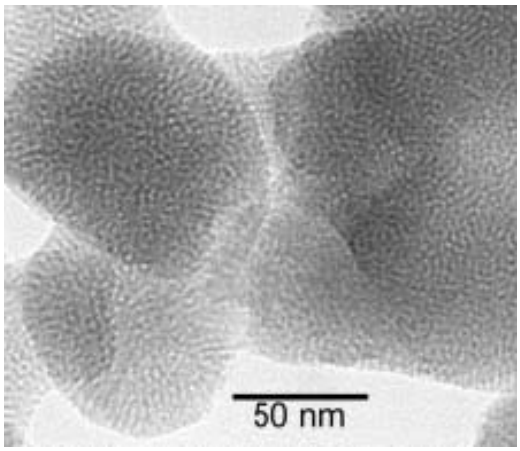

Figure 5-3. TEM micrograph of Al-MS.

N_2 Adsorption Analysis. The N_2 adsorption-desorption isotherm of Al-MS was of type IV, which is characteristic of mesoporous materials (Figure 5-4a). High surface area (1099 m^2/g) and large pore volume (1.17 cm^3 /g) were observed. The BJH pore size distribution was also presented in Figure 5-4b, which indicted the existence of uniform sized mesopores with an average pore diameter of 27.3 Å and a narrow distribution throughout the whole material. In addition, we analyzed the Al-MS material by using the empirical Harkins-Jura adsorption method. A median pore diameter of 23.9 Å was observed, which is only slightly different from the BJH value. The microporosity was not observed on the t-plot analysis of the adsorption data.

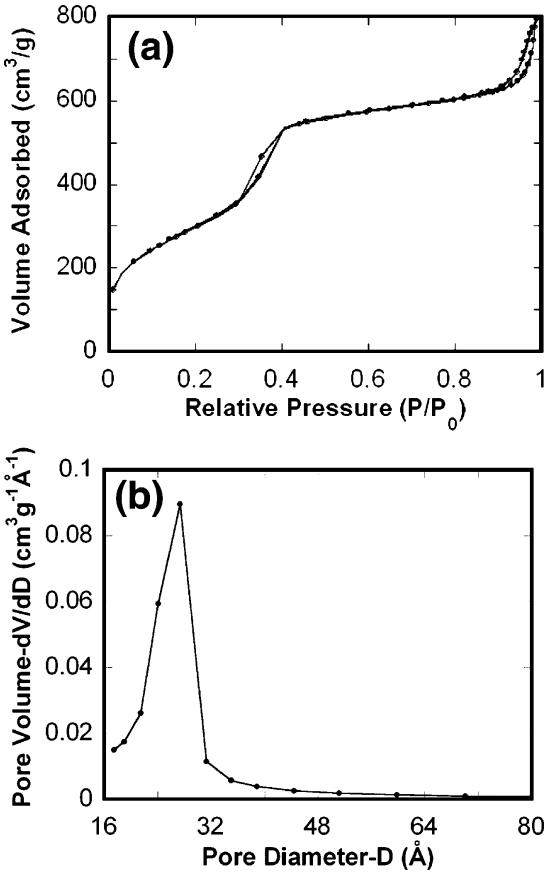

Figure 5-4. BET nitrogen adsorption/desorption isotherm (a) and BJH pore size distribution (b) of Al-MS.

Solid-State NMR Studies. ^{27}Al MAS spectrum of the hydrated Al-MS sample (Figure 5-5a) consists of a dominant resonance centered at around 54 ppm, which comprises 95% of overall intensity. The resonance at ~0 ppm (5%), representing the Al sites that became octahedrally coordinated due to the exposure of sample to water, vanished upon subsequent drying at 100 °C. The pentahedral Al sites, which typically resonate near 30 ppm,[43] were not detected. The corresponding MQMAS spectrum (Figure 5-5b) shows a similar line along the isotropic (vertical) axis centered at δ_{ISO} = 56 ppm. From the MQMAS spectrum, the second-order quadrupole parameter P_Q was estimated at 2.1 MHz. Note that $P_Q = C_Q\sqrt{1+\eta_Q^2/3}$ where C_Q is the quadrupole coupling constant and η_Q is the asymmetry

parameter of the electric field gradient tensor. The observed line shape parameters suggest that aluminum is present in the tetrahedral positions, most likely in the Al-MS framework. Although the isotropic projection of the MQMAS spectrum looks very similar to the MAS spectrum, the diagonally extended ridge that correlates the two dimensions is shaped by the distribution of isotropic chemical shifts.[44] The results of ^{27}Al spin counting, which was performed on the hydrated samples according to the procedure described in the experimental section, showed that the overall Si/Al ratio in the studied sample is 60 ± 5(~ 0.9 wt %). The dried samples typically yielded considerably lower ^{27}Al intensity than observed in hydrated materials. This is attributed to the increased quadrupolar broadening associated with the sites near the surface. It is well-known that the aluminum sites whose second-order broadening under MAS becomes comparable or greater than ν_R may become unobservable in the NMR spectrum.[29,45] In the hydrated sample, the water molecules were able to relax the lattice strain and reduce the resulting quadrupolar broadening.

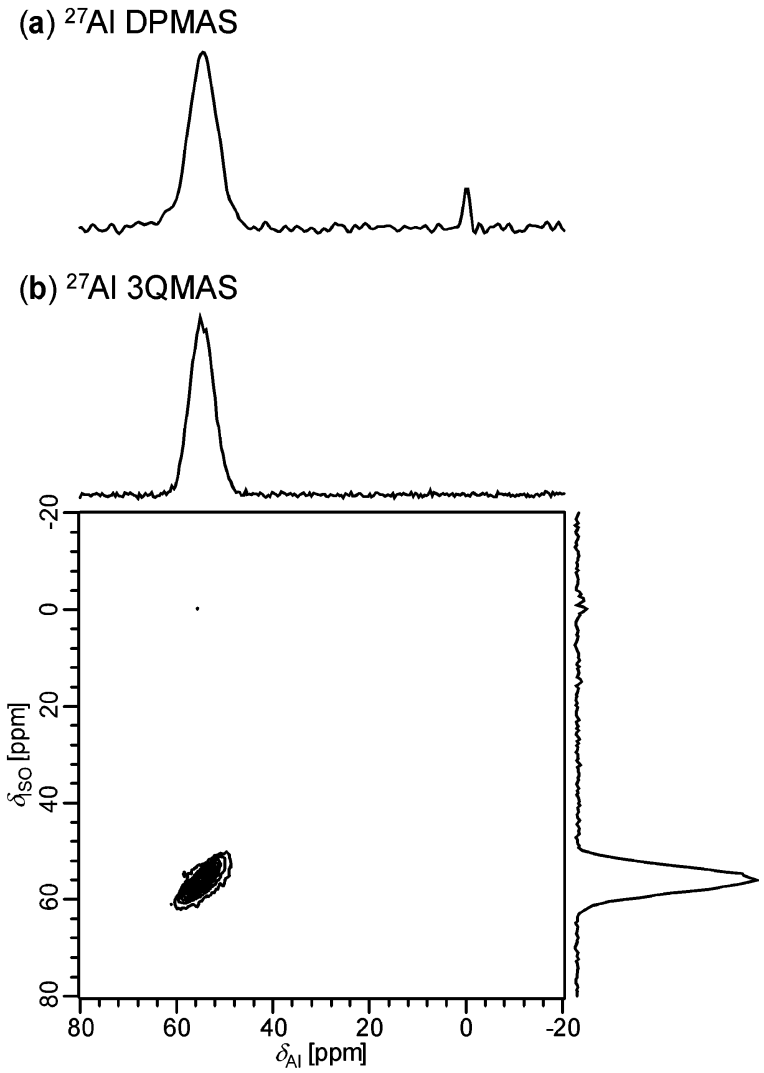

Figure 5-5. (a) ^{27}Al DPMAS and (b) ^{27}AlMQMAS spectra of hydrated Al-MS acquired with ν_R = 10 KHz. The MQMAS experiment was performed using ν_{RF}^{Al} = 8 kHz during the soft pulse, 48 t_1 increments of 40 μs, and 7200 scan per t_1 increment in the hypercomplex acquisition mode. The spectrum is displayed after shearing, using the isotropic scale δ_{ISO} in the MQ (vertical) dimension.[44]

In the discussion below, we will denote the silicon sites as $Q^n(m\text{Al})$, where n is the number of next nearest neighbor silicon and aluminum atoms, m of which are aluminum. ^{1}H-^{29}Si CPMAS and ^{29}Si DPMAS spectra (Figure 5-6a,b) consist of three partially overlapping resonances at around -92, -101, and -110 ppm, which can be readily assigned to the silicon sites Q^2(0Al) (geminal silanols (Si-O-)$_2$*Si*(OH)$_2$), Q^3(0Al) (single silanols, (Si-O-)$_3$*Si*OH),

and Q^4(0Al) (siloxanes).[43,46] The line width corresponding to each of these sites is in the order of 6-7 ppm, which causes partial overlap in the spectra. Since ^{1}H decoupling had no effect on the observed line width, the resolution in the ^{29}Si MAS spectra is governed by the distribution of chemical shifts resulting from the variation of Si-O-Si distances and bond angles.[47] Based on the deconvolution of the DPMAS spectrum, the relative intensities of Q^2(0Al), Q^3(0Al), and Q^4(0Al) sites were estimated at 4%, 39%, and 57%, respectively. The concentration of OH groups was determined to be 4 ± 0.5 per nm^2, which corresponds to ~7 mmol/g.

Because aluminum is responsible for Brønsted acidity in aluminum silicate catalysts, a detailed characterization of Al environment(s) in Al-MS, especially concerning the location of four-coordinate species, was of particular importance to this study. However, the choice of the best experimental strategy for such characterization by NMR was not obvious. The ^{29}Si resonances corresponding to the $Q^n(m\text{Al})$ sites involved in Si-O-Al bonds (i.e., with $m > 0$), cannot be discerned in the DPMAS and ^{1}H-^{29}Si CPMAS spectra because of the very low Al content and the overlap with the chemical shift ranges of Q^n(0Al) sites described above.[43] In an earlier study of aluminum silicate MCM-41 materials with high Si/Al ratio, it has been shown, based on the ^{1}H-^{27}Al HETCOR spectrum, that a significant fraction of the tetrahedrally coordinated aluminum resided near the head groups of the surfactant molecules inside the pores.[35] Given the low Al content and lack of surfactant molecules in our samples, the two-dimensional (2D) homo or heteronuclear correlation spectra involving ^{27}Al nuclei are beyond the current detection limit of solid-state NMR.

It has been also demonstrated that the use of 1D and 2D through space ^{27}Al-^{29}Si methods, such as CPMAS or transferred echo double resonance (TEDOR), is feasible in

zeolite networks.[48] Again, assuming the most favorable scenario of a homogeneous distribution of aluminum atoms within our mesoporous framework, less than 0.3% of silicon sites would be involved in ^{27}Al-O-^{29}Si connectivities under natural ^{29}Si abundance. We found this to be below the detection limit of a standard ^{27}Al-^{29}Si CPMAS NMR experiment. However, we were able to detect the ^{27}Al-^{29}Si cross polarization signal using the RAPT-CPMAS-CPMG scheme illustrated in Figure 5-1 and described in the experimental section. The resulting spectra, taken with hydrated and dried samples, are shown in Figure 5-6c,d. Because the CP process is sensitive to Al-Si distances not exceeding 0.4-0.5 nm, this experiment selectively brings to light ^{29}Si resonances attributable to $Q^n(m\text{Al})$ sites with $m > 0$ while suppressing those representing $Q^n(0\text{Al})$. Indeed, the spectrum in Figure 5-6c consists of two previously undetected peaks centered at -104 and -96 ppm. Because the signals corresponding to $Q^n(1\text{Al})$ sites are typically shifted downfield by approximately 5 ppm with respect to the corresponding $Q^n(0\text{Al})$ sites,[47,49,50] these two peaks can be assigned to $Q^4(1\text{Al})$ and $Q^3(1\text{Al})$ silicons, respectively. The fact that the ^{27}Al-^{29}Si RAPT-CPMAS-CPMG spectrum of the dried sample (Figure 5-6d) features only the peak centered at approximately -103 ppm is consistent with our assignment. The $Q^3(1\text{Al})$ sites, which are expected near the pore surface, are likely to become "invisible" in the dried sample, because the neighboring ^{27}Al nuclei are not polarizable under the conditions of our experiment. Note that sites with $m > 1$, expected between -85 and -95 ppm,[43] are not present in this sample in detectable concentration. If the aluminum atoms assumed positions within the Al-MS framework, the presence of both such sites would be expected.

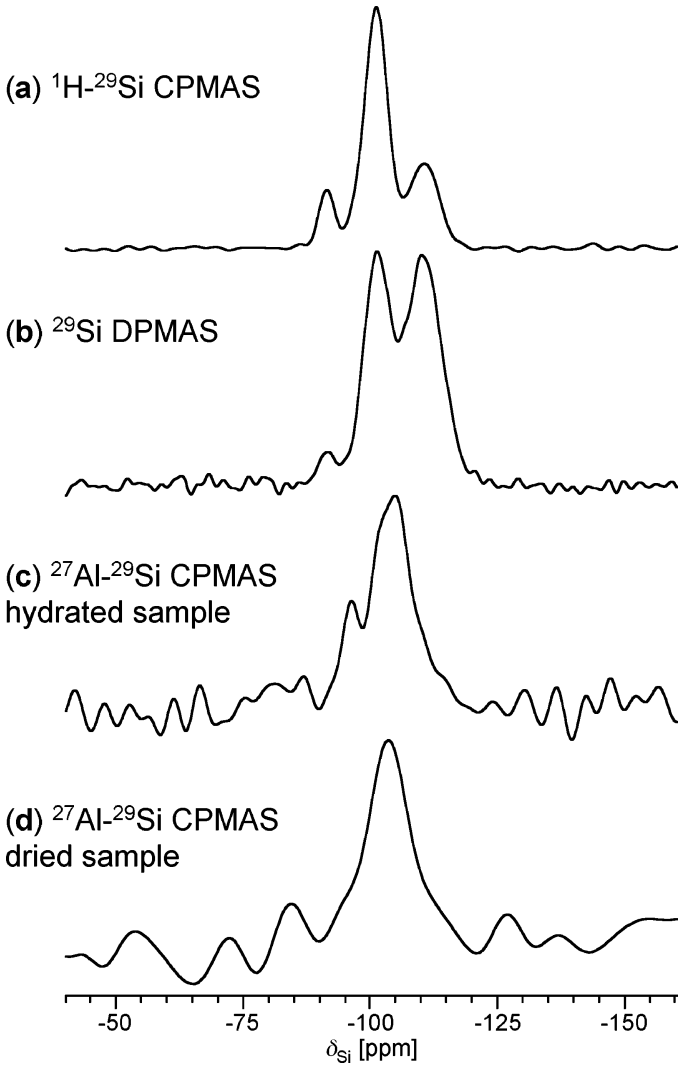

Figure 5-6. (a) ^{1}H-^{29}Si CPMAS, (b) 29Si DPMAS and (c,d) ^{27}Al-^{29}Si CPMAS spectra of Al-MS. The sample was studied in a hydrated state (a) – (c) and after drying at 100 °C ν_R = 10 kHz, ν_{RF}^{H}= 96 kHz during the initial excitation, ν_{RF}^{H} =34 – 40 kHz during the ramped CP, ν_{RF}^{Si} = 34 kHz during CP and CPMG, τ_{CP} = 8ms, τ_{CPMG}= 4 ms, n_{CPMG}= 6, recycle delay =1 s, and *NS* = 3000. To quantitatively measure the concentrations of silicon functionalities in the DPMAS experiment, spectrum (b), we used ν_R = 10 kHz, a recycle delay of 300 s, and *NS* = 300. Spectra (c,d) were obtained using the RAPT–CP–CPMG sequence shown in Figure 1, under the following experimental condition: ν_R= 10 kHz, ν_{RF}^{Al}= 6 kHz during RAPT, τ_{RAPT}= 1.2 ms, ν_{RF}^{Al}= 1.5 kHz during CP, ν_{RF}^{Si}= 7–8 kHz during ramped CP, τ_{CP} = 6 ms, ν_{RF}^{Si}= 26 kHz during CPMG, n_{CPMG} = 6, τ_{CPMG}= 4 ms, recycle delay = 10 ms (after the acquisition of the last echo), and NS = 6000000. Note that the actual delay between scans in (c) was $\tau_{RAPT}+\tau_{CP}$ $+6.5\,\tau_{CPMG}$+recycle delay ≈ 43 ms.

Finally, by comparing the intensity observed in zeolite 13X under the same conditions, we were able to assess that the spectrum in Figure 5-6c does indeed represent most of aluminum (90 ± 10%) in the Al-MS sample. This finding has important implications. First, it confirms that most, if not all, of the aluminum atoms assumed positions within the Al-MS framework. Accordingly, it rules out the existence of undesirable aluminum rich phases, which were earlier reported during the synthesis involving sodium aluminate.[51] Second, it implies that the spectrum in Figure 5-6c reasonably well represents the silicon functionalities that surround aluminum in Al-MS. Note that the intensity ratio between peaks representing Q^4(1Al) and Q^3(1Al) in this spectrum (estimated by deconvolution and integration to be approximately 3) is more than 2 times higher than the corresponding Q^4(0Al):Q^3(0Al) ratio in the ^{29}Si DPMAS spectrum of the same sample (which is slightly below 1.5). Thus, the fraction of aluminum sites that reside on the surface is estimated at around 25% instead of 40%, which further implies that the silicon to the (Si/Al)s ratio is equal to (40/25) × 60 ≈ 100. This is a rough approximation due to possible inaccuracies of the spectral intensities and the fact that we have neglected the small concentration (4%) of Q^2(0Al) sites. Notwithstanding these factors, we have demonstrated, for the first time, an inhomogeneous distribution of aluminum sites between the surface and bulk matrix of mesoporous aluminum silicates prepared by direct synthesis (co-condensation). Because only the surface Al sites are chemically accessible, we will use the adjusted $(Si/Al)_s$ value of 100 rather than the bulk composition of 60 in the evaluation of the catalytic activity of our Al-MS material

The stability of Al-MS was studied by comparing the ^{27}Al MAS spectra of sample after heating at 100, 300, and 400 °C for 3 h under a pressure of 10^{-5} Torr. The spectra,

shown in Figure 5-7, are similar to those of as-synthesized material in terms of line shape and intensity. Again, upon the subsequent rehydration the intensity was almost doubled and a small contribution from octahedrally coordinated Al appeared at around 0 ppm. A gradual broadening of the resonance at 54 ppm was observed with increasing temperature, up to 50% in the sample heated to 400 °C, due to dehydroxylation of the pore surface.

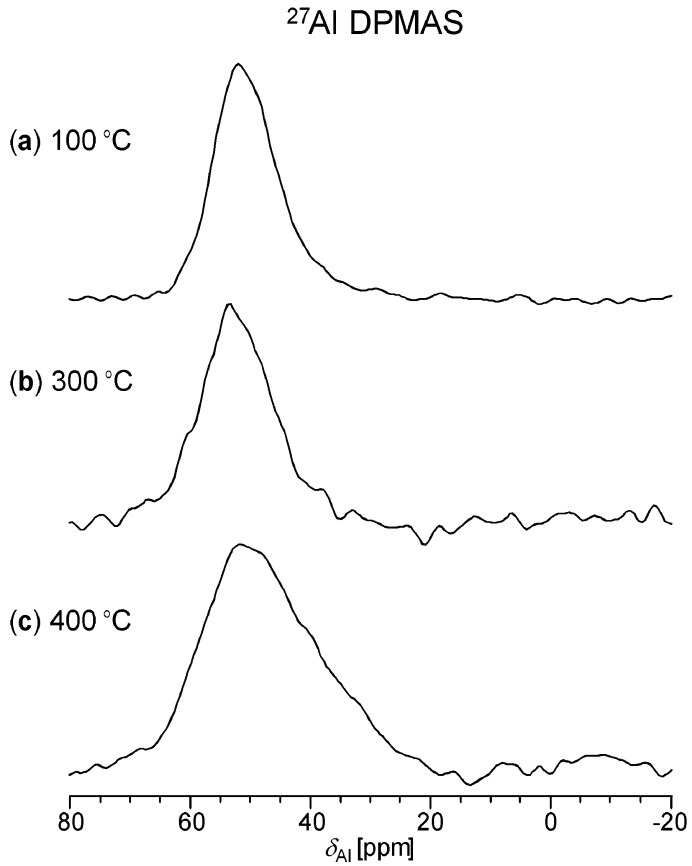

Figure 5-7. (a) – (c) ^{27}Al DPMAS spectra of Al-MS sample calcined at 100, 300, and 400 °C.

Catalytic Activity. Claisen rearrangement reaction of allyl phenyl ether (**A**) to *o*-allylphenol (**I**) and 2,3-dihydro-2-methylbenzofuran (**P**) was used to evaluate the catalytic performance of our Al-MS material. The reaction scheme is shown in Figure 5-8, where k_1 and k_2 are rate constants for the first and second steps, respectively. The **A** first undergoes

intramolecular rearrangement to produce **I**, then further cyclizes to form **P** product. As reported previously, purely siliceous (Al-free) MCM-41 did not exhibit any catalytic activity for Claisen rearrangement reaction,[52] which is an acid-catalyzed reaction at high temperature (>200 °C). Upon mixing 0.73 M of allyl phenyl ether with 0.1 g of Al-MS in 9 mL refluxing toluene, we found that the reaction yield reached 98% in about 7 h as monitored by GC. A kinetic plot of the percentage of each species against reaction time is shown in Figure 5-9. Because this reaction consists of two first-order consecutive steps in which **I** first builds up and then falls, the rate constants k_1 and k_2 could be determined by using the following equations:

$$\frac{A}{A_0} = \exp(-k_1 t)$$

$$\frac{I}{A_0} = \frac{k_1}{k_2 - k_1}[\exp(-k_1 t) - \exp(-k_2 t)]$$

$$\frac{P}{A_0} = 1 - \frac{1}{k_2 - k_1}\{[k_2 \exp(-k_1 t)] - [k_1 \exp(-k_2 t)]\}$$

The kinetic data and the reaction conversion are given in Table 5-1. For our Al-MS material, the reaction conversion reaches 98% at the end of 7 h and the average value of k_1 and k_2 is 10.6×10^{-3} min^{-1} and 12.9×10^{-3} min^{-1}, respectively. Thus, it was confirmed that our material is a very active catalyst for Claisen rearrangement reaction. As described previously, the solid-state NMR results indicated that the tetrahedrally coordinated, strong Brønsted acidic Al sites were observed throughout the Al-MS material. However, only the surface Al sites could be accessed by the reaction substrates. Therefore, the observed catalytic reactivity of our Al-MS should be attributed to the surface Al sites with an estimated Si/Al ratio of 100 according to the NMR analysis. This Si/Al ratio is significantly

lower than those (typically between 4 and 40) of other literature reported mesoporous aluminum silicate materials prepared by other synthesis methods.[23-25,30,34] Our results suggest that the distribution of the acidic Al sites could be better controlled by adjusting the co-condensation reaction condition, such as the pH value and the amount of Al introduced to the co-condensation reaction. We envision that this method would lead to higher catalytic reactivity of the mesoporous mixed oxide materials.

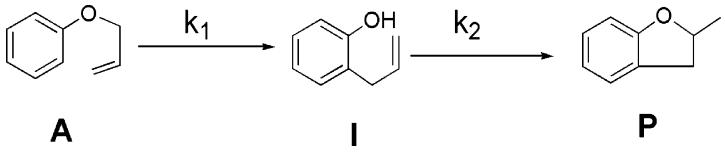

Figure 5-8. Reaction scheme of Claisen rearrangment of allyl phenyl ether: allyl phenyl ether (**A**); *o*-allylphenol (**I**), and 2,3-dihydro-2-methylbenzofuran (**P**).

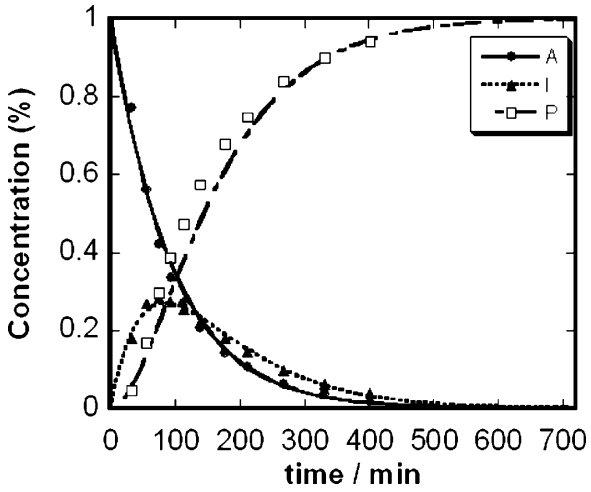

Figure 5-9. A typical kinetic trace of allyl phenyl ether rearrangment reaction. Condition: 0.73 M allyl phenyl ether and 0.1 g Al-MS in toluene at 110 °C.

Table 5-1: Reactivity of Al-MS for Claisen rearrangement reaction of allyl phenyl ether

sample	conversion	k_1 (min^{-1})	k_2 (min^{-1})
Al-MS (Si/Al = 60) ((Si/Al)s = 100)	98% (7 h)	10.6×10^{-3}	12.9×10^{-3}
Al-MS (Si/Al = 20)[a]	87% (12 h)	2.7×10^{-3} [a]	3.0×10^{-3} [a]

[a]. From ref 52. Condition: reaction temperature, 120 °C; reaction time, 12 h in tetracholoroethylene.

Conclusion

In summary, we have demonstrated that a mesoporous aluminum silicate material with single-type Al sites has been successfully synthesized via a base-catalyzed co-condensation reaction. Solid-state NMR studies showed that the aluminum atoms are tetrahedrally coordinated in environments that appear to be stable up to at least 400 °C. By directly detecting the Al-Si connectivities, we have provided the first direct characterization of these environments. First, we ruled out the existence of undesirable aluminum rich phases. Second, the distribution of aluminum sites was found to be inhomogeneous with the occupancy of the Al sites enclosed in the bulk silica matrix being higher than those on the surface. Consequently, in the evaluation of the catalytic activity of our Al-MS material used the adjusted $(Si/Al)_s$ value of 100 rather than the bulk composition of 60. Reactivity study of the mesoporous aluminosilicate shows a good catalytic reactivity for the Claisen rearrangement of allyl phenyl ether, despite the low surface concentration of Al.

Acknowledgment

The support for this research work at Ames Laboratory through the U.S. DOE, office of Basic Energy Sciences, through the Catalysis Science Grant No. AL-03-380011 and under Contract W-7405-Eng-82 is gratefully acknowledged.

References:

(1) Beck, J. S.; Vartuli, J. C.; Roth, W. J.; Leonowicz, M. E.; Kresge, C. T.; Schmitt, K. D.; Chu, C. T. W.; Olson, D. H.; Sheppard, E. W.; et al. A New Family of Mesoporous Molecular Sieves Prepared with Liquid Crystal Templates. *J. Am. Chem. Soc.* **1992**, *114* (27), 10834-43.

(2) Kresge, C. T.; Leonowicz, M. E.; Roth, W. J.; Vartuli, J. C.; Beck, J. S. Ordered mesoporous molecular sieves synthesized by a liquid-crystal template mechanism. *Nature* **1992**, *359* (6397), 710-12.

(3) Corma, A. From Microporous to Mesoporous Molecular Sieve Materials and Their Use in Catalysis. *Chem. Re*V. **1997**, *97* (6), 23732419.

(4) Zhao, X. S.; Lu, G. Q.; Millar, G. J. Advances in Mesoporous Molecular Sieve MCM-41. *Ind. Eng. Chem. Res.* **1996**, *35* (7), 2075-2090.

(5) Corma, A.; Grande, M. S.; Gonzalez-Alfaro, V.; Orchilles, A. V. Cracking activity and hydrothermal stability of MCM-41 and its comparison with amorphous silica-alumina and a USY zeolite. *J. Catal.* **1996**, *159* (2), 375-382.

(6) Luan, Z.; Cheng, C.-F.; Zhou, W.; Klinowski, J. Mesopore Molecular Sieve MCM-41 Containing Framework Aluminum. *J. Phys. Chem.* **1995**, *99* (3), 1018-24.

(7) Luan, Z.; Cheng, C.-F.; He, H.; Klinowski, J. Thermal Stability of Structural Aluminum in the Mesoporous Molecular Sieve MCM-41. *J. Phys. Chem.* **1995**, *99* (26), 10590-3.

(8) Corma, A.; Fornes, V.; Navarro, M. T.; Perez-Pariente, J. Acidity and stability of MCM-41 crystalline aluminosilicates. *J. Catal.* **1994**, *148* (2), 569-74.

(9) Schmidt, R.; Akporiaye, D.; Stocker, M.; Ellestad, O. H. Synthesis of a mesoporous MCM-41 material with high levels of tetrahedral aluminum. *J Chem. Soc., Chem. Commun.* **1994**, (12), 1493-4.

(10) Ryoo, R.; Ko, C. H.; Howe, R. F. Imaging the Distribution of Framework Aluminum in Mesoporous Molecular Sieve MCM-41. *Chem. Mater.* **1997**, *9* (7), 1607-1613.

(11) Yonemitsu, M.; Tanaka, Y.; Iwamoto, M. Metal Ion-Planted MCM-41. 1. Planting of Manganese(II) Ion into MCM-41 by a Newly Developed Template-Ion Exchange Method. *Chem. Mater.* **1997**, *9* (12), 2679-2681.

(12) Zhao, D.; Goldfarb, D. Synthesis of mesoporous manganosilicates: Mn-MCM-41, Mn-MCM-48 and Mn-MCM-L. *J. Chem. Soc., Chem. Commun.* **1995**, (8), 875-6.

(13) Cheng, C.-F.; He, H.; Zhou, W.; Klinowski, J.; Goncalves, J. A. S.; Gladden, L. F. Synthesis and Characterization of the Gallosilicate Mesoporous Molecular Sieve MCM-41. *J. Phys. Chem.* **1996**, *100* (1), 390-6.

(14) Sayari, A.; Danumah, C.; Moudrakovski, I. L. Boron-Modified MCM-41 Mesoporous Molecular Sieves. *Chem. Mater.* **1995**, *7* (5), 813-15.

(15) Liu, S.; Heyong, H.; Luan, Z.; Klinowski, J. Solid-state NMR studies of the borosilicate mesoporous molecular sieve MCM-41. *J. Chem. Soc., Faraday Trans.* **1996**, *92* (11), 2011-2015.

(16) Niessen, T. E. W.; Niederer, J. P. M.; Gjervan, T.; Holderich, W. F. Synthesis and characterization of titanium-containing MCM-41 using (NH4)3[Ti(O2)F5] as the titanium source. *Microporous Mesoporous Mater.* **1998**, *21* (1-3), 67-74.

(17) Corma, A.; Navarro, M. T.; Perez Pariente, J. Synthesis of an ultralarge pore titanium silicate isomorphous to MCM-41 and its application as a catalyst for selective oxidation of hydrocarbons. *J. Chem. Soc., Chem. Commun.* **1994**, (2), 147-8.

(18) Luan, Z.; Xu, J.; He, H.; Klinowski, J.; Kevan, L. Synthesis and Spectroscopic Characterization of Vanadosilicate Mesoporous MCM-41 Molecular Sieves. *J. Phys. Chem.* **1996**, *100* (50), 19595-19602.

(19) Park, D. H.; Cheng, C.-F.; He, H.; Klinowski, J. Synthesis and characterization of vanadosilicate mesoporous molecular sieves MCM-41. *J. Mater. Chem.* **1997**, *7* (1), 159-162.

(20) Reddy, K. M.; Moudrakovski, I.; Sayari, A. Synthesis of mesoporous vanadium silicate molecular sieves. *J. Chem. Soc., Chem. Commun.* **1994**, (9), 1059-60.

(21) Mokaya, R., Ultrastable mesoporous aluminosilicates by grafting routes. *Angew. Chem., Int. Ed.* **1999**, *38* (19), 2930-2934.

(22) Ryoo, R.; Kim, M. J.; Kim, J. M.; Jun, S. Generalized route to the preparation of mesoporous metallosilicates via post-synthetic metal implantation. *Chem. Commun.* **1997**, (22), 2225-2226.

(23) Mokaya, R., Post-synthesis grafting of Al onto MCM-41. *Chem. Commun.* **1997**, (22), 2185-2186.

(24) Hamdan, H.; Endud, S.; He, H.; Nazlan, M.; Muhid, M.; Klinowski, J. Alumination of the purely siliceous mesoporous molecular sieve MCM41 and its hydrothermal conversion into zeolite Na-A. *J. Chem. Soc., Faraday Trans.* **1996**, *92* (12), 2311-2315.

(25) Mokaya, R.; Jones, W. Efficient post-synthesis alumination of MCM-41 using aluminum chlorohydrate containing Al polycations. *J. Mater. Chem.* **1999**, *9* (2), 555-561.

(26) Chen, L. Y.; Ping, Z.; Chuah, G. K.; Jaenicke, S.; Simon, G., A comparison of post-synthesis alumination and sol-gel synthesis of MCM41 with high framework aluminum content. *Microporous Mesoporous Mater.* **1999**, *27* (2-3), 231-242.

(27) Zanjanchi, M. A.; Asgari, S. Incorporation of aluminum into the framework of mesoporous MCM-41: the contribution of diffuse reflectance spectroscopy. *Solid State Ionics* **2004**, *171* (3-4), 277-282.

(28) Yu, J.; Shi, J.-L.; Wang, L.-Z.; Ruan, M.-L.; Yan, D.-S. Room temperature synthesis of mesoporous aluminosilicate materials. *Ceram. Int.* **2000**, *26* (4), 359-362.

(29) Jun, S.; Ryoo, R. Aluminum Impregnation into Mesoporous Silica Molecular Sieves for Catalytic Application to Friedel-Crafts Alkylation. *J. Catal.* **2000**, *195* (2), 237-243.

(30) Oumi, Y.; Takagi, H.; Sumiya, S.; Mizuno, R.; Uozumi, T.; Sano, T. Novel post-synthesis alumination method for MCM-41 using trimethylaluminum. *Microporous Mesoporous Mater.* **2001**, *44-45*, 267-274.

(31) Mokaya, R.; Jones, W.; Luan, Z.; Alba, M. D.; Klinowski, J. Acidity and catalytic activity of the mesoporous aluminosilicate molecular sieve MCM-41. *Catal. Lett.* **1996**, *37* (1,2), 113-20.

(32) Luan, Z.; He, H.; Zhou, W.; Cheng, C.-F.; Klinowski, J. Effect of structural aluminum on the mesoporous structure of MCM-41. *J. Chem. Soc., Faraday Trans.* **1995**, *91* (17), 2955-9.

(33) Liu, Y.; Zhang, W.; Pinnavaia, T. J. Steam-stable MSU-S aluminosilicate mesostructures assembled from zeolite ZSM-5 and zeolite beta seeds. *Angew. Chem., Int. Ed*. **2001**, *40* (7), 1255-1258.

34) Ghanbari-Siahkali, A.; Philippou, A.; Garforth, A.; Cundy, C. S.; Anderson, M. W.; Dwyer, J. A comparison of direct synthesis and vapor phase alumination of MCM-41. *J. Mater. Chem.* **2001**, *11* (2), 569-577.

(35) Janicke, M. T.; Landry, C. C.; Christiansen, S. C.; Birtalan, S.; Stucky, G. D.; Chmelka, B. F. Low Silica MCM-41 Composites and Mesoporous Solids. *Chem. Mater.* **1999**, *11* (5), 1342-1351.

(36) Yao, Z.; Kwak, H. T.; Sakellariou, D.; Emsley, L.; Grandinetti, P. J. Sensitivity enhancement of the central transition NMR signal of quadrupolar nuclei under magic-angle spinning. *Chem. Phys. Letters* **2000**, *327* (1,2), 85-90.

(37) Freude, D.; Haase, J. *NMR Basic Principles and Progress*. Springer-Verlag: Berlin, 1993; Vol. 29, p 1.

(38) Meiboom, S.; Gill, D. Modified spin-echo method for measuring nuclear relaxation times. *Re*V. *Sci. Instrum.* **1958**, *29*, 688-91.

(39) Garroway, A. N. Homogeneous and inhomogeneous nuclear spin echoes in organic solids: adamantane. *J. Magn. Reson.* **1977**, *28* (3), 365-71.

(40) Trebosc, J.; Wiench, J. W.; Huh, S.; Lin, V. S. Y.; Pruski, M. Studies of Organically Functionalized Mesoporous Silicas Using Heteronuclear Solid-State Correlation NMR Spectroscopy under Fast Magic Angle Spinning. *J. Am. Chem. Soc.* **2005**, *127* (20), 7587-7593.

(41) Vega, A. J. CP/MAS of quadrupolar S = 3/2 nuclei. *Solid State Nucl. Magn. Reson.* **1992**, *1* (1), 17-32.

(42) Amoureux, J. P.; Pruski, M. Theoretical and experimental assessment of single-and multiple-quantum cross-polarization in solid state NMR. *Mol. Phys.* **2002**, *100* (10), 1595-1613.

(43) Engelhardt, G.; Michel, D. *High-Resolution Solid-State NMR of Silicates and Zeolites*; Wiley: New York, 1989.

(44) Amoureux, J. P.; Pruski, M. *Encyclopedia NMR*, 1st ed.; John Wiley & Sons: Chichester, England 2002; Vol. 9, p 226-251.

(45) Man, P. P.; Klinowski, J.; Trokiner, A.; Zanni, H.; Papon, P. Selective and nonselective NMR excitation of quadrupolar nuclei in the solid state. *Chem. Phys. Letters* **1988**, *151* (1-2), 143-50.

(46) Maciel, G. E. *Encylopedia of Nuclear Magnetic Resonance*; John Wiley & Sons Ltd: Chichester, England, 1996; Vol. 7, p 4370-4386.

(47) Ramdas, S.; Klinowski, J. A simple correlation between isotropic silicon-29 NMR chemical shifts and T-O-T angles in zeolite frameworks. *Nature (London)* **1984**, *308* (5959), 521-3.

(48) Fyfe, C. A.; Wong-Moon, K. C.; Huang, Y.; Grondey, H.; Mueller, K. T. Dipolar-Based 27Al -> 29Si Solid-State NMR Connectivity Experiments in Zeolite Molecular Sieve Frameworks. *J. Phys. Chem.* **1995**, *99* (21), 8707-16.

(49) Hong, S. B.; Han, D.-Y.; Han, O. H.; Nam, I.-S. Solid-state NMR evidence for the presence of two crystallographically distinct tetrahedral sites in zeolite merlinoite. *Chem. Commun.* **2000**, (18), 1719-1720.

(50) Jacobsen, H. S.; Norby, P.; Bildsoe, H.; Jakobsen, H. J. A 1:1 correlation between aluminum-27 and silicon-29 chemical shifts and correlations with lattice structures for some aluminosilicate sodalites. *Zeolites* **1989**, *9* (6), 491-5.

(51) Kloetstra, K. R.; Zandbergen, H. W.; van Bekkum, H. MCM-41 type materials with low Si/Al ratios. *Catal. Lett.* **1995**, *33* (1,2), 157-63.

(52) Mathew, N. T.; Khaire, S.; Mayadevi, S.; Jha, R.; Sivasanker, S. Rearrangement of allyl phenyl ether over Al-MCM-41. *J. Catal.* **2005**, *229* (1), 105-113.